A Multidisciplinary Approach to Neuropathic Pain: Assessing Tactile Sensation and Neuroma Pain Factors

Dissertation for the award of the degree

"Doctor of Philosophy"

of the Georg-August-Universität Göttingen

within the Molecular Medicine doctoral program of Göttingen Graduate School for Neurosciences, Biophysics, and Molecular Biosciences (GGNB) and Georg-August University School of Science (GAUSS)

submitted by

Luis Ángel Pardo Sánchez

from Oviedo (Spain)

Göttingen, 2023

THESIS COMMITTEE

Prof. Dr. Arndt F. Schilling

(Dept. of Trauma Surgery, Orthopaedics and Plastic Surgery, UMG)

Prof. Dr. Christine Stadelmann-Nessler

(Dept. of Neuropathology, UMG)

Prof. Dr. Frauke Alves

(Translational Molecular Imaging Group, MPI for Multidisciplinary Sciences)

MEMBERS OF THE EXAMINATION BOARD

Reviewer: **Prof. Dr. Arndt F. Schilling**

(Dept. of Trauma Surgery, Orthopaedics and Plastic Surgery, UMG)

Second Reviewer: **Prof. Dr. Christine Stadelmann-Nessler**

(Dept. of Neuropathology, UMG)

Further members of the Examination Board:

Prof. Dr. Frauke Alves

(Translational Molecular Imaging Group, MPI for Multidisciplinary Sciences)

Prof. Dr. Andrea Antal

(Non-Invasive Brain Stimulation Laboratory, Dept. of Neurology, UMG)

Prof. Dr. Ralf Dressel

(Institute for Cellular and Molecular Immunology, UMG)

Prof. Dr. Michael Sereda

(Translational Neurogenetics, MPI for Multidisciplinary Sciences)

Date of the oral examination: 26.06.2023

ACKNOWLEDGMENTS

I would like to express my deepest gratitude to everyone who contributed to the successful completion of this thesis. My journey began alongside the COVID-19 pandemic and with much uncertainty in the world. However, it ended up being an incredible one, and I could not have reached this point without the support, guidance, and encouragement of a lot of remarkable people.

First and foremost, I am immensely thankful and wish to recognize my doctoral advisor, or "Doktorvater" in German, Prof. Dr. Arndt F. Schilling, not only for his unwavering support in matters related to my research but also in broader aspects of life. I have previously expressed my admiration for his exceptional mentorship and guidance, as he has been a remarkable guide and a source of inspiration, consistently going above and beyond to help me grow, both as a researcher and a person. As I look forward to the next chapter of my professional journey, I sincerely hope that we can continue to work together toward making the world a better place.

I would also like to express my profound gratitude to my supervisor, Dr. Jennifer Ernst, for believing in me from the very beginning and fully involving me in all projects. We often argued based on our ideas but eventually discovered that these were compatible and complementary. I hope that after this phase of life, I can continue to rely on her deep understanding of medicine and scientific approach to questioning and striving for improvement.

Furthermore, I would like to thank Prof. Dr. Christine Stadelmann-Nessler, and Prof. Dr. Frauke Alves, members of my advisory committee. Their invaluable insights, critical feedback, and continuous encouragement have been instrumental in shaping my research and keeping me focused throughout this process. I am truly grateful for their commitment and dedication to my academic growth.

I would like to thank the examination board members, Prof. Dr. Andrea Antal, Prof. Dr. Ralf Dressel, and Prof. Dr. Michael Sereda, for taking the time to participate in my defense.

I am truly grateful and would like to acknowledge Dr. Marko Markovic and Dr. Carolina Thomas. Their expertise, patience, and mentorship have always helped me to find the right way and keep going. The constant availability and valuable feedback were important building blocks on this journey.

Additionally, I would like to acknowledge my colleagues and friends from the Department of Trauma Surgery, Orthopaedics, and Plastic Surgery, the Department of Neuropathology, and

the Translational Molecular Imaging Group. Particularly Dr. Jonas Franz, for initial input and help handling (very) large images, Paula Mahn, for her help with the scanner, Katja Schulz, for the always prompt and excellent staining of the samples, even when there was a lot to do everywhere, and Dr. Fernanda Ramos, for providing new viewpoints on the peripheral nerve analysis, which I hope to proceed together further.

I would like to specially mention Miguel A. Bravo, for helping whenever necessary, in and outside the lab, and becoming a best friend, and Carmen Modrok for the valuable chats and company in the lab during the difficult times of home-officing.

Lastly, I am forever indebted to my family, especially my parents, Araceli Sánchez and Luis A. Pardo, for their encouragement and belief in me, and Verónica Herrero, for her unwavering love and infinite patience. Their support has been my source of strength and motivation throughout this journey, and I dedicate this thesis to them.

ABSTRACT

Neuropathic pain is a complex and often debilitating condition. Distally from the injury site, missing input contributes to deafferentation pain, while proximally, neuroma formation leads to peripheral and central sensitization, increasing pain sensation and lowering pain thresholds. Tactile feedback has been shown to potentially alleviate deafferentation pain by substituting missing afference and restoring sensorimotor incongruence.

This thesis establishes a baseline on the perception of mechanical vibration in the healthy arms of ten able-bodied participants. It investigates the effects of sensory loss after peripheral nerve injury (PNI) distal to the injury site when feedback is applied proximal to the injury site in five transradial amputees and, in six subjects with brachial plexus injury when applied distal to the lesion site. It then performs a comparative analysis of various aspects of neuromas forming proximal to the injury site. Here, several inflammation-related and morphological aspects are considered comparing patients with and without neuroma, and patients with and without neuroma pain.

Psychometric evaluation tasks were performed to quantify sensation threshold, just noticeable difference, Weber fraction, and perception of dynamically changing vibrotactile stimuli. Additionally, a combination of machine learning and computer vision was used to investigate several aspects of neuromas.

Results demonstrated that the sensation capacity on the arm does not differ from the one on a healthy arm proximally from the site of injury, which facilitates the design and accommodation of vibrotactile feedback interfaces. In contrast, if applied distally, the more distal it is applied the sensation capacity drastically decreases.

Moreover, inflammation-related cells were not more abundant in the neuroma group, however, patients suffering from pain had a significantly lower amount of organized (healthy) nervous tissue, suggesting the amount of organized tissue to counteract neuroma-evoked pain.

The findings presented here contribute to a deeper understanding of neuropathic pain, giving insight into how the lost connection between the receptors and the brain affects sensation proximal- and distally from the injury and, additionally, which further factors decide if a neuroma –if formed– is painful or not, aiding in the development of therapeutic approaches and strategies for its prevention.

ACRONYMS AND ABBREVIATIONS

Acronym/ abbreviation	Definition
AB	Able-bodied participant
BPI	Participant with a brachial plexus injury
CNS	Central nervous system
CX	Cervical X
Dors	Dorsal
LA	Lower arm
LX	Lumbar X
NDI	Number of distinct intervals
PLP	Phantom limb pain
PNI	Peripheral nerve injury
PNS	Peripheral nervous system
RF	Random forest
RLP	Residual limb pain
SH	Shoulder/ neck
ST	Sensation threshold
TMR	Targeted Muscle Reinnervation
TR	Participant with a transradial amputation
TX	Thoracic X
UA	Upper arm
Vent	Ventral
WF	Weber fraction

TABLE OF CONTENTS

1 INTRODUCTION

Neuropathic pain is a complex and multifaceted phenomenon resulting from damage or dysfunction within the nervous system, significantly impacting the quality of life for affected persons. The primary objective of this doctoral thesis is to shed light on the underlying mechanisms of several aspects of neuropathic pain. However, to fully understand the intricacies of neuropathic pain and the implications of the disrupted sensorimotor loop, a comprehensive introduction to the nervous system, its structure, function, and response to injury and pain is essential. This foundation will provide the necessary context for appreciating the challenges and opportunities in developing effective treatment strategies for neuropathic pain and restoring the proper functioning of the sensorimotor system.

1.1 THE PERIPHERAL NERVOUS SYSTEM

1.1.1 Anatomy of the nervous system

The nervous system, composed of the central nervous system (CNS) and the peripheral nervous system (PNS), serves as the body's sophisticated communication network, responsible for coordinating and regulating all physiological and behavioral responses of the organism [1]. It integrates sensory information, processes cognitive functions, and controls the motor output, ultimately allowing organisms to interact with their environment and forming the basis for the complexity and adaptability of living beings [1].

The CNS consists of the brain and spinal cord, functioning as the primary integrative center for processing and transmitting information throughout the body, using billions of neurons and glial cells to perform a vast array of cognitive, motor, and sensory functions [2]. While neurons, the fundamental cellular units of the nervous system, are organized into complex circuits that facilitate information processing, glial cells support neuronal function and maintain homeostasis [3]. The interconnectivity of these cells is supported by a complex network of synapses, which enables rapid and precise communication between neurons [4]. Neurotransmitters enable information transfer and modulate neuronal activity, ultimately influencing behavior and cognition [2] and adding further complexity to the CNS.

The PNS comprises cranial and spinal nerves, which serve as a functional interface between the rest of the body and the CNS. The cranial nerves are twelve paired nerves that send sensory information between the neck, head, torso, and brain and carry motor commands to control the

musculature of the neck and head. The sensory part is the one that transfers the information from the receptors to the spinal cord. In contrast, the motor part carries the impulses from the spinal cord to the corresponding effectors. Each spinal or rachidial nerve joins the spinal cord at two different points: the posterior and anterior roots, which fuse to form the spinal nerve. Since the posterior root contains sensory fibers and the anterior root contains motor fibers, the result is a mixed nerve [5].

Nerves group together to form plexuses that play essential roles in controlling various motor and sensory functions. The cervical plexus (C1-C4) mainly manages the functions of the head, neck, and trunk. The brachial plexus, located at the base of the neck and axillary fossa, is responsible for the innervation of the thoracic limb through connections between cervical nerves (C5, C6, C7, C8, and T1) and some contributions from C4 and T2. The lumbar plexus consists of connections between the anterior branches of spinal nerves (L1 to L4). Lastly, the sacral plexus, including the lumbosacral trunk and the anterior branches of the first three sacral nerves, provides innervation for the gluteal region, lower limb, and pelvis (from L4 to S4). [5]

Every nerve is formed by grouping several hundred or thousands of axons that join to form spatially arranged motor or sensory bundles called fascicles. [6, 7]. Each axon is surrounded by a thin connective tissue layer called the endoneurium, and each fascicle is covered by the perineurium. The nerve formed by the union of several fascicles is covered by the epineurium, surrounded by the mesoneurium, which contains the nerve's blood supply (Figure 1) [6, 7].

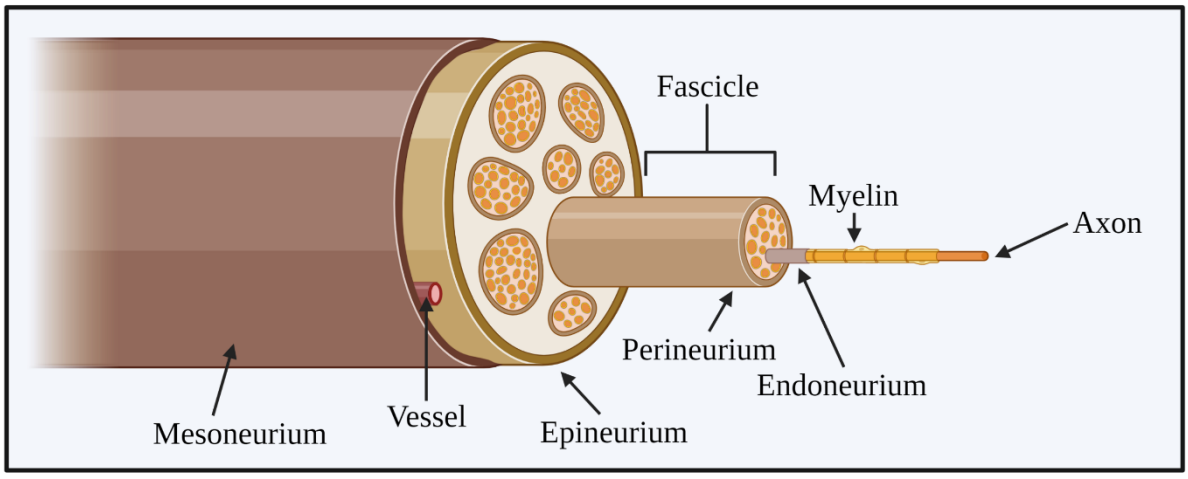

Figure 1 – Peripheral nerve. Schematic representation of the hierarchical structure within a peripheral nerve, illustrating key components such as the epineurium, perineurium, endoneurium, myelin sheath, and axon. These layers collectively provide mechanical protection, electrical insulation, and nutrient support to ensure the efficient transmission of nerve signals.

Nerves can be classified based on their physical characteristics and their conducting properties. It was long believed that differences in axon thickness, ranging from 0.1 to 20 µm, would impact the speed at which action potentials could travel along the axon, referred to as conduction velocity. This hypothesis was confirmed in 1927 by Erlanger and Gasser [8], who identified several types of nerve fibers and established a classification system based on the relationship between axon diameter and nerve conduction velocity. Their classification system divided the fibers into three groups: A, B, and C, and included both sensory fibers (afferents) and motor fibers (efferents) [8]. Group A fibers are the largest diameter nerve fibers (2-20 µm). These are further subdivided based on their conduction velocity and function into alpha (Aα – 60-120 $\frac{m}{s}$), beta (Aβ – 30-75 $\frac{m}{s}$), gamma (Aγ – 20-40 $\frac{m}{s}$), and delta (Aδ – 10-30 $\frac{m}{s}$) fibers. B fibers (3-20 $\frac{m}{s}$) are smaller in diameter (1-3 µm) and primarily involved in the autonomous nervous system. C fibers (0.5-2 $\frac{m}{s}$) are the smallest diameter nerve fibers (0.5-1.5 µm) and unmyelinated, in contrast to A and B fibers [9, 10].

1.1.2 The sensorimotor system

The sensorimotor system is a network that involves sensory organs, specific regions of the nervous system, and the body's motor control mechanisms, forming a loop of information between the CNS and PNS [2].

Efferent fibers transport information from the CNS mainly to the muscles and glands [6, 11] using two major tracts: the corticospinal [12] and the corticobulbar tract [13]. While the corticobulbar tract transmits motor commands from the cortex to the brainstem to control the muscles of the face, head, and neck, the corticospinal tract transmits motor commands from the cortex to the spinal cord. It originates in the primary motor cortex and descends through the internal capsule, a narrow pathway between the basal ganglia and the thalamus. It then passes through the brainstem and descends along the length of the spinal cord, forming synapses to lower motor neurons in the ventral horn [12, 13].

In contrast, afferent fibers transport information from the periphery to the brain [6, 11]. The sensory pathway comprises three main stages: reception, transmission, and interpretation in the brain [2]. In the case of tactile sensation, there are two primary pathways through which sensory information is transmitted from the receptors to the brain. The first pathway, the dorsal column pathway, involves sensory signals extending from the receptors to the dorsal horn. These signals ascend ipsilaterally in the spinal cord before synapsing in the medulla. At this point,

they cross over to the contralateral side and continue ascending to the thalamus via the medial lemniscus [1]. The spinothalamic tract involves sensory signals from nociceptors to the dorsal horn, where they synapse to secondary neurons, cross over to the contralateral side, and ascend to the thalamus via the anterolateral columns [14]. From there, the sensory information is conducted to the primary sensory cortex for further processing and interpretation [15] (Figure 2A).

Interestingly, although the two pathways have different functions and primary sensory modalities, they both involve a complex network of neurons and interneurons that allow for interaction and modulation of sensory information in the dorsal horn (Figure 2B).

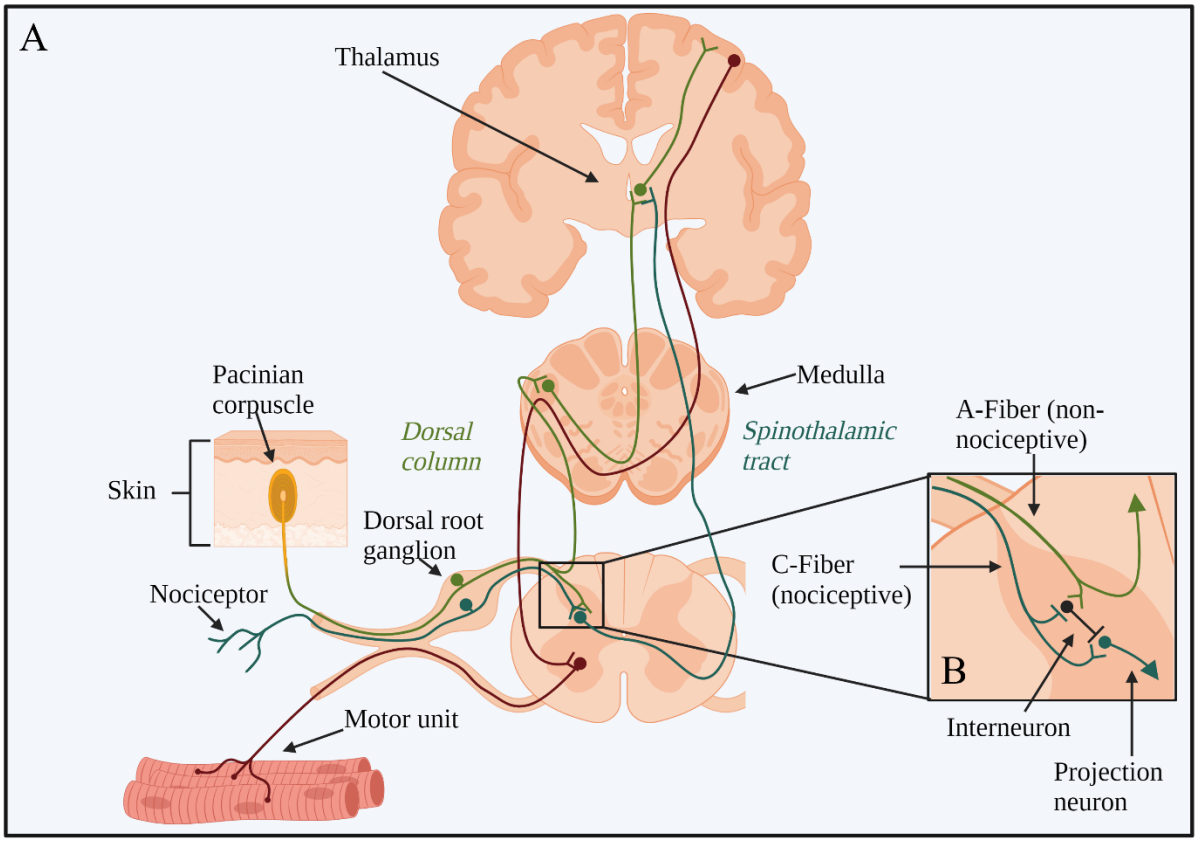

Figure 2 - Sensorimotor pathway. A comprehensive illustration of the sensorimotor pathways, highlighting the afferent and efferent pathways through the dorsal column and spinothalamic tract, as well as the complex connections within the dorsal horn of the spinal cord. The diagram also showcases the schematic connection to sensory receptors and muscles, emphasizing the integration of these components in the transduction, transmission, and processing of somatosensory information for perception and motor response.

The human body is covered with a wide range of receptors to achieve proper interaction with the environment. Regardless of their specific function, all sensory receptors convert physical or chemical signals into action potentials that can be transmitted to the nervous system. Various specialized receptor types respond to specific stimuli, such as photoreceptors in the retina of the eye to photons [16] hair cells in the inner ear to sound waves [17], and olfactory receptors

in the airways to odorants. Though these receptors are concentrated on specific body parts and limited by the relatively small size of the organs they are situated on, mechanoreceptors, responsible for detecting mechanical stimuli such as pressure, touch, and vibration, are spread over the whole body. These receptors are classified into four groups: two fast-adapting (FA I and FA II) and two slow-adapting types (SA I and SA II). Type I receptors have small, clear borders, while type II receptors have larger, less-defined edges. [18]. While slow-adapting respond to constant pressure, fast-adapting units mainly serve vibration detection. Meissner corpuscles (FA I) are primarily found in hands and feet and have the highest sensitivity around 50 Hz. Pacini corpuscles (FA II) are most commonly found on hairy skin, present on the limbs, trunk, and head, and have the optimal sensitivity between 200-300 Hz [19] (Figure 3). The cutaneous nerves that innervate these receptors depend on their location and arise from various neural roots [20]. For the upper limbs and the shoulder/neck area, nerve roots form seven distinct dermatomes: Cervical 3 (C3) to Cervical 8 (C8), Thoracic 1 (T1), and Thoracic 2 (T2). These roots are located in long bands around the arm and neck.

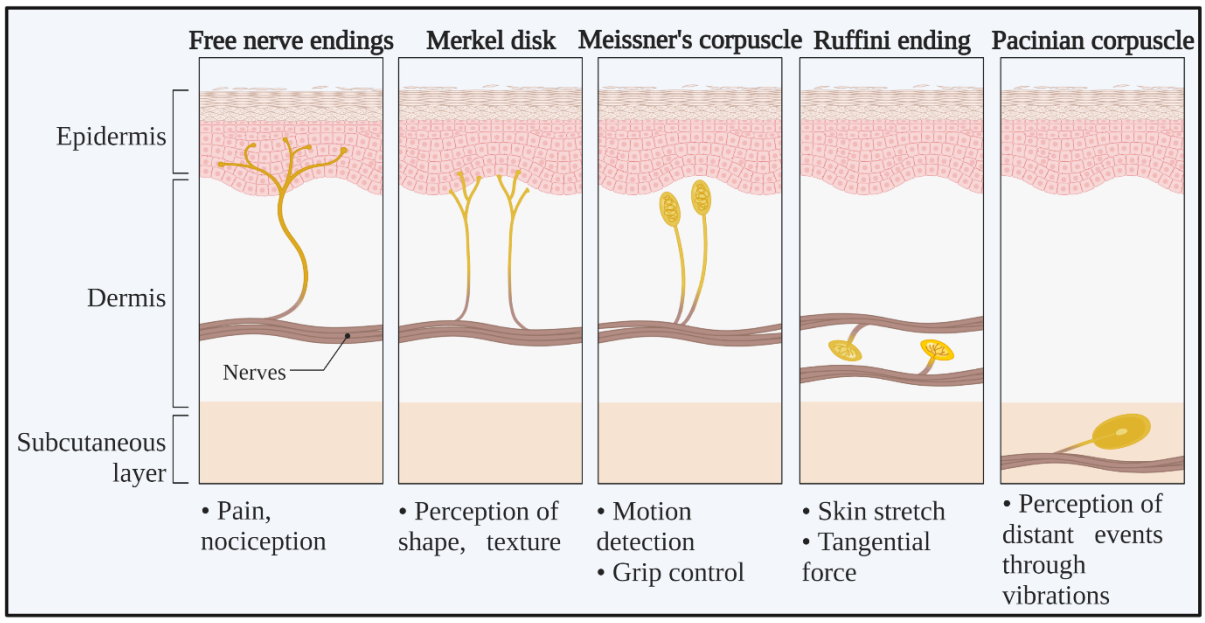

Figure 3 – Mechanoreceptors. Depiction of the diversity of cutaneous mechanoreceptors and free nerve endings, encompassing Merkel cells, Meissner's corpuscles, Pacinian corpuscles, and Ruffini endings. Each receptor type exhibits distinct morphological and functional characteristics, enabling the selective transduction of specific mechanical stimuli into neural signals for tactile perception and proprioception.

An additional kind of widespread receptor is nociceptors, which are responsible for initiating the sensation of pain [21]. Peripheral nociceptive axons terminate in unspecialized "free endings", which are categorized based on the properties of the associated axons [22]. While myelinated axons associated with somatic sensory receptors responsible for the perception of

innocuous mechanical stimuli have relatively fast conduction velocities, the axons associated with nociceptors are defined as either the Aδ group of myelinated axons (conducting at about 20 $\frac{m}{s}$), or the C fiber group of unmyelinated axons (conducting at velocities generally less than 2 $\frac{m}{s}$) [14]. Consequently, even though all nociceptive information is relatively slow, fast and slow pain pathways exist [21].

Aδ nociceptors are relatively fast-conducting nerve receptors that usually respond to intense mechanical or combined mechanical and thermal stimuli [21]. They have receptive fields made up of clusters of sensitive areas [22]. Polymodal nociceptors, connected to unmyelinated C fibers, generally react to thermal, mechanical, and chemical stimuli [21]. This categorizes nociceptors in the skin into three primary classes: Aδ mechanosensitive nociceptors, Aδ mechanothermal nociceptors, and polymodal nociceptors [14].

1.2 INJURY, REPAIR, AND REGENERATION

1.2.1 Kinds of injury

There are several origins of injury to peripheral nerves, such as accident, trauma, and other causes, which may result in partial or complete loss of sensory, motor, and autonomic functions and neuropathic pain [23]. Generically, they are divided into mononeuropathies if they affect only the functioning of one nerve and polyneuropathies in case of affecting several nerves.

Stretch is the most common kind of nerve injury [24]. Due to their collagenous endoneurium, peripheral nerves are inherently elastic, and stretch does not necessarily severe the nerve. In fact, to provide an indicative value, Sunderland and Bradley examined the mechanical properties of human peripheral nerve trunks. Here, they reported that the perineurium of median nerves, which are relatively large, could withstand a tensile force of 4.4 $\frac{\mathrm{kg}}{\mathrm{mm}^2}$ (43.2 MPa), while smaller cutaneous nerves had a tensile strength of around 2.2 $\frac{\mathrm{kg}}{\mathrm{mm}^2}$ (21.6 MPa) [25]. However, when nerves are close to bones, the required force may be reduced, but nerve continuity is usually maintained in these cases. Laceration, accounting for up to 30% of serious injuries, can lead to complete transections but often retains some nerve continuity. Compression is another common type of nerve injury, with unclear pathophysiology for motor and sensory function loss, as complete nerve continuity is preserved [25].

Injuries to the nervous system are classified according to severity and extent, resulting in different outcomes and varying degrees of recovery. Seddon [23] categorized nerve injuries using severity as the distinctive factor, into three types: neurapraxia, axonotmesis, and neurotmesis. Neurapraxia is the mildest form, involving temporary impairment due to local myelin damage. Axonotmesis involves disruption of the nerve axon and myelin, causing complete denervation. Neurotmesis is the most severe, with complete nerve disconnection and functional loss, often requiring surgical intervention for recovery. [23].

Sunderland [26] further divided Seddon's classification into five types, keeping neuropraxia and neurotmesis, and subdividing axonotmesis into three distinct types, depending on the degree of connective tissue involvement (Figure 4).

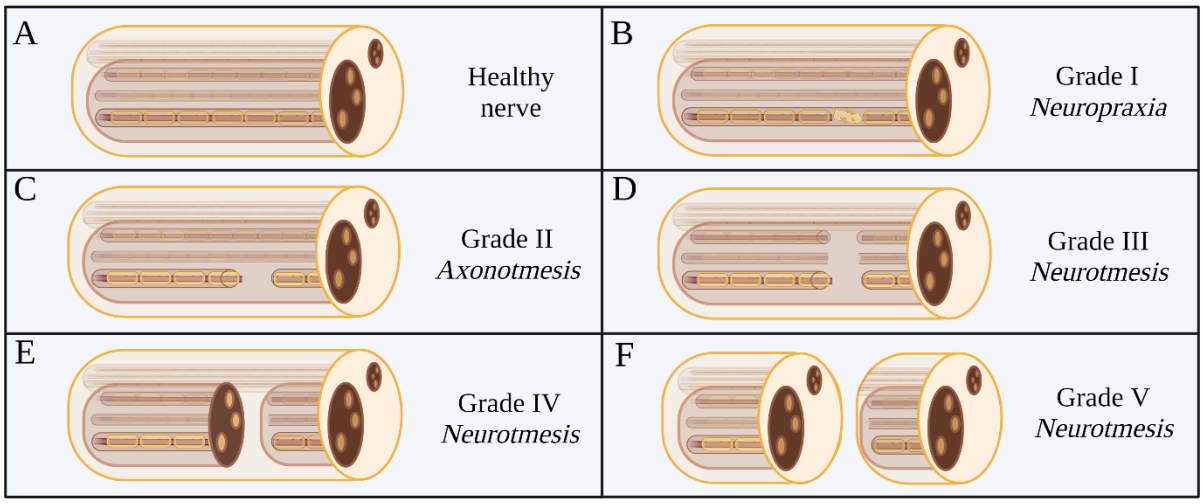

Figure 4 - Peripheral nerve injury classification Classification of peripheral nerve injuries according to Sunderland's system: **(A)** Healthy nerve. **(B)** Type I - Neurapraxia, **(C)** Type II - Axonotmesis with preserved endoneurium, **(D)** Type III - Axonotmesis with disrupted endoneurium, **(E)** Type IV - Axonotmesis with disrupted perineurium and **(F)** Type V - Neurotmesis with complete nerve transection.

1.2.2 Symptoms after PNI

Peripheral nerve injuries encompass a wide range of symptoms depending on the affected nerve, the severity of the injury, and the specific type of injury [23].

Motor dysfunction is characterized by muscle weakness or paralysis in the area supplied by the affected nerve or uncontrolled muscle contractions (fasciculations), depending on the extent of nerve damage. It may include muscle atrophy due to disuse or denervation [27].

Sensory disturbances may manifest as numbness, tingling, or paresthesia in the area innervated by the damaged nerve [28]. In peripheral nerve injuries, symptoms can be classified as positive or negative. Positive symptoms involve abnormal sensations or functions, while negative symptoms involve the absence or reduction of normal sensations or functions [29]. Positive symptoms include hyperalgesia (increased sensitivity to pain), allodynia (pain in response to non-painful stimuli), and paresthesia (abnormal sensations such as tingling or numbness). These symptoms are generally attributed to ectopic nerve activity from the damaged nerve fibers [30]. In contrast, negative symptoms, such as hypoesthesia (loss of sensation) or hypoalgesia (decreased sensitivity to pain), reflect the affected nerve fibers' reduced or absent function. These symptoms can result from disrupting normal nerve signaling due to the injury [31].

1.2.3 Repair and regeneration

The term "plasticity" refers to the ability of the nervous system to adapt and change in response to environmental conditions or injury. It occurs in the central and peripheral nervous systems and plays a crucial role in learning, memory formation, and recovery from neurological damage [32].

CNS plasticity occurs in the brain, where changes in synaptic connections between neurons are responsible for processes such as learning and memory [33]. For instance, long-term potentiation (LTP) is a well-known phenomenon that occurs when repeated stimulation of a particular synapse strengthens this synaptic connection and is thought to underlie the formation of memories [34].

Several studies have shown that plasticity in the PNS might occur at different levels, including modifications in the quantity and strength of synapses, modulation of neurotransmitter release, and property modifications of individual neurons [35]. For example, peripheral sensory

neurons can adapt to different levels of stimulation by changing the number of nociceptors or in response to changes in the amplitude of incoming inputs, leading to LTP and long-term depression (LTD) [36].

However, another aspect of peripheral nervous system plasticity is the ability of axons and dendrites to regenerate after injury, in which axonal regrowth and reinnervation of target tissues are essential steps in recovery [37, 38, 39, 40, 41]. Following injury, molecular and cellular events occur, including the activation of intrinsic growth programs in injured neurons, changes in the local environment, and the interaction between regenerating axons and their target tissues [35]. These processes are essential for restoring function after peripheral nerve injury (PNI). They can be influenced by various factors, such as the injury's severity, the individual's age, and the type of nerve affected [42].

In pain perception and management, understanding the CNS and PNS plasticity is crucial, as alterations in neural circuits can contribute to developing chronic pain conditions. For example, peripheral nerve injury can lead to the sensitization of nociceptors and the subsequent development of neuropathic pain, which is often challenging to treat [43]. Similarly, maladaptive plasticities in the CNS, such as the somatosensory cortex reorganization following amputation or deafferentation, have been implicated in generating phantom limb pain [44].

Following axonal transection, a sequence of pathologic events occurs peripherally and centrally in the nervous system caused by neuronal plasticity [40, 45].

Within hours of injury, several morphological alterations occur in neurons, such as the dissolution of Nissl bodies (chromatolysis), nuclear and nucleolar enlargement, nuclear eccentricity, cell swelling, and retraction of dendrites [46]. Simultaneously, a strong proliferative response occurs in the perineuronal glial cells (such as astrocytes and microglia), characterized by retraction of the dendritic arbor and reduction of synapses. This response is most likely produced by chromatolysis, i.e., morphological changes leading to functional isolation of the injured and non-functional neurons from the rest of the neuronal networks [46].

The intensity of the reaction depends on several factors such as whether the affected neurons are sensory or motor neurons [38]. The same applies to small sensory neurons in comparison to large ones [47]. The reaction is even more pronounced after avulsion or transection in ventral roots, as opposed to sciatic nerve injury [48].

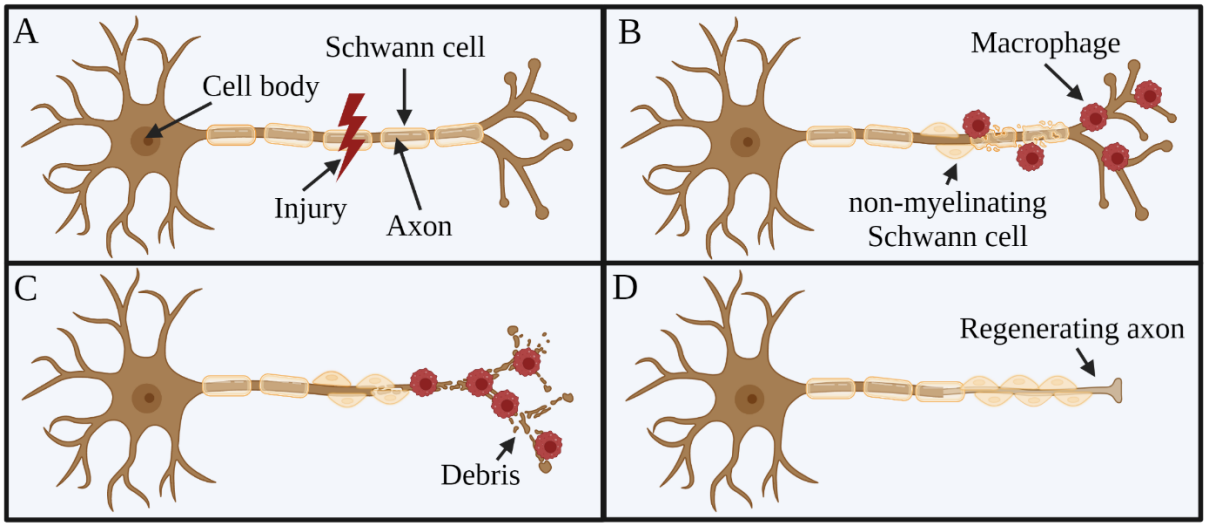

Figure 5 – Wallerian degeneration Illustration of Wallerian degeneration process, divided into four stages: **(A)** Initial nerve injury, **(B)** Myelin breakdown and macrophage recruitment, **(C)** Axonal degeneration, and **(D)** Schwann cell proliferation, remyelination and axonal regrow.

Signals generated by injury-induced electrical excitation and the subsequent signals are transmitted retrogradely from lesioned axons to the lesioned neuronal body. After axotomy, several molecular responses in the spinal cord are up-regulated, as is the case for growth-associated proteins [49], ion channels [50], and transcription factors [51]. Key factors include neurotrophic factors such as Nerve Growth Factor (NGF), Brain-Derived Neurotrophic Factor (BDNF), and glial cell line-derived neurotrophic factor (GDNF), which stimulate axon growth and survival through the activation of signaling pathways like the phosphatidylinositol 3-kinase (PI3K)/Akt and mitogen-activated protein kinase (MAPK)/extracellular signal-regulated kinase (ERK) pathways [52]. The cAMP pathway also plays a role in axon regeneration by modulating protein kinase A (PKA) and downstream transcription factors, CREB and ATF3 [53]. Furthermore, the mammalian target of rapamycin (mTOR) signaling pathway is involved in regulating cell growth, protein synthesis, and autophagy, contributing to axon regeneration after injury [54]. In fact, sensory neurons experience alterations in the expression levels of 11,163 out of 27,463 identified genes, with 52% of these genes showing increased and 48% decreased expression [55]. These may generate a more supportive phenotype directly or indirectly affecting neuronal survival and growth.

Conversely, responses not directly related to nerve regeneration are down-regulated (e.g., neurotransmitters, transmitter-related proteins, postsynaptic receptors, neurofilaments, and proteins involved in neurotransmission [56]). These regulations imply that neurons are shifted from a transmitting to a regenerative state, facilitating axonal regeneration and overall survival.

At the site of injury, residual axons undergo a mechanism called Wallerian degeneration [40]. Here, due to the loss of contact with the axon and under the stimulus in response to endogenous factors such as erythropoietin [57, 58, 59, 60, 61], the Schwann cells previously myelinating the damaged axons switch to a repair phenotype through a change in their transcriptome pattern (Figure 5B). Additionally, they recruit immune cells like macrophages and neutrophils to remove myelin debris [62, 63] and to fragment and disintegrate the axon (Figure 5C). In the meantime, nerve fibers from the proximal stump start elongating, in a phenomenon denominated as sprouting, attempting to reconnect with their original target tissue. After myelin debris clearance, the dedifferentiated Schwann cells proliferate on the remaining endoneurial tubes of the extracellular matrix, forming a hollow tube and providing a path for the regenerating axon sprouts to regrow, in which neurotrophic factors (e.g., Nerve Growth Factor (NGF) or Brain-Derived Neurotrophic Factor (BDNF)) play a key role (Figure 5D/ Figure 6B) [64, 24].

Once the regenerating axons have reached their target tissues, the Schwann cells begin to form new myelin sheaths around the axons, a process called remyelination. This restores the proper conduction of nerve signals and leads to functional recovery [65, 66]. As the regenerated axons reestablish connections with their target tissues, synaptic connections are reformed, allowing for the restoration of sensory and motor functions (Figure 6C) [35].

However, if an axon does not populate the endoneurial tube within four months, it starts to shrink, leading to axonal extension in random orientations, disorganizing remyelination, and forming a neuroma (Figure 6D) [67, 68].

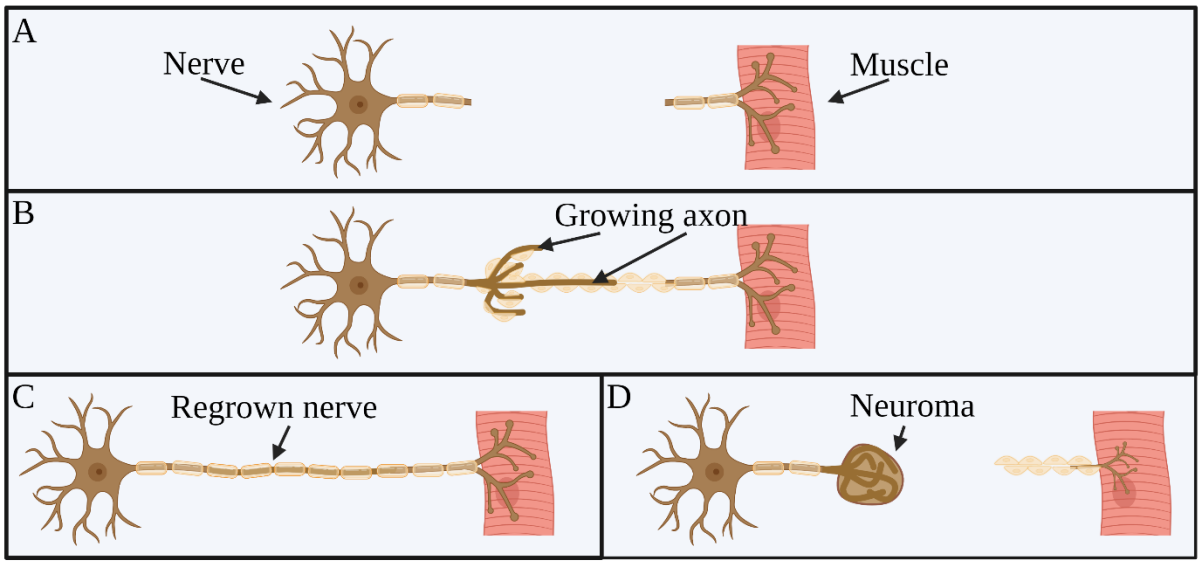

Figure 6 – Nerve regrowth and neuroma formation. The process of aberrant nerve regeneration, characterized by disorganized axonal sprouting, resulting in a tangled mass of nerve fibers and connective tissue at the site of nerve injury. **(A)** depicts the cut nerve, **(B)** shows the regenerating sprouts, and **(C)** illustrates the successfully regenerated nerve. At the same time, D portrays neuroma formation, which occurs when the nerve regrowth is disrupted or fails to occur correctly.

CNS response to altered peripheral input can happen in various ways. These include shifts in constant or response-triggered activity, the features of areas sensitive to stimuli, and connections within brain regions responsible for processing this information. These changes can influence how we perceive things, behave, think, or control our movements. Reorganization initiated by PNI can be seen in different parts of the nervous system, including the spinal cord, brainstem, relay nuclei, thalamus, and cortex. [69, 70, 71]. Peripheral nerves create links with neurons in the spinal cord's receptive field and grow into regions responsible for sending pain signals [72, 73], probably because the severed peripheral nerves stop sending sensory information to the dorsal horn in the spinal cord [74]. Furthermore, decreased inhibition of sensory transmission from the brainstem reticular areas [75] results in autonomous sensory activity from dorsal horn neurons.

In the 1980s, multiple research groups suggested that the brain's representation of the body surface in adult primates can change due to modifications in the activation patterns of sensory elements in the skin. When some of these sensory elements stop functioning because of deafferentation or amputation, a significant reorganization or "remapping" of the still-active inputs occurs [76, 77, 78]. Merzenich et al. [79] found that after severing the median nerve in monkeys, the cortical area originally representing the nerve was occupied by input from surrounding skin fields, showing cortical reorganization. Similar reorganization was observed in humans following amputation [80]. The underlying mechanism for the reorganization is still

not well understood. Studies using functional magnetic resonance imaging on rats with median nerve entrapment have shown that the sensory area of the affected limb expands in the early stages of injury to compensate for the loss of input and is reduced in the later stages [81].

In cases of peripheral nerve injury (PNI) in human upper limbs, neurons that previously received input from an arm prior to amputation later react to new inputs from the face, which intrude the neighboring somatosensory region associated with the arm (Figure 7) [82].

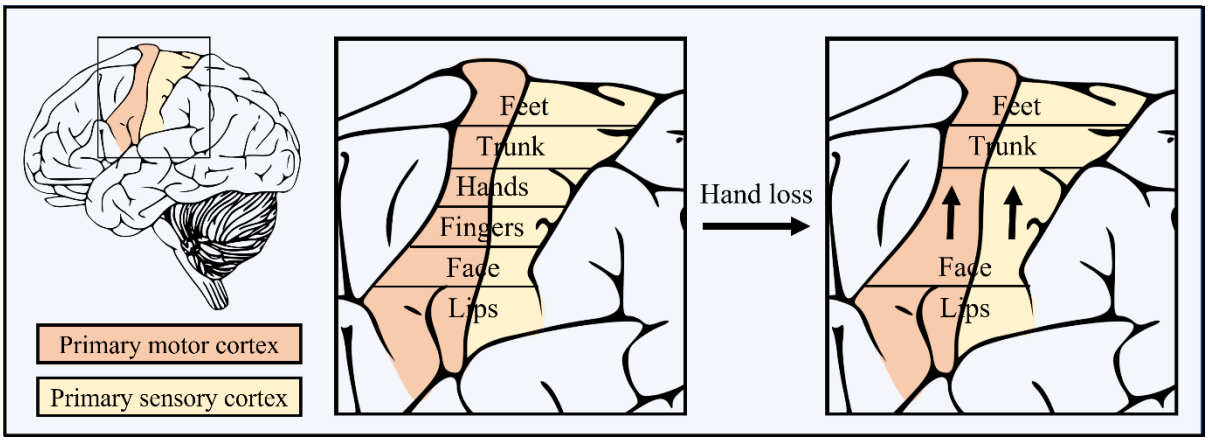

Figure 7 - Cortical reorganization. Sensory and motor representations of body parts are arranged in a pattern known as the cortical homunculus, which receives various sensory information (e.g., tactile, olfactory, or pain) from different body areas **[80]**. Following an amputation, the cortical region that once received sensory or motor projections from the amputated limb may start receiving respective sensory or motor input from adjacent cortical areas, expanding to occupy the region previously associated with the amputated limb **[83, 84]**(Figure inspired by **[85]**)

1.3 COMPLICATIONS AFTER PERIPHERAL NERVE INJURIES

1.3.1 The physiology of pain

Pain is a complex phenomenon that plays an essential role in protecting the body from potential harm and consists of two main categories, namely, nociceptive and neuropathic pain.

Nociceptive pain is the most prevalent form of pain and serves, when functioning properly, as a completely protective mechanism. It is a direct response to noxious stimuli perceived as potentially harmful or damaging to the body [74]. It is typically associated with tissue injury or inflammation, such as in trauma, surgery, or arthritis [86]. It arises from the activation of nociceptors present in various tissues, such as the skin, muscles, joints, and viscera [87]. Nnociceptors, when activated by stimuli such as mechanical, thermal, or chemical factors, convey signals via peripheral nerves to the spinal cord. Here, they form synapses with second-order neurons in the dorsal horn. These second-order neurons then project to the brainstem and

thalamus, ultimately reaching the cerebral cortex, where pain perception occurs [88]. Nociceptive pain can be further classified into two subcategories: somatic (originating from nociceptors in the skin, muscles, and joints) and visceral (arising from nociceptors within internal organs) [89].

For many years, the perception and modulation of pain has been a subject of debate. Among numerous theories, the gate theory of pain has earned considerable recognition due to its capacity to offer an extensive insight into the different facets of pain. First proposed by Melzack and Wall [88], the gate theory of pain suggests that pain perception is modulated at the spinal cord level through a balance of excitatory and inhibitory inputs. According to this theory, a "gate" mechanism in the dorsal horn of the spinal cord can either facilitate or inhibit the transmission of pain signals to the brain based on the interplay between small-diameter (C and Aδ) and large-diameter (Aβ) nerve fibers. Small-diameter nerve fibers are primarily responsible for transmitting pain and temperature sensations [22], while large-diameter fibers convey non-painful tactile information [14]. When there is an increase in non-painful stimuli, such as touch or vibration, the activity of large-diameter fibers increases, inhibiting the transmission of pain signals through small-diameter fibers [90]. This mechanism effectively "closes the gate" for pain signals, reducing pain perception.

In contrast to nociceptive pain, neuropathic pain results from injury or dysfunction in the nervous system, either in the CNS or PNS. Common causes include diabetic neuropathy, postherpetic neuralgia, and spinal cord injury [91]. This type of pain is often chronic and may persist even after the initial injury or disease has resolved [92]. It is characterized by abnormal sensations such as allodynia (pain caused by ordinarily non-painful stimuli) and hyperalgesia (increased sensitivity to painful stimuli) [93]. These symptoms arise from a complex interplay of maladaptive changes in the PNS and CNS, including alterations in ion channel expression, neurotransmitter release, and glial cell activation [30].

The pathophysiology of neuropathic pain is complex and involves both peripheral and central mechanisms. At the peripheral level, nerve injury may lead to ectopic activity in primary sensory neurons, generating spontaneous pain signals [94]. Additionally, inflammation at the site of nerve injury can cause the release of pro-inflammatory mediators, sensitizing nociceptors and promoting pain. In the CNS, synaptic plasticity and neuronal excitability alterations contribute to the maintenance and amplification of pain signals [95]

1.3.2 Pain after PNI

After PNI, 70% of the patients suffer from chronic pain, either isolated to the remnant of the limb itself (Residual Limb Pain, RLP) or as Phantom Limb Pain (PLP), perceived in the absent limb [96]. The disruption of the usually closed sensorimotor loop after amputations and nerve avulsions leads to several maladaptive processes in the PNS and CNS.

Proximally to the injury site, within the neuroma, many regenerated axons are surrounded by an abnormal myelin sheath that exhibits variable degrees of thickening [97]. This results in the accumulation of Na^+ channels [98], a change in the expression of transduction molecules [30], and the development of non-functional connections between axons called ephapses [94], all phenomena altering the electrophysiological properties of axons. As a result, spontaneous afferent input to the spinal cord increases, rendering the axons hypersensitive to mechanical, chemical, and physical stimuli (nociceptor sensitization) [99, 72]. Furthermore, this hyperpathia might be intensified by the factors released during immune reactions (e.g., TNF-α) [93, 100, 101].

Moreover, during long-lasting inflammation, collagen and mature myofibroblasts might invade the neuroma. These elements can then become the main cause of mechanical irritation on the regenerating nerves. Then, these nerves send aberrant signals through afferent pathways and the posterior horn to the brain and generate persistent painfulness, intensifying the perception of painful stimuli (hyperalgesia) and lowering the pain threshold (allodynia), in a process known as peripheral sensitization [102, 103, 104, 105, 106]. These changes lead to and contribute to neuroma pain. Interestingly, not all patients with neuroma also suffer from neuroma pain. Buch et al. [107] attempted to find a link between pain and neuroma swelling identified through ultrasound but found that swollen neuromas were equally present in amputees with and without pain. They interpret that an inflammatory response in the neuromas, causing swelling, may not be the cause of pain. Also, attempts to correlate the size of neuromas to the patient's pain level were unsuccessful [108].

Opposite to sensitization, distally to the injury site, as the sensory neurons lose connections to the receptors, patients experience no or reduced sensitivity (hypoalgesia or analgesia). This loss of sensation elicits a second pain quality, known as deafferentation pain [109]. Hitherto, the mechanism through which deafferentation pain initiates is under debate.

The previously mentioned gate control theory [88] suggests that non-nociceptive afferents can reduce the flow of painful information to the brain by activating spinal inhibitory neurons, which requires a balance between the inputs, disrupted after PNI. Due to continuous input, neuroma-driven peripheral sensitization can initiate and support central sensitization in the dorsal horn. Here, injured sensory neurons in the dorsal root ganglion undergo significant alterations in transcription that alter their membrane properties, growth, and transmitter function. It is believed that this mechanism might be at least maintaining or sustaining deafferentation pain [95].

Nevertheless, the mechanisms described cannot fully explain the pathophysiology of deafferentation pain. Its extreme form, PLP, is present in 75% of patients immediately after amputation, even before a neuroma could have formed [110].

More recently, studies report a relationship between PLP and a remapping of the somatosensory cortex after injury. The main evidence supporting this idea is the relationship between pain and the reorganization of sensorimotor cortical maps in the brain. This has been demonstrated by various techniques, such as having participants perform imagined and phantom limb movements while their brain activity is recorded using functional magnetic resonance imaging [111, 45, 44].

The mechanism of PLP has long been debated, with two leading models attempting to explain its occurrence. The maladaptive plasticity model proposes that PLP initiates from functional reorganization in the primary somatosensory cortex (S1). In this process, nearby cortical areas take over the region that no longer receives input from the missing limb. Conversely, the persistent representation model suggests that higher PLP levels are associated with a maintained representation and increased activity in the sensorimotor cortex corresponding to the absent limb [112].

Makin and Flor [113] attempted to reconcile these models by presenting them as complementary processes in S1. They propose that other brain structures may be similarly crucial as S1 in understanding PLP, as the current models are inconclusive.

Weiss et al. [112] propose the concept of “predictive coding” to provide a more comprehensive understanding of PLP. This approach hypothesizes that perceptual processes involve a continuous interaction between the brain's expectations and actual sensory evidence. They

introduce a three-step theory of the emergence and maintenance of PLP, incorporating predictive coding and considering the processing of somatosensory information beyond S1.

1.4 CURRENT MANAGEMENT OF PNI-RELATED PAIN

Due to the diversity of its origin, there is no overall procedure to treat PNI-related pain, as the different pain qualities impact each other. The different qualities must be identified to design an appropriate therapeutic strategy. Effective management of PNI-related pain involves a combination of pharmacological and non-pharmacological treatments and non-surgical and surgical approaches [114, 115]. In contrast, several techniques have been proposed to treat neuromas and neuroma pain with more or less efficacy [116, 117, 118].

1.4.1 Pharmacological treatments

Pharmacological interventions for PNI-related pain aim for nociceptive inhibition or membrane potential stabilization. These include the use of medications like NMDA antagonists [119, 120], antidepressants [121, 122], anticonvulsants [123, 124], capsaicin [125, 126], calcitonin [127, 128], and opioids [129].

Evidence for sodium channel blockers was inconclusive, but some are suggested to be effective for specific subgroups of patients. Despite the efficacy of drugs with different mechanisms, effect sizes are minor, and side effects are common, often leaving many patients without sufficient pain relief. Combination therapy is often used when a single drug is only partially effective [120, 119, 130, 131].

1.4.2 Non-pharmacological treatments

Due to the high number of pharmacological side effects, non-pharmacological treatments receive higher approval rates from the clinical community.

Non-surgical treatments include electrical stimulation, to induce muscle contractions, preventing atrophy during reinnervation [132, 133, 134], infiltration, referring to injecting a therapeutic substance, such as a local anesthetic, corticosteroid, or sclerosing agent, directly into or around the affected area [135, 136, 137], or mirror therapy, first introduced in 1996 [138] and consisting of reflecting the patient's intact limb to the covered stump. This last method was designed to provide visual feedback of phantom limb movements to a patient, therefore counteracting its absence.

In contrast, various surgical approaches, specifically for neuromas, have been described in the literature as a major determinant of neuropathic pain and the predominant driver of RLP [116, 117].

If the distal nerve end is available, nerve reconstruction can be performed using various techniques, such as hollow tube constructs [139], autografts [140], or allografts [141].

When the distal nerve end is unavailable, most techniques focus on mitigating the effects of the positive and negative symptoms after PNI by separating the nerve from external stimuli such as pressure or mechanical irritation, by implanting the proximal nerve into adjacent tissue, as bone, veins, or muscle [142, 143, 41]. These techniques have been shown to be effective for both upper and lower-extremity neuromas, although their success is not universal [144].

Also, if the distal nerve is not accessible, several techniques have been explored for nerve treatment, including centro-central neurorrhaphy, which involves connecting adjacent nerves [145, 146, 147]; relocation nerve grafting, where nerve allografts are used to guide nerve regeneration towards less painful destinations [148]; nerve capping, which uses a cap on the terminal end of the nerve to reduce painful regrowth [149, 150, 151]; and Regenerative Peripheral Nerve Interface (RPNI), where a free muscle graft is wrapped around the terminal nerve stump to allow muscle innervation by the regenerating nerve [152].

However, no surgical technique could show consistently effective or superior treatment, and the success of these procedures mentioned earlier is limited to reducing symptoms' intensity [118]. Targeted Muscle Reinnervation (TMR) has been proposed as a possible alternative. Initially performed to allow physiological control of advanced myoelectric prostheses [153], TMR involves the removal of the terminal neuroma and the freshening of the nerve, which is then coapted to a newly surgically divided motor nerve located nearby. The fascicles, which are prepared to regenerate, grow down the motor nerve and enter the newly denervated muscle to facilitate its re-innervation [154, 155, 156, 157]. Within the muscle, some fascicles establish connections with motor endplates, while others establish connections with numerous sensory end organs, such as proprioceptors, allowing for bionic reconstruction and the desired improvement prosthetic control [158, 159, 118]. A key feature that differentiates TMR from other neuroma treatments is its method of guiding the bundles of mixed primary and sensory nerves toward their intended nerve receptor targets.

Despite early concerns that TMR could produce or intensify pain, studies have shown that TMR patients experience less pain after the procedure [159]. In addition, a preclinical animal model confirmed the histologic restoration of myelinated nerve morphology with TMR [160]. By giving the regenerating fascicles a specific goal, TMR serves to promote healing of the amputated nerve ending rather than just masking the injury.

1.4.3 The role of the sensorimotor incongruence and restoring the loop

Sensorimotor incongruence refers to the mismatch between the brain's expectations and the actual sensory feedback received from the affected body part [161]. This discrepancy can lead to various issues, including pain and impaired motor control, as the damaged nerves disrupt the normal communication between the brain and the injured area [161]. Deafferentation after PNI provokes the disruption of the normal communication between the nervous system, muscles, and receptors [82].

Even if still under debate (see [162, 163] for reviews), closing the disrupted sensorimotor loop might have potential benefits in terms of reducing deafferentation pain, improving the function of prosthetic limbs for amputees, and treating neuroma [118, 164]. In fact, TMR may be able to reverse the pathologic cortical reorganization associated with PLP [165, 166], which is suggested to happen by restoring physiological continuity (through the restoration of myelinated nerve morphology) after surgery [160], and therefore, closing the loop [167, 118, 159].

TMR has existed for over ten years [154, 155]. It is noteworthy that patients who have had nerves redirected to their chest muscles report feeling their hand on their chest wall, indicating the potential for targeted sensory reinnervation (TSR) [168]. Studies have demonstrated that TSR of residual nerves in the upper limb can produce genuine sensations from the missing limb [169]. This sensory feedback is crucial for further improving prosthetic control and reducing phantom pain [170].

In cases where surgical restoration is not a viable solution, sensory substitution comes into play. Sensory substitution aims to provide alternative or supplementary sensory feedback to compensate for the lost or altered sensation after PNI. By using other intact sensory modalities or assistive devices, sensory substitution may help to reduce the mismatch between expected and actual sensory feedback, ultimately improving sensorimotor integration and functional outcomes.

As with mirror therapy, overall embodiment and reduction of PLP seem to be intense when additional cutaneous feedback is provided by the prosthesis to the residual limb. Furthermore, there is a significant increase in the functionality of the prosthesis by a feedback mechanism, e.g., on the grip strength and walking parameters [171, 172, 173, 174, 175, 176, 177, 178, 179]. A prosthesis with a feedback function shows potential as a therapeutic tool for reducing PLP by addressing the sensorimotor incongruence that presumably leads to PLP after amputation [37, 83].

Several advanced prosthetic hands are available on the market, providing numerous movable joints, an extended range of movements, and improved dexterity of fingers [180]. Nevertheless, the lack of sensory feedback for the user is still a significant drawback of today's prostheses [181, 182].

In addition to pain management, especially for hand movements, the interaction between sensibility and motor functions is fundamental [37, 183, 184]. Moreover, there might also be a potential benefit of providing sensory feedback to paretic limbs to reduce their deafferentation pain. In their case, no orthotic devices that provide feedback are available, as they are supposed to be purely supporting. However, pathological conditions, such as stroke, brachial plexus injury, cerebral palsy, Parkinson's disease, and amputation, can cause distinct somatosensory disabilities. Schneider et al. observed that patients with Parkinson's disease present significantly higher difficulties distinguishing between two points on their index finger compared to healthy individuals, while no significant difference was measured on the lower arm [185]. Tyson described tactile impairment as more common than proprioceptive impairment after stroke [186]. Like amputations, tactile problems in brachial plexus injuries depend on the level of the injury [187]. Sensory dysfunctions can lead to additional difficulties. For example, Auld and colleagues found that in children with one-sided cerebral palsy, about 30% of upper-limb motor function problems are due to spatial touch deficits [188]. In addition, sensation also plays a crucial in body image and is necessary for experiencing body ownership and pain [189, 190, 172].

The investigation of tactile perception has, up to now, used brief mechanical stimulation, its most elementary form. Next to the common usage in everyday devices, such as smartwatches and mobile phones [191, 192, 193], advanced prosthetic and orthotic devices frequently incorporate vibration feedback to convey multiple functions that could be useful in neuropathic pain management, among others, modality transitions and velocity adjustments [194].

Nevertheless, research using elaborate tactile stimuli generally targets single regions of the arm [195], and the region of injury and the accompanying symptoms might significantly alter the patient's capacity to perceive vibrations at the designated stimulation location. Consequently, a comprehensive understanding of human vibration perception is essential for optimizing these technologies.

After peripheral nerve injury, patients experience various pain qualities and sensory alterations. These include increased sensation proximal to the injury, such as hyperalgesia and allodynia, and diminished sensations distally, such as hypoalgesia. Reestablishing the interrupted sensorimotor loop is a promising strategy to reduce pain, for instance, by using feedback systems like vibrotactile stimulation.

Previous investigations on vibration have primarily focused on the lower arm and hand [196, 197, 198], localized areas within prominent dermatomes [199], or predetermined arrays within specific arm regions [200]. However, it is imperative to understand these phenomena in a holistic map and across diverse patient populations to extend the potential of tactile stimulation to them. Despite extensive research, the sensory capacity for vibration perception remains incompletely explored in the arm.

1.5 MOTIVATION FOR THE STUDY

The initial focus of this thesis is to examine the effects of sensory loss distal to the injury on the perception of mechanical vibration. As a preliminary step, the baseline perception of vibration feedback in the healthy arm will be assessed (section 4.1). Then, it explores the consequences of peripheral nerve injury (PNI) when applying vibration proximal to the injury site in amputees and distal to it in BPI subjects (section 4.2). This will help investigate the potential of vibration feedback as a sensory substitute following PNI to complete the sensorimotor loop (section 4.3).

Due to the lost connection between the receptors and the brain, sensory deficits are expected distally from the injury site. As shown with TMR, sensorimotor restoration is a critical factor in reducing neuroma pain [118], which affects 15% of patients after PNI (pooled prevalence, ranging from 3% to 60% depending on the study) [201, 202]. Nevertheless, not all individuals with a neuroma suffer from neuroma pain, suggesting additional local factors to the lost connection. Therefore, owing to the presumed role of inflammation in neuroma pain, the second aspect of this thesis involves a comparative analysis of various inflammation-related cells, including the Schwann cell area, macrophage density, and T-lymphocyte density relative to the nervous tissue area, comparing controls with neuromas, to further distinguish between patients with and without neuroma pain and correlate these factors to neuroma pain.

2 METHODS

2.1 PSYCHOPHYSICAL ANALYSIS

2.1.1 Ethical approval

Ten healthy, able-bodied subjects, five persons with transradial amputations, and six persons with a plexus brachialis injury (presenting a C5/C6 avulsion) took part in the study. All participants provided their consent by signing a form that was approved by the ethics committee at the University Medical Center Gttingen (Ethics Number: 26/6/20).

2.1.2 Experimental setup

The vibrotactile sensation ability for each of the six dermatomes of the arm-shoulder region, namely C3, C4, C5, C6, T1, and T2, was investigated. The tactile sensations were elicited using twelve vibro-tactors placed in pairs on each dermatome. The participant's response to the vibrations was measured using three different assessment methods.

Throughout the experiments, participants sat at a desk with a computer screen, wearing noise-canceling headphones. White noise was played when the tactors were active to prevent hearing the vibrations. This ensured that the participants' decisions were based only on touch sensations (Figure 8A/B). As user interface for control, a modified joystick was connected to a PC via a USB port (the spring was detached to achieve an ideal motion translation; HT Series, CH Products, USA). The PC operated the output of the stimulation channels, which were attached to twelve high-end, state-of-art vibration motors based on voice-coil technology that generate vibrations perpendicular to the skin (C2-tactor, Engineering Acoustics, Inc., USA; diameter: 30.5 mm). These tactors provide a certain degree of independent control over both frequency and intensity, though the two parameters are coupled through the resonance effect (modulation of the frequency does not affect the amplitude; however, modulation of the amplitude will, at some point, affect the frequency). They could be adjusted with 0.38% amplitude precision (arbitrary values between 0 and 255, from now on expressed in percentage of the maximal amplitude for easier reference) at their optimal operating frequency of 230 Hz [203]. The limb was divided into three segments, each evaluated separately, defined as the lower arm (mostly innervated by T1 and C6), upper arm (mostly innervated by T2 and C5), and shoulder (mostly innervated by C3 and C4). The tactors were positioned on each dermatome of these segments, using relevant anatomical features. The distance between the

processus styloideus ulnae and the armpit *(PSU-AP),* between the armpit and the *articulatio acromioclavicularis (AP-ACC),* and between the shoulders *(*SH*)* was measured. The tactors were then placed as follows (Figure 8C):

1. Distal and proximal T1, C6: $\frac{1}{3}$ $(PSU - AP)$ and $\frac{2}{3}$ $(PSU - AP)$ from the *processus styloideus ulnae, correspondingly*
2. Distal and proximal T2, C5: $\frac{1}{3}$ $(AP - ACC)$ and $\frac{2}{3}$ $(AP - ACC)$ from the *armpit, correspondingly*
3. Dorsal C4 and C3: $\frac{1}{3}$ $(\frac{1}{2}(SH))$ and $\frac{2}{3}$ $(\frac{1}{2}(SH))$ from the *articulatio acromioclavicularis correspondingly*- To avoid the clavicle, the placement had to be marginally adapted on the ventral part of C4 and C3.

Moreover, every two tactors were at every moment separated by at least a tactor-diameter, such that the minimum distance between the centers of vibration was a minimum of 61mm (Figure 8D). Additionally, on the lower arm, the tactors used were proximal on C6 and T1 because the anatomical distance between distal points could (for some subjects) be lower than the minimally required distance for the simultaneous application of stimuli (i.e., lower than 61mm). The choice of distal locations on C5 and T2 for the upper arm was made to prevent uncomfortable sensations caused by continuous vibrations close to the axilla, which is where the ulnar nerve runs near the surface. The ventral locations on C3 and C4 were used on the shoulder because the sensation threshold is significantly lower than on the dorsal part.

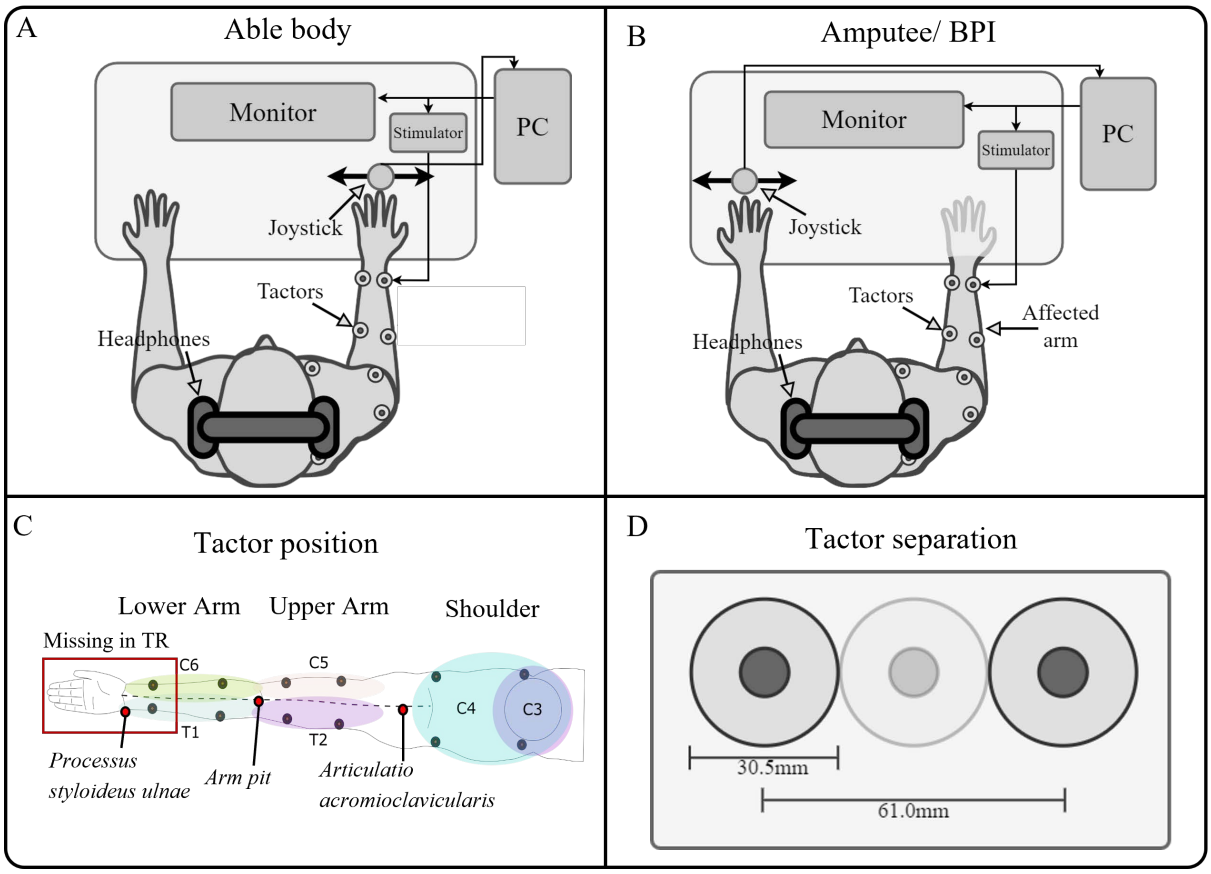

Figure 8 - Psychometrics setup (A/B) The experimental setup included a PC for data recording, visual instructions, and tactile stimulation; a stimulator to control the tactors; and a joystick as the user interface. Participants wore noise-canceling headphones with white noise playing whenever the tactors were active to mask the vibration sound **(A)** Able body participants used the stimulated arm to control the joystick, **(B)** while amputees and BPI participants used their healthy arm. **(C)** In total, twelve tactors were placed on the arm and shoulder/neck, stimulating the dermatomes innervated by cervical spinal nerves C6 (not in TR amputees), C5, thoracic spinal nerves T1 (not in TR amputees) and T2, and cervical spinal nerves C3 and C4. This allowed for mapping tactile sensations to vibrations across the entire arm. The arm was divided into three sections, each evaluated separately: lower arm (mainly connected to T1 and C6 nerves), upper arm (mainly connected to T2 and C5 nerves), and shoulder (primarily connected to C3 and C4 nerves). **(D)** Moreover, it was ensured that two tactors were always placed at a distance of a tactor-diameter, such that the minimum distance between the vibration centers was at least 61mm (modified from **[204]**).

2.1.3 Experimental tasks and protocol

Three tasks were conducted to assess the ability to sense vibrations in the lower arm, upper arm, and shoulder. The tasks took place in three sessions, each focusing on a specific arm-shoulder area and lasting 1-2 hours. There was a break of at least one hour between sessions, or they were held on separate days. The tasks are summarized here and explained in greater detail below:

1. The *tactile sensation threshold* was assessed by progressively increasing the amplitude of each of the twelve vibro-tactors independently, i.e., quantifying the sensation threshold in four points of each of the arm regions mentioned above.

2. The *Weber fraction* [205], which describes the percentual increment of the amplitude needed to be perceptible for the subject, and the number of distinct intervals that the subject could perceive. This was done by evaluating the *just noticeable difference* in amplitude between two separate vibration stimulations delivered one after the other on the same spot (four points per arm region).
3. Finally, a *compensatory tracking task* was used to study the subject's ability to distinguish continuous stimulation on the two main dermatomes of each arm segment. In this case, a method called frequency identification of human operators was employed, based on McRuer and Weir's control theory [206], which was already used by Dosen et al. [175] for similar objectives. The human transfer functions collected in this phase enabled estimating the magnitude and phase delay of the participant's response to changing stimulation signals. This test was conducted only once per arm region, resulting in a total of three data points per participant.

2.1.3.1 Sensation threshold

The method of limits was used to determine the sensation threshold (ST) for each stimulation side [17]. The experimental task began by randomly selecting one of three arm-shoulder regions. One tactor was then selected from a randomly generated list of four, with the others remaining off. The intensity of the selected tactor was increased in steps of 0.78%, starting from 0% amplitude, with a break of 0.5 seconds between consecutive stimuli. The subject reported the first time they perceived the stimulation, after which one additional stimulus was applied at the maximum amplitude. The subject then identified the location of the stimulation on their arm. This process was repeated for each of the four tactors in each of the three arm-shoulder regions for a total of 12 measuring points. The maximum intensity level was set at 100% because the vibrotactile devices did not cause any pain. The testable intensity range for each site was defined as *[STi, 100%],* where *i=1, ..., 12*. For able-bodied participants, the tactors were placed on the dominant arm, while for patients, the tactors were placed on the affected side, and the joystick was handled with the opposite arm. The sensation threshold was not measured on the distal lower arm of the amputees, and it was not defined as 100% to avoid distorting the performance of the proximal lower arm. The overall procedure took approximately one hour and was completed in one session.

2.1.3.2 Just noticeable difference

In the second task, the just noticeable difference (JND) was measured, which is the smallest change in amplitude between two sequential stimuli that a participant can detect. The order in which the arm-shoulder areas were assessed was determined randomly. In each chosen area, four vibrating devices were placed on the related dermatomes of the proximal and distal (or ventral and dorsal for the shoulder) sides. As in the previous task, one device (i.e., one dermatome) was randomly chosen to be active. The experimental task consisted of applying two consecutive stimuli of varying intensities to the selected dermatome: a base (lower and constant) and a test (higher and variable) stimulation. Each stimulus lasted for 0.5 seconds, with a 1-second pause between the two stimuli (Figure 9A). The two stimuli's order was randomized. After every two stimuli, the subject was required to select the stimuli with higher intensity by turning the joystick left (implying the first stimulus had higher intensity) or right (signaling the second stimulus had higher intensity). Put simply, the subject had to identify which of the two stimuli was the test stimulus. This process was repeated until ten reversal points were reached (see below). During the experiment, the baseline stimulus within the selected stimulation site remained constant in intensity, while the intensity of the test stimulus was adjusted using the staircase method. The baseline intensity was fixed at $ST_i + 0.15 * (100\% - ST_i)$, while the test stimulus was initially set to $ST + 0.9 * (100\% - ST)$. If no sensation threshold was measured at any point, it was defined to be 100%.

The baseline stimuli were increased by 15% of the perceivable range, as continuous stimulation on the same spot was expected to shift the sensation threshold upward due to adaptation effects, making the baseline stimuli undetectable. Similarly, the first test stimulus was reduced to 90% of the testable range to avoid overstimulation and slow the overall adaptation to the stimuli. When the participant accurately identified the higher intensity stimulus (i.e., the test stimulus), the intensity of the subsequent test stimulus was decreased by 1.18% of the maximum amplitude. In contrast, if the participant made an incorrect identification, the intensity of the following test stimulus was increased by 3.53% (Figure 9B). The oscillation point was determined as the average intensity preceding all stimuli with erroneous identifications throughout all trials, or as the average of ten reversal points (Figure 9C).

To determine the just noticeable difference (JND) of the chosen stimulation site, the difference between the oscillation point (OP) and the baseline intensity was calculated as a percentage of

the maximum amplitude., $JND = \frac{OP-(ST+0.15*(100\%-ST)}{255} * 100$ ($\frac{x}{255} * 100$, because max(Amplitude) = 255, and it is preferably expressed as a percentage). This process was repeated for each stimulation site (i) in each arm-shoulder region, yielding twelve distinct measurements of the JND_i, *i=1, ..., 12*. If the participants could not feel anything in the whole range of a dermatome, the JND was defined as 100, and no further experiments were conducted on that dermatome.

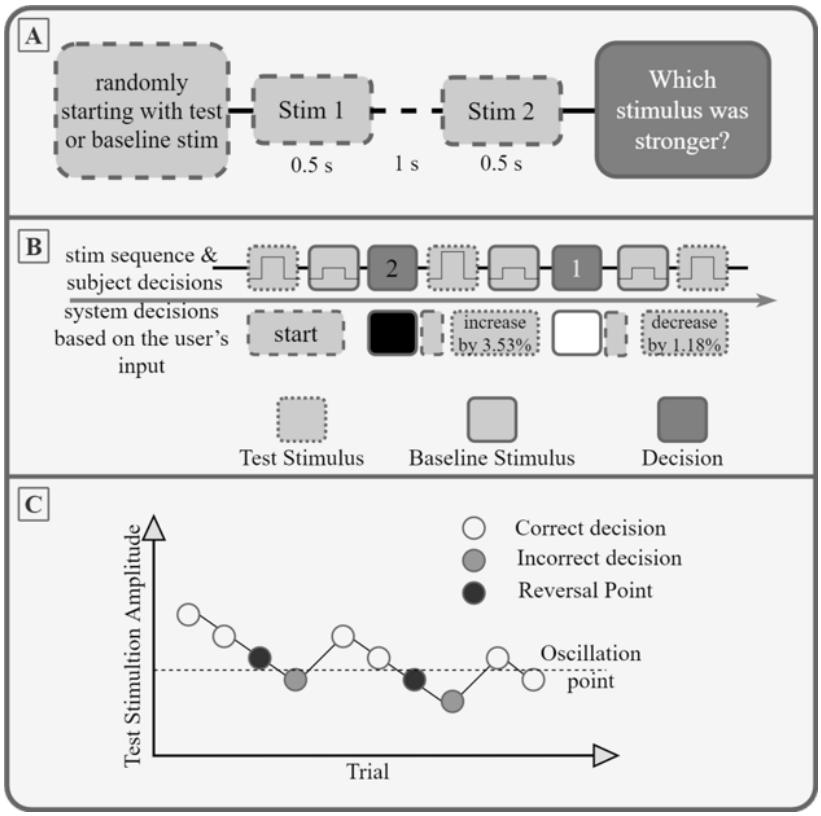

Figure 9 - Just noticeable difference. (A) The experimental protocol was as follows: the order of whether the first stimulus was the test stimulus or the baseline stimulus was chosen randomly. Each stimulus had a duration of 0.5 seconds, and there was a one-second interval between stimuli. Following the presentation of the second stimulus, the participant was required to indicate (via joystick selection) whether the first or second stimulus was stronger in amplitude. An exemplary sequence of trials is depicted in panel **(B)**, with incorrect decisions resulting in a 3.53% increase in test stimulus amplitude and correct decisions resulting in a 1.18% decrease. **(C)** The amplitude of the stimulation was reduced after each correct decision and increased following an incorrect decision. A reversal point was defined as the last correctly recognized amplitude before an incorrect decision. The oscillation point was determined as the average amplitude of ten reversal points (from **[204]**).

2.1.3.3 Closed loop compensatory tracking

A compensatory tracking task was used to evaluate the participant's ability to distinguish between dynamically changing stimuli. In this task, the participant received two-dimensional feedback on their performance as they tried to track a 90-second reference signal using a joystick input interface. The reference signal was a pseudorandom multi-sine wave consisting of nine components ranging from 0.1 Hz to 2 Hz. The five sine waves with higher frequencies (>0.4 Hz) had half the power of all other components combined, and the signal ranged from -1 to 1. The tracking error was determined as the difference between the user input (i.e., joystick

position) and the reference signal. This error was communicated to the participant through either two tactile units placed on different dermatomes of the chosen arm-shoulder area or visual feedback on a computer screen. The participant was first trained on the task using only visual feedback. The error was displayed as a red circle moving along a horizontal axis on the screen, with a green vertical line indicating zero error. The participant was instructed to move the joystick to keep the red circle on the green line. Once familiar with the task, they completed ten additional trials using visual feedback only.

Next, tactile vibration feedback was combined with the visual feedback. The participant was asked to perform the task three more times, focusing on the relationship between the movement of the red circle on the screen and the sensation of stimulation. In the tactile vibration feedback condition, the direction of the error was represented spatially by two tactors, and the stimulation strength was proportional to the error size. The participant's goal was to minimize the intensity of the stimulation by moving the joystick in proportion to the perceived stimulation intensity and in the opposite direction from the active stimulation site.

The evaluation process began after the subject had been trained to use tactile feedback only for at least three trials. They were asked to complete ten additional trials, and a 1-2 minute break was introduced after each trial to avoid fatigue. The evaluated arm-shoulder regions were randomly selected for each trial. The overall process resulted in a total of thirty data points for the vibrotactile condition (ten per arm-shoulder region) and an additional ten data points for the visual condition.

To analyze the data, the tracking correlation coefficient for each trial was calculated. The coefficient measures the similarity between the subject's input and the reference signal, with a value of 1 indicating perfect tracking. The subject's ability to differentiate between the dynamic stimuli was assessed by comparing the tracking correlation coefficients between the vibrotactile and visual conditions. If the coefficients were significantly higher in the vibrotactile condition, it indicated that the subject was better able to differentiate between the stimuli with the addition of tactile feedback.

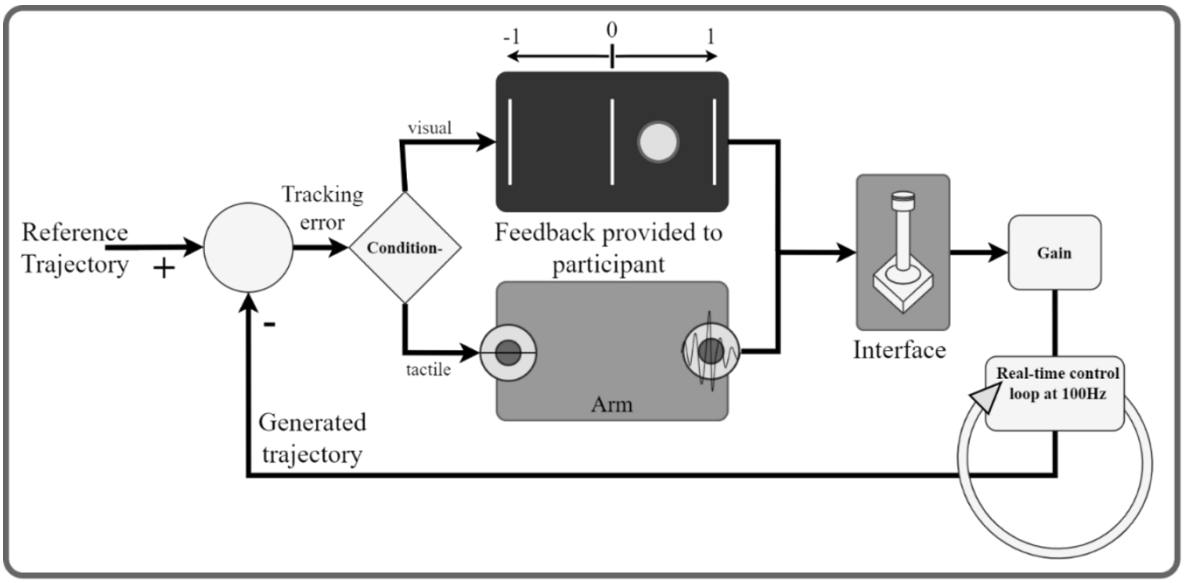

Figure 10 - The real-time control loop. The participant (human operator) operator is considered to be a component of a dynamic system. The aim is to produce a signal with the joystick that minimizes the tracking error in relation to a predetermined reference trajectory. The operator is provided with feedback through both tactile and visual modalities regarding the tracking error. The visual feedback is conveyed through an on-screen circle that represents both the sign and magnitude of the error. In the tactile feedback conditions, the active stimulator is used to convey information about the sign and amplitude of the error (from **[204]**).

2.1.4 Data analysis and statistics

The experiment measured several outcomes to unravel the acquired data: (1) the sensation threshold (ST) in which the participant could feel the stimulation, (2) the success rate of recognizing the stimulation location, (3) the number of distinct intervals (NDI) defined by the magnitude of the just noticeable difference (JND), (4) the Weber fraction (WF) as the percentage difference needed between two stimuli to be classified as different, and (5) the tracking performance measured by delay, average rectified error, and correlation coefficient during the tracking task.

To calculate ST, the data from three trials for every one of the twelve locations in the arm-shoulder region were averaged for each subject, and then these values were averaged across the three arm-shoulder segments (lower arm, upper arm, and shoulder) and two sides of the region (ventral and dorsal). The calculation of JND was performed for each individual location as well as for arm-shoulder segments, considering both ventral and dorsal sides, and used to

calculate NDI iteratively using the equation: $I_{k+1} = I_{k'} + JND * I_k$, where I is the stimulation intensity and k counts the intervals. The NDI was set to k when I_{k+1} exceeded the maximum

intensity. The WF was calculated from the JND using the formula: $WF = \frac{JND}{b} * 100$, where b is the baseline intensity.

The trial tracking performance was assessed by comparing the generated and reference trajectories for each of the three arm-shoulder segments, and the shape similarity, average deviation, and time delay were compared. The mean values of these three parameters were calculated for each subject and arm-shoulder segment.

One-sample Kolmogorov-Smirnov tests showed that any of the outcome parameters were normally distributed. Therefore, a Friedman test combined with a post-hoc Wilcoxon signed-rank test were utilized to determine significant differences between different locations, segments, and sides of the arm-shoulder region. Additionally, a Kruskal-Wallis test in combination with a post-hoc Wilcoxon ranked-sum test were utilized to detect statistically significant differences between different populations. All statistical tests were corrected for multiple comparisons using the Bonferroni-Holm correction. The significance threshold was set to 0.05.

To investigate the variance between subjects and how it compares between segments and populations, Levene's tests were performed.

All results are presented as "median [interquartile range (IQR)]".

2.2 NEUROPATHOLOGICAL ANALYSIS OF NEUROMAS

2.2.1 Ethical approval

The present study was approved by the ethics committee at the University Medical Center Gttingen (Ethics Number: 20/11/17).

2.2.2 Human Tissue

The analyzed samples include nerves from upper and lower limb amputees suffering neuroma pain at their residual limb (Neuroma pain indicating surgery was defined and exhausted non-surgical treatments as improvement of prosthetic fitting, desensitization (and was objectified by clinical examination (reliable HT sign), pain relief after infiltration with local anesthesia, imaging (MRI and/or ultrasound). These nerves will be referred to as neuroma with neuroma pain. Furthermore, peripheral nerves were obtained from amputees which suffered Residual limb pain (RLP) due to scars, soft tissue problems, insufficient socket fitting, etc. , and intraoperatively, neuromas were found. Surgical treatment was TMR and/or burying the nerve [41, 154]. These nerves will be treated as neuroma without neuroma pain. The third group of nerves are nerves that were freshly transected and harvested during tumor surgery and are further seen as the control group. All surgical procedures were performed at the Department of Trauma Surgery, Orthopedics, and Plastic Surgery, and the samples were processed and stored in the Department of Neuropathology, both located at the University Medical Center in Göttingen (UMG) (Table 1).

Patient	Gender	Age (years)	Procedence	Pain	Neuroma	HT	VAS
1	m	32	Leg (right)	Yes	Yes	Yes	3
2	m	36	Leg (right)	Yes	No	Yes	10
3	m	33	Leg (both)	Yes	Yes	Yes	7
4	m	55	Arm (right)	No	No	No	0
5	m	61	Arm (right)	Yes	Yes	Yes	8
6	m	39	Sh. (left)	Yes	Yes	Yes	5
7	m	32	Hand (right)	Yes	Yes	Yes	3
8	m	38	Leg (left)	No	No	No	0
9	m	23	Arm (left)	Yes	Yes	Yes	3
10	m	46	Leg (left)	Yes	Yes	Yes	6
11	w	28	Leg left	Yes	Yes	Yes	9
12	m	77	Leg (left)	No	No	No	0
13	w	63	Arm (left)	No	No	No	0
14	w	49	Leg (right)	No	No	No	0
15	w	66	Leg (left)	No	No	No	0
16	m	25	Arm (right)	No	No	No	0
17	m	40	Arm (left)	No	Yes	No	0

Table 1 - Tissue samples. Demographics of the included patients. Greyed out samples were excluded due to difficulties in comparison like cutting angle or nerve growth. Patients with neuroma and pain underwent surgery due to named pain. Patients with neuroma but without pain underwent surgery due to secondary aspects, as prosthetic fitting. A neuroma was detected intrasurgically and removed. The control group are freshly cut nerves, without pain or neuroma. These were extracted during tumor surgery.

2.2.3 Sample preparation and tissue processing

2.2.3.1 Tissue collection and fixation

All samples were sent from the operation rooms in the UMG to the Neuropathology laboratory in a wet chamber devoid of fixatives. After the macroscopic inspection of the biopsies by a neuropathologist, the tissue samples destinated to paraffin embedding were placed in labeled embedding cassettes and fixated in a 3.7% formalin solution for 12-24 hours.

2.2.3.2 Embedding

Following the fixation step, the tissue was removed from the formaldehyde solution and soaked in running tap water for 2 hours. Subsequently, the tissue was further prepared using an Excelsior tissue processor. Here the tissue samples passed automatically through ascending alcohol series, isopropanol, and xylene for given exposure times. Finally, the samples passed through two or three paraffin baths. After approximately 18 hours, the samples were taken from the last paraffin bath of the embedding machine and immediately transferred to the paraffin bath of the pouring station. Here the tissue samples were individually removed from the embedding cassettes and poured using metal molds and the bottom of the embedding cassettes. The obtained paraffin blocks were stored in the block archive of the Department of Neuropathology, UMG.

2.2.3.3 Cutting and mounting of formalin-fixed paraffin-embedded tissue slices

Upon embedding and/or before cutting, the paraffin blocks were cooled on cooling plates and prepared for making 5-6 µm-thick paraffin sections. The paraffin sections were collected in a cold-water bath, individually mounted on microscope slides, and transferred to a warm water bath for a short time. Here they were allowed to fix on the slide by means of the heat and then collected in a staining rocker to dry. Sections of different cases were collected and dried at 80°C in a drying oven for 10 minutes. After drying, the sections were first deparaffinized in xylene and then led through a descending alcohol series to water to facilitate the staining process in aqueous solutions.

2.2.4 Histological and immunohistochemical stainings

Histological and immunohistochemical stainings were performed on slices of the above-mentioned peripheral nerves.

Nuclear structures were labeled using hematoxylin (H), and immunohistochemical stainings were performed using the following primary antibodies:

- Anti-CD3, which recognizes the CD3 cell surface glycoprotein that plays a crucial role in T-cell activation and signaling and serves as a reliable marker for T-lymphocytes [207], whose infiltration is associated with the development of neuropathic pain [208].
- KiM1P, a marker for macrophages and monocytes. Macrophages contribute significantly to neuroinflammatory responses following nerve injury and the development and maintenance of neuropathic pain [209].
- Anti-S100. S100 belongs to a family of calcium-binding proteins and is predominantly expressed in glial cells, including Schwann cells, which are responsible for myelination, peripheral nerve support [210] as well as peripheral nerve regeneration during neuroma formation [211].

Antibody	*Host*	*Dilution*	*Provider*	*Cat. Number*
CD3 (Paraff)	Rabbit	1:25	Dako	A0452
KiM1P	Mouse	1:50	Path. Kiel	
S100	Rabbit	1:400	Dako	Z0311

Table 2 - Antibodies

These primary antibodies were dissolved in 10% FCS/PBS and filled into a cover plate chamber with a volume of 120 µl. The tissue slices were then incubated for 90 minutes at room temperature. The primary antibody binding was visualized using a biotinylated secondary antibody followed by a developing step with avidin-peroxidase and diaminobenzidine (DAB).

In addition to the immunostainings, the Elastica van Gieson (EvG) histological staining [212] was performed to provide an overview of the tissue architecture and composition and in particular, to detect the different fiber types present in the connective tissue. The final staining mix is composed of two primary solutions: Verhoeff's hematoxylin and Van Gieson's stain. Verhoeff's hematoxylin stains elastic fibers black or dark blue, while Van Gieson's stain, which is a mixture of picric acid and acid fuchsin, stains collagen fibers red and cell nuclei dark blue or black.

2.2.5 Digitization of histological sections

Whole-slide bright field scans of the stained tissue slices were acquired at 20x-magnification using an Olympus VS120 slide scanner for subsequent digital analysis.

2.2.6 Analysis of histological images and methodological development

When multiple specific structures need to be highlighted in brightfield microscopy, a combination of stains with different spectral absorption characteristics is used. However, the individual contrast information of each stain gets diluted due to the multiplication of their distinct spectral transmission. Therefore, it is crucial to reconstruct the contrast information of each stain to obtain its diagnostic benefits.

Color deconvolution using a set of stain vectors to calculate the stain concentrations in every pixel of the image was applied on the hematoxylin/DAB stainings. These vectors represent the optical properties of each stain, such as its absorbance spectrum and the wavelength-dependent contribution to the overall color of the image [213].

Furthermore, a method able to differentiate between organized and unorganized nervous tissue was developed.

Therefore, several algorithms were designed for the different automatized image analyses in Python, combining existing libraries such as SciPy and OpenCV [214, 108], as well as self-written functions. The analysis can be broadly differentiated into two methodologies:

1. A combination of machine learning approaches, together with computer vision, was used for tissue segmentation and morphological analyses of EvG staining.
2. A combination of color deconvolution and, again, computer vision was designed for positive staining detection in S100, KiM1P, and CD3 stainings.

All analyses were performed on a Razer Blade 15 Laptop with an Intel Core i7-10750H Processor working at 2.60GHz, 15.86GB RAM, and an NVIDIA GeForce RTX 2070 graphics card with Max-Q design.

2.2.6.1 Tissue segmentation

Using unsupervised classification, which requires less computational power compared to supervised classification, the existing dataset underwent an initial evaluation using K-Means clustering. This vector quantization approach aims to separate n data points into k unique clusters. By assigning each data point to the nearest cluster mean, which serves as the cluster's representative, the data space is effectively divided into Voronoi cells (Figure 11).

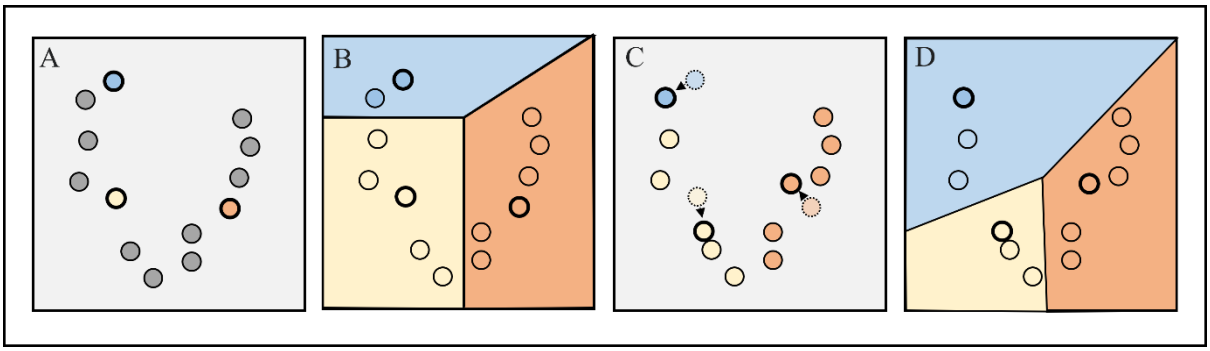

Figure 11 - KMeans clustering. (A) Step 1: k initial centroids (k=3 in this case) are randomly chosen within the data domain (indicated by distinct colors). **(B)** Step 2: k clusters are formed by associating each data point with the nearest centroid. The partitions displayed represent the Voronoi diagram generated by the centroids. **(C)** Step 3: The geometric center of each of the k clusters is determined, becoming the new centroid. **(D)** Step 4: Steps 2 and 3 are iteratively repeated until a convergence criterion is satisfied.

However, after initial evaluation, a Random Forest Classifier from scikit-learn was used as the model, with a pixel-based segmentation being computed using local features based on local intensity, edges, and textures. As an ensemble learning algorithm, it is based on the concept of training several models using distinct data subsets and integrating their predictions to enhance the overall accuracy of the resulting model (Figure 12). During classification, the RF develops branches that decrease classification error using a measure similar to entropy while trying to minimize it at each branch. A metric commonly used is the Gini index $G = \sum_{k=1}^{K} \hat{p}_{mk}(1 - \hat{p}_{mk})$, where $\hat{p}_{mk}$ denotes the proportion of observations in the m-th region belonging to the k-th class, essentially functioning as a measure of variance.

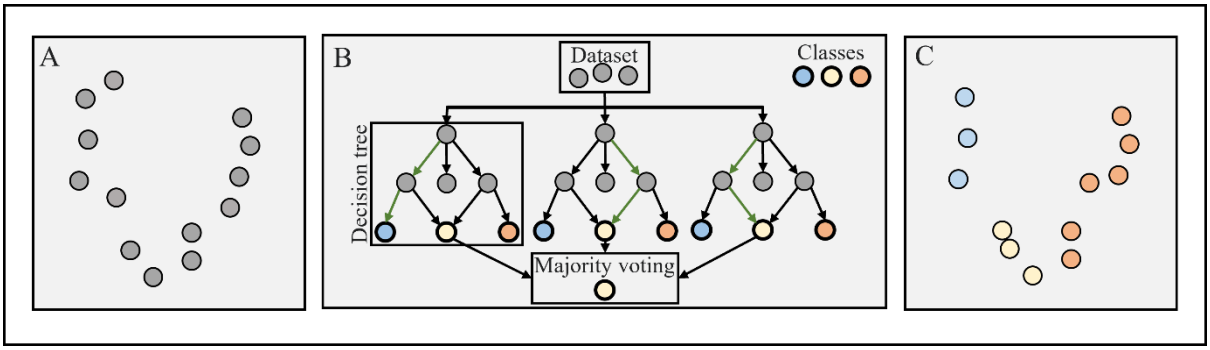

Figure 12 - Random Forest Classifier. (A) Unclassified data. **(B)** A subset of datapoints is passed to the decision trees. Each decision tree produces a result. Using majority voting, a final output is defined. To avoid overfitting, not all features are included in the decision trees. **(C)** The same procedure is performed with all pixels in the image.

This algorithm was implemented into a workflow to segment images directly from the server into defined labels. In the first step, several regions of interest (ROI) were selected in every image, in which differentiation was made by commenting between tissues to segment. Additionally, regions to be excluded were selected, as some samples included tissues that did not belong to the nerve itself and remained on the sample from the staining procedure. Using

the Open Microscopy Environment (OME) Remote Objects (OMERO) library, the algorithm automatically communicates locally with the OMERO server to retrieve every image and its associated ROIs. Using a predefined python dictionary, it transforms the combination of ROIs into a 2-dimensional mask, in which each pixel was either 0 (unlabeled), or a number between 1 and n (respectively for every tissue) (Figure 13).

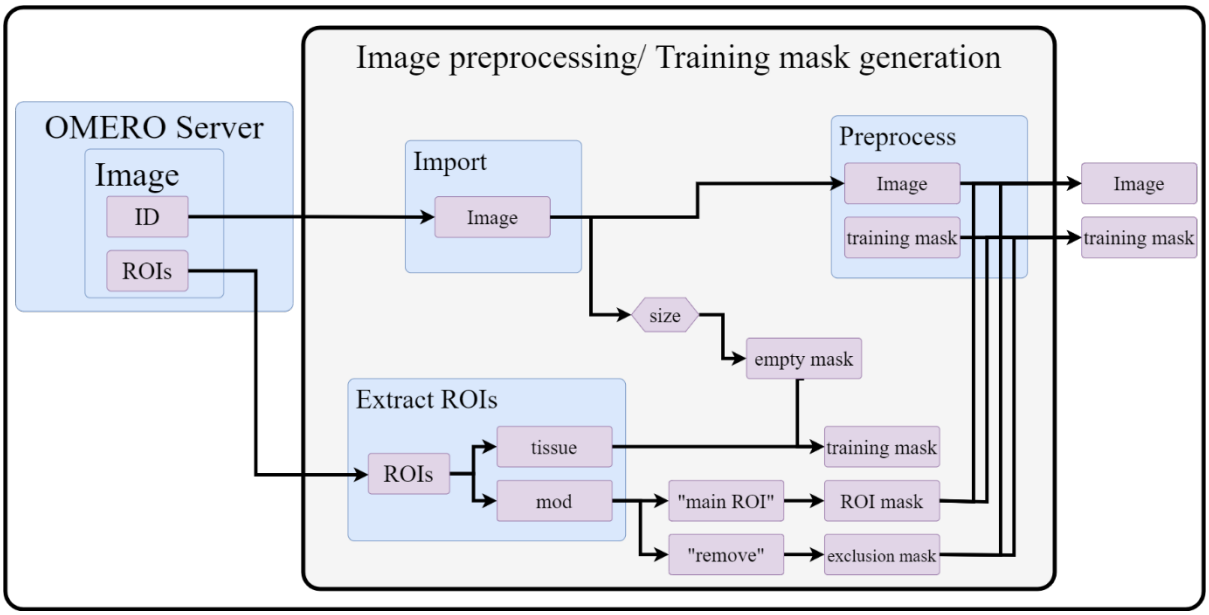

Figure 13 - Image import and preprocessing. Workflow for the import of images from OMERO, their preprocessing and the generation of training masks. ROIs predefined in OMERO are imported together with the images. These are used to generate the mask and to remove the regions without interest from the image.

The algorithm then uses the feature module from Scikit-image [215] to extract local features from the imported and resized image at multiple scales. It computes them by taking an image as input and calculating the features using a Gaussian pyramid approach. In this approach, the input image is repeatedly blurred and subsampled to generate a sequence of images, from which two main features are extracted by averaging over the scales. On the one hand, the pixel intensities, on the other hand, the eigenvalues of the Hessian matrix, providing information about the local structure and orientation of image features, such as edges, corners, and blobs. The resulting feature matrix contains the basic features for each pixel at each scale and is used together with the mask to generate training and testing data, by randomly splitting the dataset into two subsets ($\frac{2}{3}$ for training and $\frac{1}{3}$ for testing). Then, the training data is used to train the random-forest classifier (for computational reasons, the images and ROI-masks were split into four equal pieces, trained separated, and stitched together afterward). In the next step, the classifier then predicts the unlabeled pixels and outputs a n-dimensional matrix containing a 1-dimensional mask in every dimension (again, respectively for every tissue) (Figure 14).

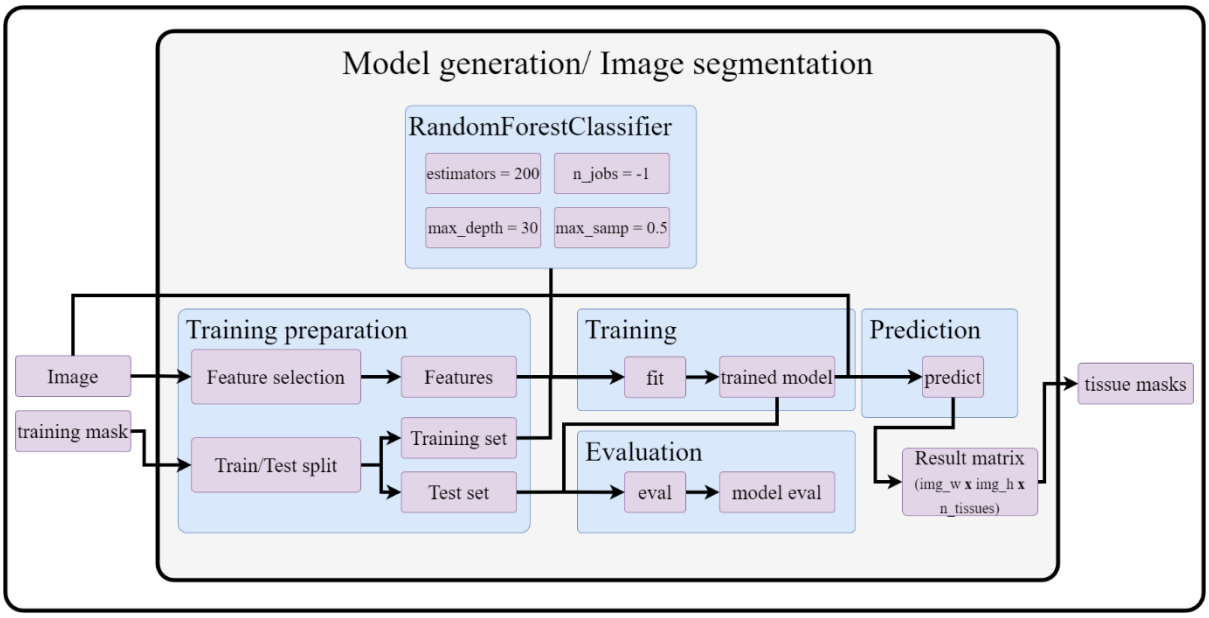

Figure 14 - Training and segmentation. Depiction of the workflow using the image and mask to train a model able to segment the image by predicting unlabeled pixels based on the features extracted from the image. This workflow outputs a matrix made of a stack of one-dimensional masks, one for every tissue.

2.2.6.2 Morphological analysis using EvG-staining

The increased contrast achieved with EvG-staining was used to differentiate between organized and unorganized nervous tissue using tissue segmentation as depicted in 2.2.6.1. Therefore, the resulting tissue mask for this staining consisted of a 6-dimensional matrix, where every layer consisted of a mask of either background, organized nervous tissue, unorganized nervous tissue, connective tissue, fat tissue, or erythrocytes. Most of the masks were kept as they were; however, the mask containing organized nervous tissue was further filtered in an additional step, as the algorithm sometimes misinterpreted forming neuroma for an organized nervous tissue. Here, the algorithm uses the inherited roundness of healthy fascicles in its favor. Using a Laplacian transform, it defines the masks' borders. Dilatating these borders and subtracting them from the actual mask allows separation of single fascicles from each other. Then, the greatest circle fitting in each fascicle and the smallest circle fitting the whole fascicle are calculated. It was then defined that the radial ratio between both circles had to be less than 0.2, to define it as "round enough". The pixels not reaching this goal were deleted and not further considered. Additionally, a mask for the connective tissue intruding neuroma was generated by creating a new mask surrounding the interconnected neuroma by performing a convex hull surrounding the neuroma tissue. To identify connective tissue in this area, adding to it the connective tissue previously wrongly identified as nervous tissue during segmentation, a threshold was applied targeting its specific staining color, and the result was added to the

original connective tissue mask. It additionally results in a mask containing only the connective tissue located in the surroundings of unorganized fascicles (Figure 15).

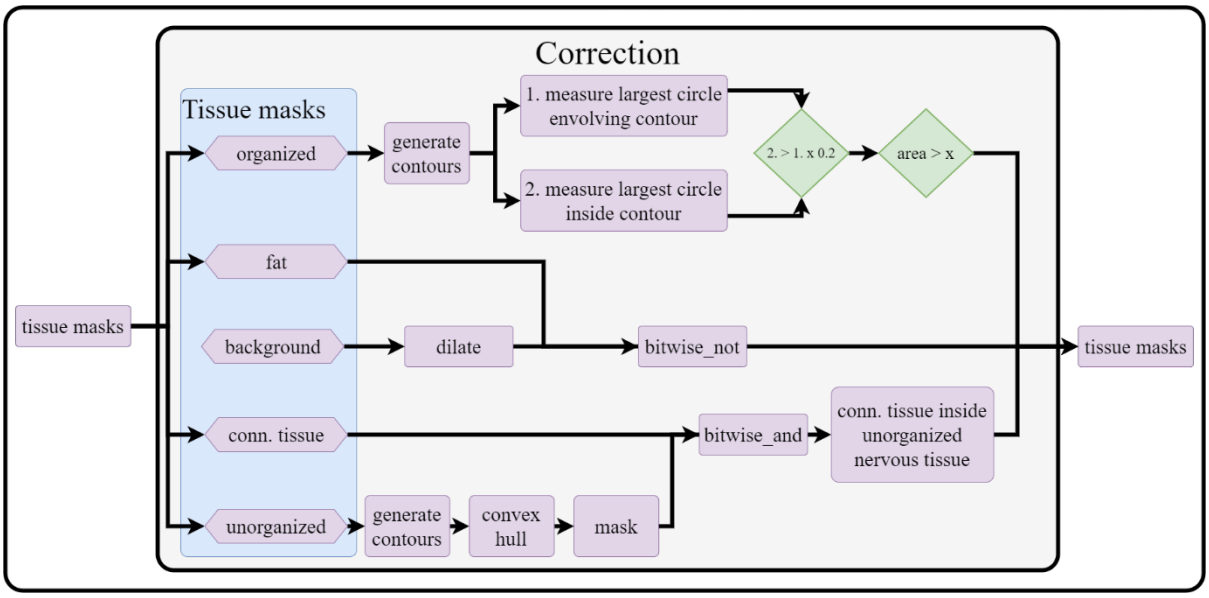

Figure 15 - Tissue correction. Workflow showing the correction of the masks after segmentation.

The masks are then used to define the percentage of each tissue in relation to the whole nerve, the "normalized deviation" between organized and unorganized nervous tissue, as well as the amount of connective tissue inside the neuromas.

Using the percentual amount of white pixels in relation to the black ones in the mentioned masks, the relative amount of healthy fascicles (organized nervous tissue), neuroma (unorganized nervous tissue), connective tissue, fat tissue, and erythrocytes were calculated.

The calculated percentages were then applied to the actual area of each transection, allowing to compare the relative quantity of every tissue together with its absolute amount. This was performed by first defining the nerve's area using the total area of the image obtained and multiplying it by the known percentage of tissue in the image. Afterward, each of the obtained relative amounts was multiplied by the total area.

Furthermore, the ratio between the amount of organized and unorganized fascicles was calculated using the following formula $\frac{unorganized-organized}{\max(unorganized,organized)}$. This results in a value between -1 and 1, from which 1 means that only unorganized nervous tissue is present and -1, that only organized nervous tissue is present (which is only true for the control group).

The resulting values were used to correlate relative and absolute amounts with the pain level reported by patients with neuroma.

Kolmogorov-Smirnov tests of normality were employed to verify that the data does not differ significantly from a normal distribution. To compare the relative amounts of tissue between the groups, t-tests for independent samples between both populations were employed. As in the case of the relative and absolute amounts of unorganized fascicles in controls, the results cannot possibly be normally distributed. Thus Mann-Whitney U tests were performed on these cases.

As the number of samples is small, Spearman correlation coefficients were calculated with associated p-values between the different tissue percentages and normalized deviations and pain levels reported by the patients (VAS).

All results are presented as “median [interquartile range (IQR)]”.

2.2.6.3 T-Lymphocyte-, macrophage-, and Schwann-cell-quantification

Quantifying T-lymphocytes, macrophages, and Schwann-cells, as the analyzed cells require the image to be in its full size, they were processed in chunks of 1000x1000 pixels, to reduce computational costs and time. Additionally, due to the less differentiable staining, the images where solely segmented into nervous tissue and background (as depicted in 2.2.6.1), using solely one model for all images of a single staining. Chunks were then only processed, if the segmented chunk contained peripheral nerve, further reducing computation.

For every staining, the first step was to deconvolute the staining channels to separate and individually analyze the hematoxylin (nuclei) and DAB (protein of interest) (Figure 16) using Scikit-learn [213].

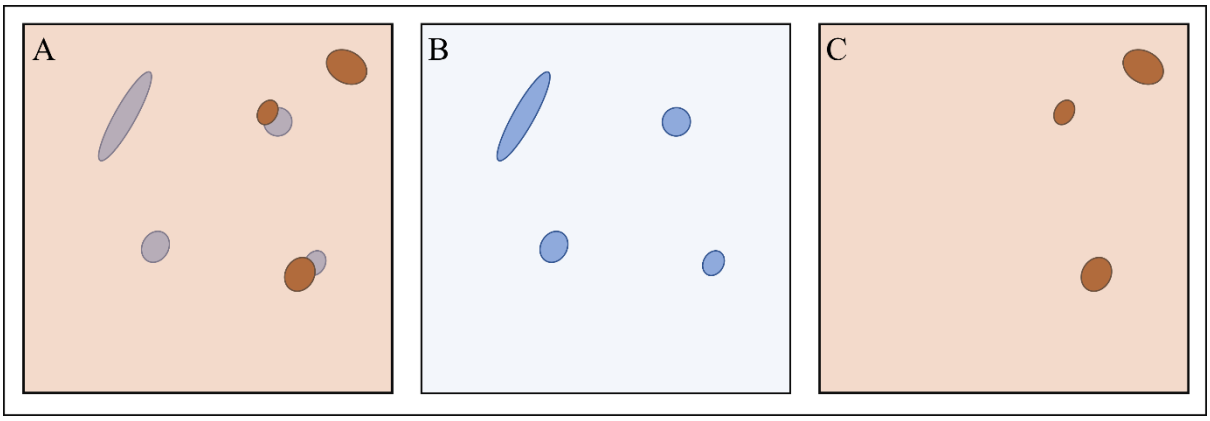

Figure 16 - Color deconvolution. The original image **(A)** is separated into the different stains: Hematoxylin **(B)** and DAB **(C)**.

The relevant signals were then detected by converting the hematoxylin and DAB channels to gray images and applying mean adaptive threshold to them. The main idea behind adaptive thresholding is to calculate a unique threshold value for each pixel, considering the pixel values within its surrounding neighborhood. This allows the algorithm to adapt to local changes in illumination and contrast, leading to more accurate and robust segmentation of foreground and background regions. In mean adaptive thresholding, for each pixel, the threshold value is determined by calculating the mean pixel value within its neighborhood and then subtracting a constant value. This method is sensitive to local changes in illumination and can produce better results when the background has a relatively uniform intensity (Figure 17).

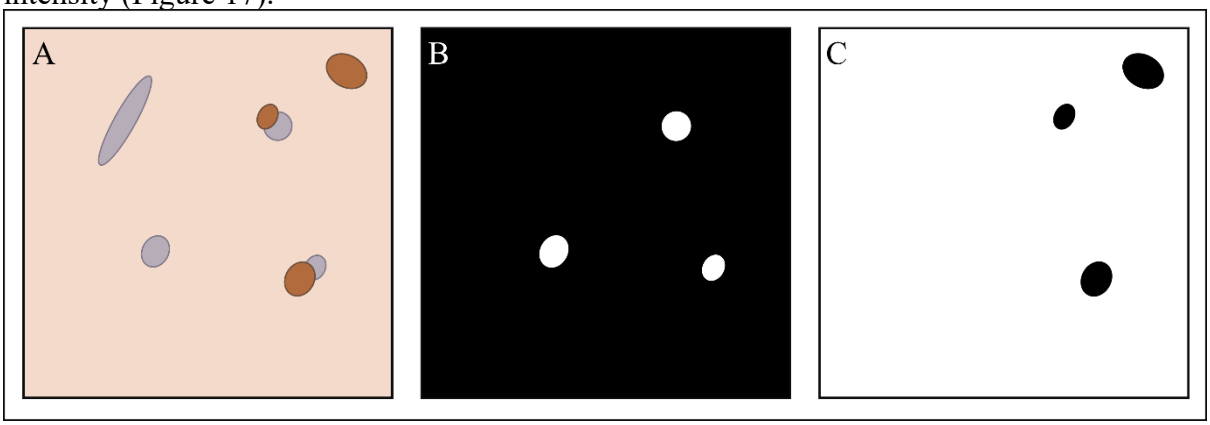

Figure 17 - Nuclei mask. Using the detected nuclei, a mask is generated **(B)**, which is then applied to the DAB-positive tissue mask, which contains the positive stainings after thresholding the DAB channel **(C).**

Depending on the analyzed staining, the thresholding and following cell counting might vary slightly. As T-lymphocytes are relatively round, nuclei were excluded if they surpassed a specific aspect ratio. For this, the smallest enclosing circle and largest circle inside the nuclei were calculated for every nucleus. Additionally, the smallest enclosing rectangle was

calculated and, using the width and height of the rectangle, the aspect ratio was calculated. If the inner radius was larger than the outer radius x 0.1 and the aspect ratio was between 0.8 and 1.2, the nucleus was seen as valid. Additionally, all nuclei beyond a specific size (between 20px and 250px) are also excluded. As positive CD3 staining is typically seen around the nuclei, a mask is generated using detected nuclei in the hematoxylin channel. Each positive pixel accumulation on that mask is enlarged and applied to the DAB channel. The masked channel is then used to detect CD3-positive cells. A similar approach is performed for KiM1P; yet, the ratio-filtering was not applied (Figure 18).

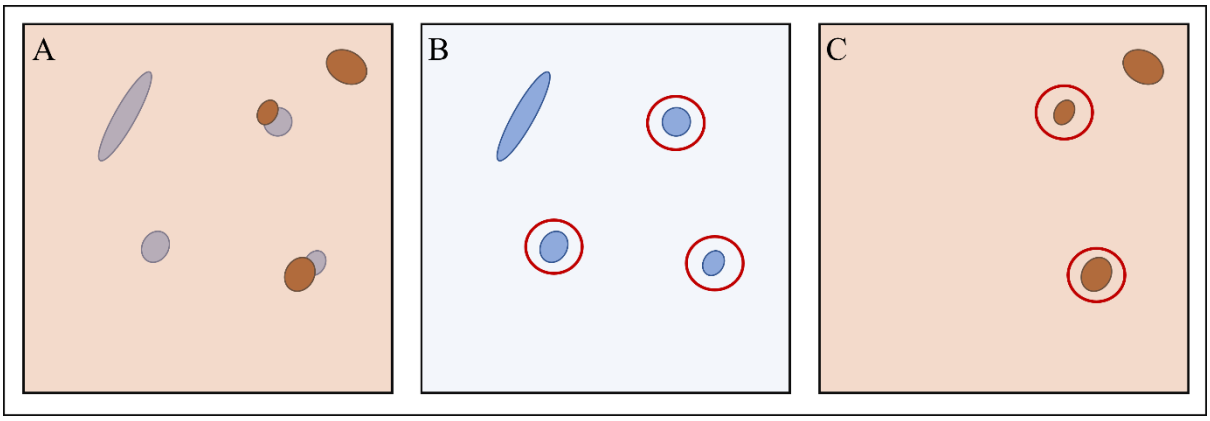

Figure 18 - Positive cell detection. After applying the mask, the number of nuclei (after filtering) **(B)** and DAB-positive cells **(C)** is counted.

However, regarding S100, the masking step is not usable as such, as the S100-positive areas might not be at a certain distance around nuclei. In this case, a distinct approach was performed, with the introduction of a strict methodology determining which positive cells to count and which not to count. The nuclei and S100-positive cells were detected, and they were labeled to make them identifiable. Subsequently, all S100-positive staining that did not contain at least one nucleus inside was excluded. Since the Schwann cell's nucleus might not be on the current slice plane, correctly labeled S100-positive cells are being excluded; however, false positives are ensured not to be included.

As ratios between populations are being compared, and the named limitation is equally applied to all samples, statistical errors are not introduced. The obtained results were the number, as well as area covered by nuclei, macrophages, T-lymphocytes, and Schwann-cells. The number of cells per unit area of nervous tissue was calculated by dividing the total number of positive cells by the area of the nervous tissue ($\frac{number\ of\ cells}{area\ of\ nervous\ tissue}$). To facilitate comparison and interpretation, we normalized this value to a range between 0 and 1, with 0 representing no

positive cells and 1 indicating the maximum possible density of positive cells in the tissue. The same was applied for the area ($norm\left(\frac{area\ of\ cells}{area\ of\ nervous\ tissue}\right)$).

These values were used to compare the number of macrophages and T-lymphocytes in relation to the total area of nervous tissue, as well as the area covered by Schwann cells in relation to the total are between controls and neuroma patients, further distinguishing between neuroma patients with and without neuroma pain. Additionally, as it is not known if the positive cells are on organized or unorganized nervous tissue, a positivity factor was calculated, using the previously computed normalized deviation between organized and unorganized tissue. For this, the number of positive cells was divided by the aforementioned normalized deviation:

$$\frac{unorganized - organized}{\max(unorganized, organized)} * norm\left(\frac{number/area\ of\ cells}{area\ of\ nervous\ tissue}\right)$$

These results were further correlated with the pain level reported by patients with neuroma.

Kolmogorov-Smirnov tests of normality were employed to verify that the data does not differ significantly from a normal distribution. To compare the relative amounts of tissue between the groups, t-tests for independent samples between both populations were employed. As in the case of the relative and absolute amounts of unorganized fascicles in controls, the results cannot possibly be normally distributed. Thus Mann-Whitney U tests were performed on these cases.

As the number of samples is small, Spearman correlation coefficients were calculated with associated p-values between the different tissue percentages and normalized deviations and pain levels reported by the patients (VAS).

All results are presented as “median [interquartile range (IQR)]”.

2.2.6.4 Model validation

Next to the visual validation of the segmented images, Random Forest algorithms supply several methods for additional model validation. As stated, during the training, not all training data is used, as $\frac{1}{3}$ of it is kept out of the fitting to be predicted afterward. Here, the model is applied to the remaining pixels, and it uses the labeled mask to compare the prediction results with the actual labels.

Moreover, an overall report is generated that provides further information on the performance. It includes metrics such as accuracy, precision, recall, and F1-score.

The accuracy of the classifier is the proportion of correctly classified instances in the data set. Precision quantifies the ratio of true positive outcomes to the total number of predicted positive cases, while recall calculates the ratio of true positive outcomes to the overall count of genuine positive instances. Lastly, the F1-score is calculated using the weighted average of precision and recall, which considers both metrics simultaneously to provide a balanced assessment of a model's performance.

As a further method of testing the model’s stability, k-fold cross-validation was performed. K-fold cross-validation is a widely used technique for assessing a model's performance in machine learning and statistical modeling. It helps to address the overfitting issue, as it provides a more robust estimate of the model's generalization ability when applied to unseen data [216].

During k-fold cross-validation, the dataset is divided into k equally sized subsets or "folds". The model is then trained and evaluated k times. In each iteration, one of the folds is used as the validation set, while the remaining k-1 folds are used for training. The process is repeated until every fold has been used as a validation set once [216].

By averaging the performance metrics (e.g., accuracy, precision, recall, F1-score) obtained from each fold, a more reliable estimate of the model's performance is obtained, mitigating the risk of overfitting, reducing the dependence on any single partitioning of the data [216].

Further, an extra step was performed, in with a model trained on an image containing unorganized nervous tissue was used to segment a control image.

Lastly, the reduction of the images was compared to using the full image size, to test if the methodology removing detail will affect the result.

3.1 PSYCHOPHYSICAL CHANGES AFTER PNI

To fully map the tactile sensations in response to vibrotactile stimulation across the whole arm-shoulder region (namely the lower arm (*LA*), upper arm (*UA*), and shoulder (*SH*), as well as the dorsal (*dors*) and ventral (*vent*) sides) of ten able-bodied (*AB*), six plexus brachialis (*BPI*), and five transradial amputated (*TR*) participants, three psychometric evaluations were performed.

For simplicity, the baseline obtained from the comparisons of the outcome and variance between segments (LA, UA, and SH) and sides (*dors*, *vent*) from able-bodied participants is presented first. Afterward, the results for both patient populations are assessed and put in comparison to the baseline.

To facilitate readability, all results are supplied in several tables as supplementary material and only the p-values of significant results are named.

3.1.1 Sensation capacity on the healthy arm

3.1.1.1 The Sensation Threshold is location dependent.

Comparing the sensation threshold (ST) between the different regions of the arm and shoulder on *AB*, a significantly higher threshold on the shoulder than on the lower arm was found ($p = 0.004$). No differences between *LA* and *UA* or between *UA* and *SH* were found. In terms of variance, no significant differences between either of the segments was detected. In addition, the *ST* on the *dorsal* side was discovered to be significantly higher than on the *ventral* side ($p = 0.008$), displaying a similar variance (Figure 19).

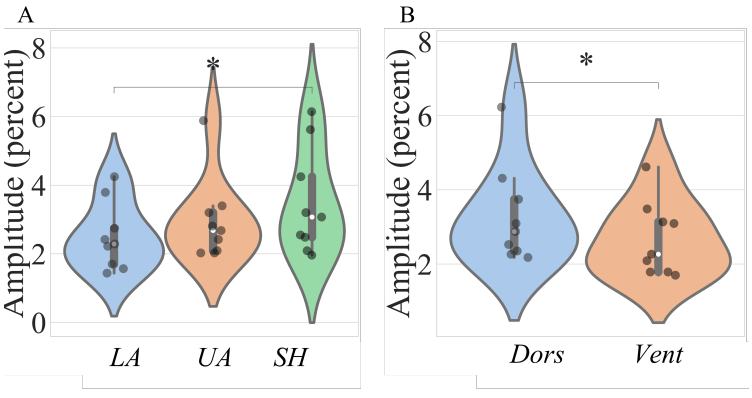

Figure 19 - Sensation threshold. along the arm and shoulder region (in percent of the maximum stimulation amplitude) of healthy participants comparing the **(A)** single segments and **(B)** dorsal and ventral sides between each other. Each violin plot represents the density of data points at different values. The white dot marks the median, and the black box represents the interquartile range (IQR). The sensation threshold data were collected from ten able-bodied, six brachial plexus injured, and five transradial amputated subjects. Dots indicate individual results (n_able=10). Asterisks (*) denote the statistical difference in value ($p<0.05$).

3.1.1.2 The outcomes of the just noticeable difference are location-independent.

In the second task, the participant had to discriminate between two consecutive stimuli and select the one with a higher amplitude. Reliable differences above 20%±7% were detected between baseline and test stimuli across all arm-shoulder regions. Regarding the Weber fraction (*WF*) of vibration stimulation on the arm-shoulder region of able-bodied participants, any significant difference between any of the segments, nor regarding the actual *WF*-value, nor in terms of intra-segmental *WF*-variance were identified. Similar results were obtained comparing *dorsal* and *ventral* and no significant differences were detected (Figure 20A/B).

The number of discrete steps that could be discriminated using the obtained tactile sensation range (11±3) also did not show any significant difference between the arm-shoulder segments, either regarding the number of distinct intervals (*NDI*) or the *NDI*-variance. The same applies to *dorsal* and *ventral* (Figure 20C/D).

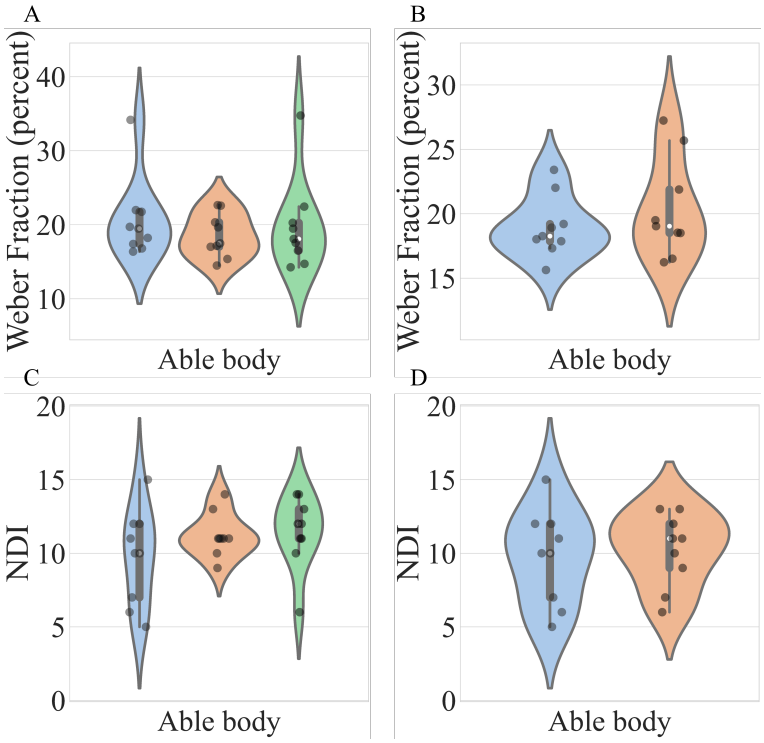

Figure 20 - Weber fraction (A/B). (in percent of the maximum stimulation amplitude) and **Number of distinct intervals (C/D)** along the arm and shoulder region of healthy participants comparing the **(A/C)** single segments and **(B/D)** dorsal and ventral sides between each other. Each violin plot represents the density of data points at different values. The white dot marks the median, and the black box represents the interquartile range (IQR). The sensation threshold data were collected from ten able-bodied, six brachial plexus injured, and five transradial amputated subjects. Dots indicate individual results ($\mathbf{n_{able} = 10}$).

3.1.1.3 Only the error shows differences during the compensatory tracking task

During the compensatory tracking task, the participant acted as the controller in a closed-loop system, where they compensated for the error between a generated and a reference signal using a joystick as an input interface. Participants received either visual or tactile feedback about their performance. To ensure that the subjects understood and adequately performed the task, we used the session in which the subject performed the task with visual feedback on the monitor as a baseline with optimal feedback. Subjects in this condition demonstrated significantly better performance in all aspects.

In the tactile feedback condition, there were no significant differences in either delay or correlation coefficient between any of the segments. The delay consistently remained below 48.5ms [11.65ms], and the correlation coefficient was within the range of 64.4% – 72.2% [13.6%] for all three evaluated segments. The only significant difference detected was between the shoulder and upper arm, where the average rectified error was significantly higher in the latter case (0.33 [0.06] vs. 0.28 [0.08], p = 0.0039) (Figure 21).

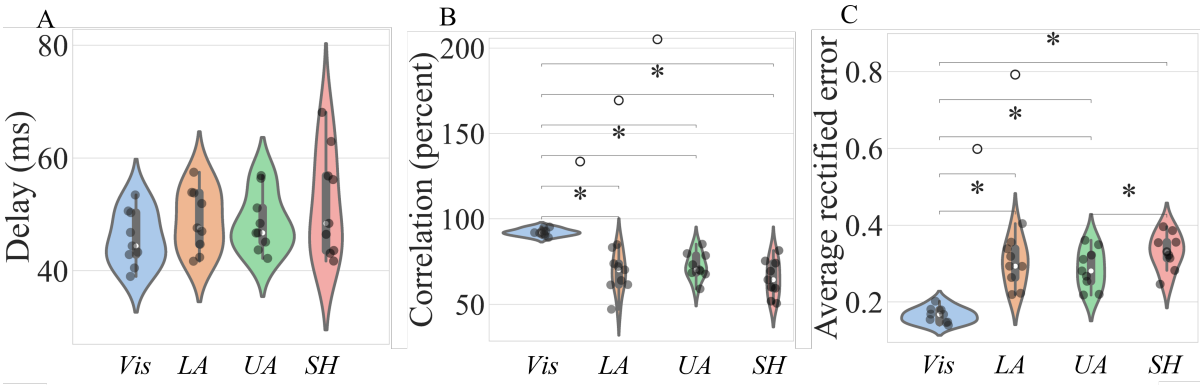

Figure 21 – Compensatory tracking task. (A) Delay (in ms), **(B)** correlation (in percent), and **(C)** average rectified error between target and cursor during the compensatory tracking task along the arm and shoulder region of healthy participants. Each violin plot represents the density of data points at different values. The white dot marks the median, and the black box represents the interquartile range (IQR). Dots indicate individual results ($\mathbf{n_{able} = 10}$). Asterisks (*) and circles (°) denote the statistical difference in value and variance respectively ($p < 0.05$).

3.1.2 Sensation capacity after peripheral nerve injury

3.1.2.1 Sensation threshold continuously decreases distally from the injury site.

Concerning the *BPI,* only significant differences between the *LA* and *UA* (p = 0.031) were found. No significant differences between *LA* and *SH* nor between *UA* and *SH* were found. The variance between single patients was, however, significantly lower regarding the *SH* than both the *LA* and *UA* (p = 0.002 and p = 0.009, respectively). No significant difference between *LA* and *UA* was found. Between *dorsal* and *ventral*, neither differences in threshold nor variance were found.

In the case of *TR,* neither significant differences in the ST-value nor the variance in the *ST* between any segment were found. The same applies between the *dorsal* and *ventral* ().

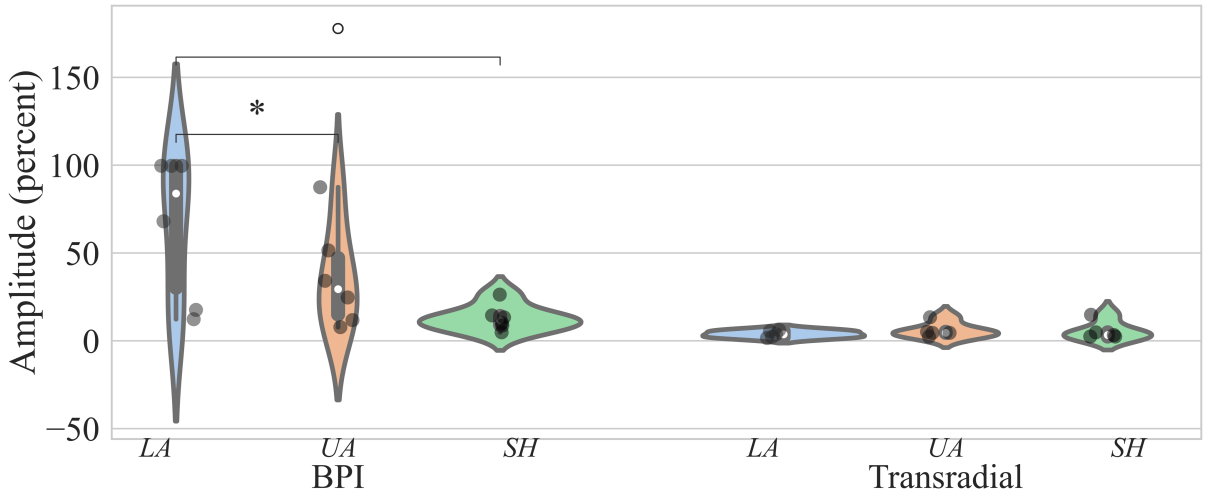

Figure 22 - Sensation threshold. Sensation thresholds along the arm and shoulder region (in percent of the maximum stimulation amplitude) of BPIs and transradial amputees, comparing the single segments of the arm between each other. Each violin plot represents the density of data points at different values. The white dot marks the median, and the black box represents the interquartile range (IQR). Dots indicate individual results ($\mathbf{n_{BPI}}$= 6, $\mathbf{n_{TR}}$ **= 5**). Asterisks (*) and circles (°) denote the statistical difference in value and variance respectively (p<0.05).

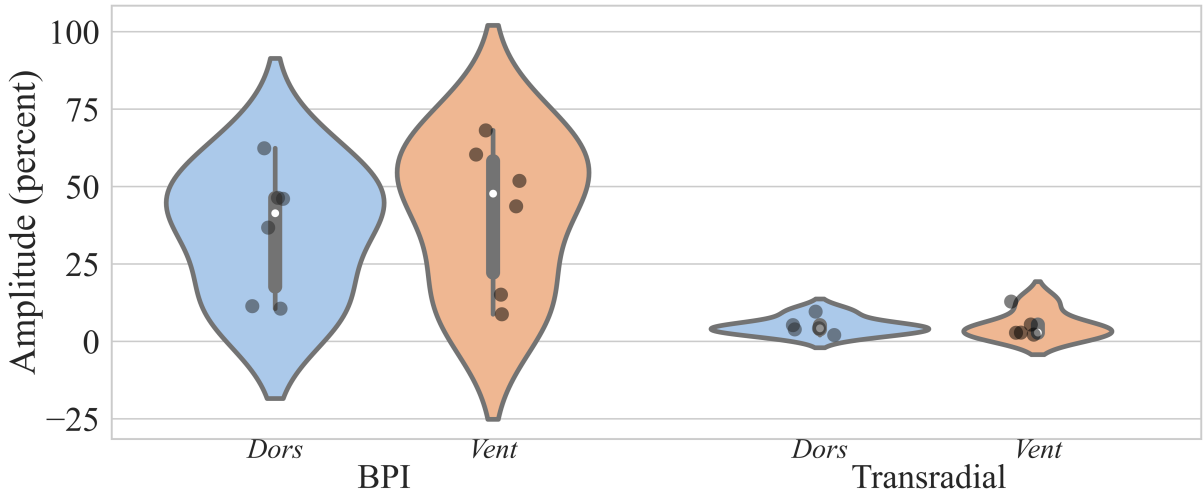

Figure 23 - Sensation threshold. Sensation thresholds along the arm and shoulder region (in percent of the maximum stimulation amplitude) of BPIs and transradial amputees, comparing dorsal and ventral sides between each other. Each violin plot represents the density of data points at different values. The white dot marks the median, and the black box represents the interquartile range (IQR). Dots indicate individual results ($\mathbf{n_{BPI}}$= 6, $\mathbf{n_{TR}}$ **= 5**).

3.1.2.2 TRs display no differences compared to the healthy arm.

Comparing the sensation threshold between populations, no statistical differences in *ST* between *AB* and *TR* in any of the segments were found. In contrast, *BPI* showed significantly higher *ST* than the *AB* in all regions (p = 0.0004 on the *LA* and *UA*, and p = 0.0016 on the *SH)*. They also exhibited a higher *ST* than the *TR* on the *LA* and the *UA* (p = 0.0043 on the *LA* and p = 0.0173 on the *UA*). No significant differences were found between the *SH* of *BPI* and *TR* regarding the segments.

Additionally, it was detected that *AB* show significantly lower *ST*-variance between subjects than *BPI* in every segment (p = 3.2e-11, p = 2.1e-09, and p = 0.0004 respectively for *LA*, *UA*, and *SH*). Moreover, significant differences were located between *AB* and *TR* on the *UA* and *SH* (p = 0.005 and p = 0.005) and between *BPI* and *TR* on the *LA* and *UA* (p = 3.54e-05 and p = 0.002) (Figure 24).

Regarding *dorsal* and *ventral*, it was discovered that both *AB* (p = 0.0014 and p = 0.0014 respectively for *dorsal* and *ventral*) and *TR* (p = 0.006 and 0.01 respectively for *dorsal* and *ventral*) exhibited significantly lower *ST* than *BPI*. Similarly, regarding the *ST*-variance between participants (p = 0.003 and p = 0.002 regarding *AB*, respectively, for *dorsal* and *ventral*; p = 0.04 regarding *TR*, for both *dorsal* and *ventral*) (Figure 25).

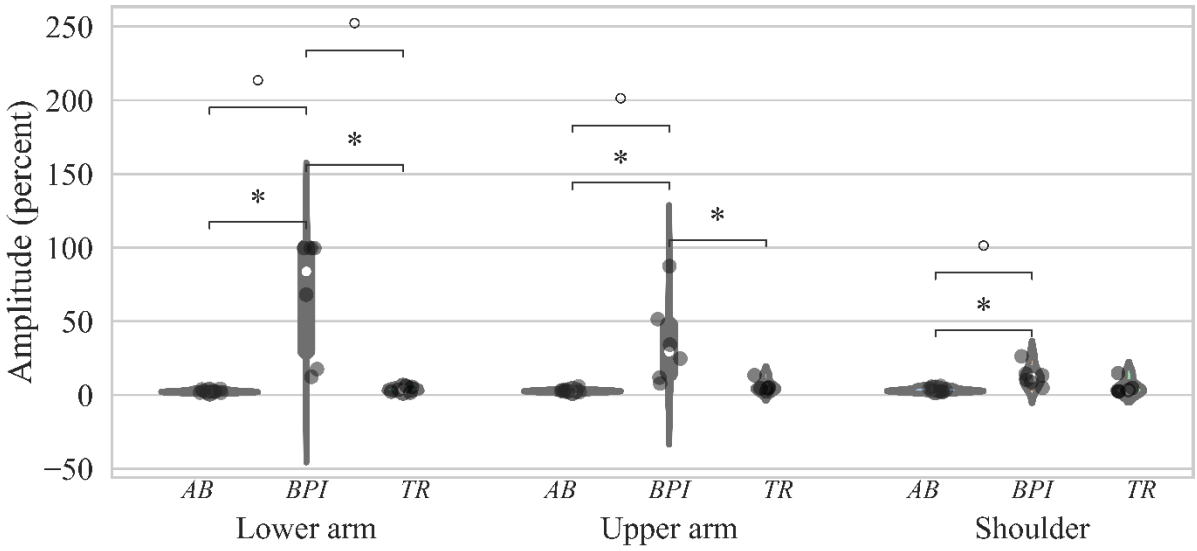

Figure 24 - Sensation threshold. Sensation thresholds along the arm and shoulder region (in percent of the maximum stimulation amplitude) of healthy participants, BPIs and transradial amputees, comparing the single segments of the arm between populations. Each violin plot represents the density of data points at different values. The white dot marks the median, and the black box represents the interquartile range (IQR). The sensation threshold data were collected from ten able-bodied, six brachial plexus injured, and five transradial amputees. Dots indicate individual results ($\mathbf{n_{BPI}}$= 6, $\mathbf{n_{TR}}$ **= 5**). Asterisks (*) and circles (°) denote the statistical difference in value and variance respectively (p<0.05).

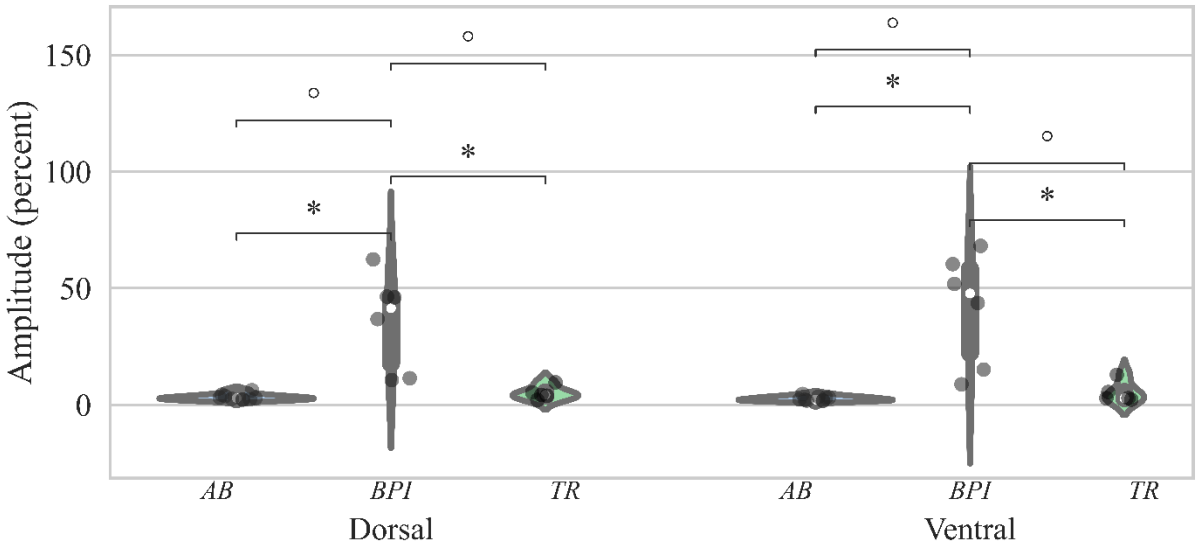

Figure 25 - Sensation threshold. Sensation thresholds along the arm and shoulder region (in percent of the maximum stimulation amplitude) of healthy participants, BPIs and transradial amputees, comparing dorsal and ventral sides between populations. Each violin plot represents the density of data points at different values. The white dot marks the median, and the black box represents the interquartile range (IQR). The sensation threshold data were collected from ten able-bodied, six brachial plexus injured, and five transradial amputees. Dots indicate individual results ($\mathbf{n_{BPI}}$= 6, $\mathbf{n_{TR}}$ **= 5**). Asterisks (*) and circles (°) denote the statistical difference in value and variance respectively (p<0.05).

3.1.2.3 Weber fraction and number of distinct intervals drastically worsen distally from the site of injury.

Only one of the *BPI* was able to identify differences in the measured range on the *LA*, leading to a *WF* of 100%, which is significantly higher than the results on the *UA* and *SH* (p = 0.03 and

p = 0.03, respectively). Also, *UA* and *SH* are significantly different (p = 0.03). In terms of *WF*-variance, no significant difference between any segments of *BPI* were found (Figure 26).

Likewise, no significant difference between *dorsal* and *ventral* neither regarding *WF* nor the *WF*-variance between *BPI* participants were detected (Figure 27).

Also, no significant differences between the *WF* or the *WF*-variance were identified between any of the segments nor *dorsal* or *ventral* in *TR* subjects (Figure 26/ Figure 27).

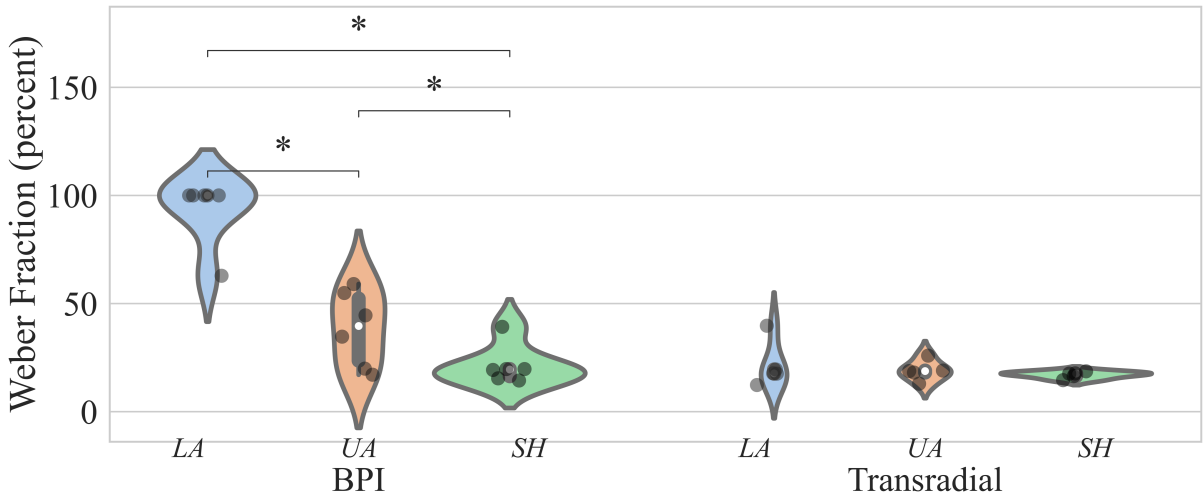

Figure 26 - Weber fraction. (in percent of the maximum stimulation amplitude) of BPIs and transradial amputees, comparing the single segments between each other. Each violin plot represents the density of data points at different values. The white dot marks the median, and the black box represents the interquartile range (IQR). Dots indicate individual results ($\mathbf{n_{BPI}}$= 6, $\mathbf{n_{TR}}$ = **5**). Asterisks (*) denote the statistical difference in value (p<0.05).

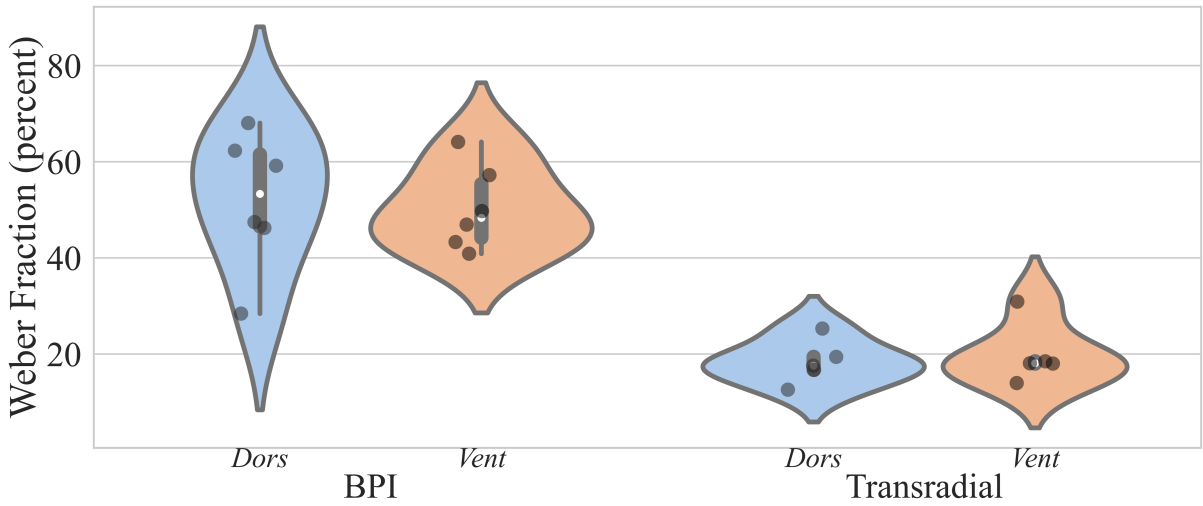

Figure 27 - Weber fraction (in percent of the maximum stimulation amplitude) of BPIs and transradial amputees, comparing dorsal and ventral sites between each other. Each violin plot represents the density of data points at different values. The white dot marks the median, and the black box represents the interquartile range (IQR). Diamonds indicate statistical outliers within a single boxplot and dots indicate individual results ($\mathbf{n_{BPI}}$= 6, $\mathbf{n_{TR}}$ = **5**). Asterisks (*) and circles (°) denote the statistical difference in value and variance respectively (p<0.05).

Similarly, to the WF, in the case of the *NDI* on the *SH* of *BPI* is significantly higher than on the *LA* and *UA* ($p = 0.03$ and $p = 0.03$ respectively). Because *BPI* subjects had the *NDI*-variance of 0 on the *LA*, we found high significance compared to the *UA* and *SH* ($p = 0.0$ and $p = 0.0$, respectively) (Figure 28). Respecting *dorsal* and *ventral*, no differences were found either in *NDI* or in the *NDI*-variance (Figure 29).

Alike, no differences were found regarding *NDI* nor the *NDI*-variance between any segment of *TR*. The same applies to *dorsal* and *ventral NDI*-results of *TR* (Figure 28/ Figure 29).

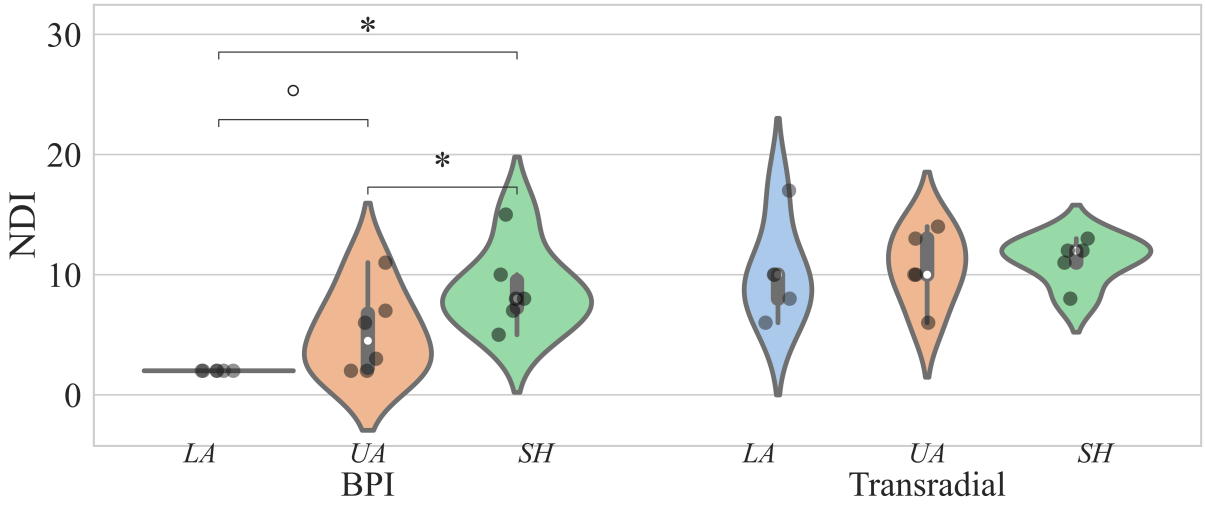

Figure 28 - Number of distinct intervals of BPIs and transradial amputees, comparing the single segments between each other. Each violin plot represents the density of data points at different values. The white dot marks the median, and the black box represents the interquartile range (IQR). Diamonds indicate statistical outliers within a single boxplot and dots indicate individual results ($\mathbf{n_{BPI}} = 6$, $\mathbf{n_{TR}} = \mathbf{5}$). Asterisks (*) and circles (°) denote the statistical difference in value and variance respectively ($p<0.05$).

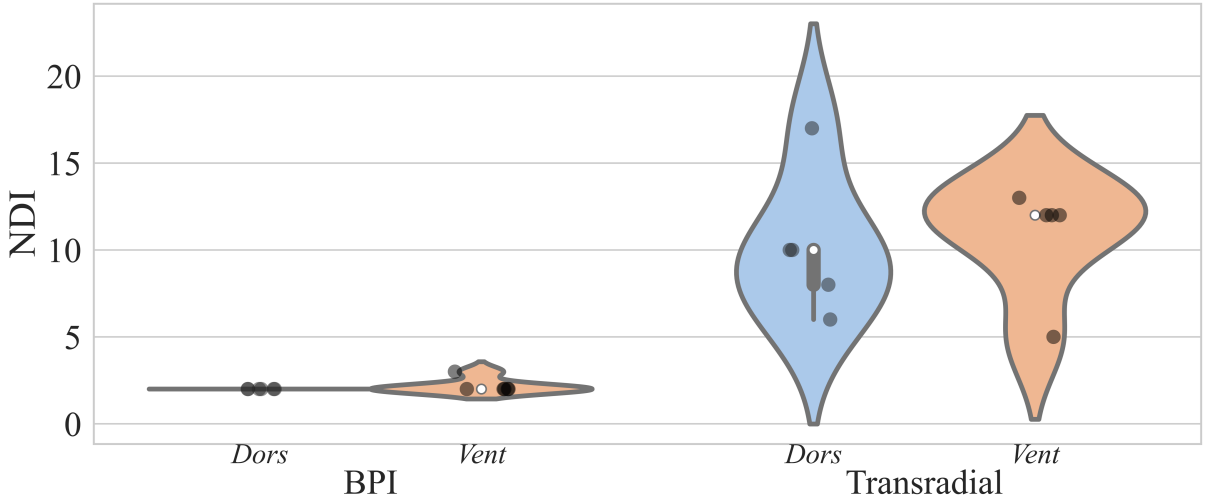

Figure 29 - Number of distinct intervals of BPIs and transradial amputees, comparing the dorsal and ventral sites between each other. Each violin plot represents the density of data points at different values. The white dot marks the median, and the black box represents the interquartile range (IQR). ($\mathbf{n_{BPI}} = 6$, $\mathbf{n_{TR}} = \mathbf{5}$).

3.1.2.4 TRs display results expected on the healthy arm, BPIs are significantly worse.

The *WF* was also similar among different groups and segments, excluding the lower arm of the *BPI*. Here, *AB* and *TR* show significantly lower *WF* (p = 0.0004 and p = 0.0043, respectively). In addition, with respect to *BPI*, *AB* had a significantly lower *WF* on the *UA* compared to *BPI* (p = 8.5e-05).

Regarding the *WF*-variance, *AB* had a significantly higher variance on the *LA* compared to *BPI* (p = 0.02). Additionally, *BPI* present a significantly higher variance than both *AB* and *TR* on the *UA* (p = 8.5e-05 and p = 0.02, respectively). *TR* display a significantly lower variance than both *AB* and *BPI* on the *SH* (p = 0.02 and p = 0.005, respectively) (Figure 30).

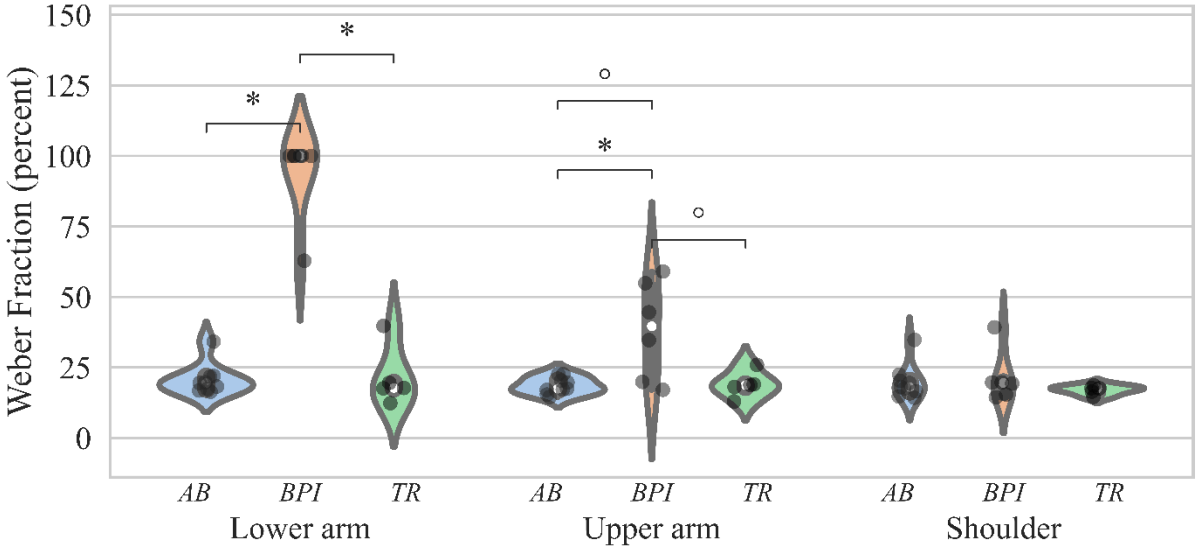

Figure 30 - Weber fraction. (in percent of the maximum stimulation amplitude) of healthy participants, BPIs and transradial amputees, comparing the single segments between populations. Each violin plot represents the density of data points at different values. The white dot marks the median, and the black box represents the interquartile range (IQR). The sensation threshold data were collected from ten able-bodied, six brachial plexus injured, and five transradial amputated subjects. Dots indicate individual results ($\mathbf{n_{able} = 10}$, $\mathbf{n_{BPI}}$= 6, $\mathbf{n_{TR} = 5}$). Asterisks (*) and circles (°) denote the statistical difference in value and variance respectively (p<0.05).

Comparing *dorsal* and *ventral*, similar to the sensation threshold, *BPI* had a significantly higher *WF* than *AB* and *TR* in both *dorsal* (p = 0.001 and p = 0.006 respectively) and *ventral* (p = 0.001 and p = 0.006 respectively). Additionally, the *WF*-variance between *AB* is significantly lower than between *BPI* on the *dorsal* (p = 0.002) (Figure 31).

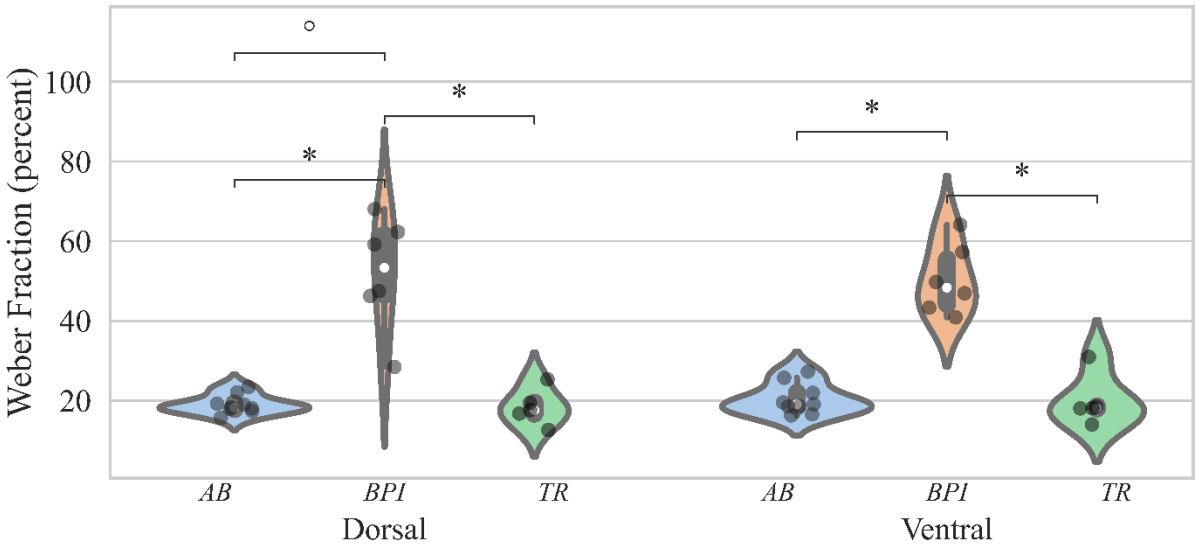

Figure 31 - Weber fraction (in percent of the maximum stimulation amplitude) of healthy participants, BPIs, and transradial amputees, comparing the dorsal and ventral sites between populations. Each violin plot represents the density of data points at different values. The white dot marks the median, and the black box represents the interquartile range (IQR). The sensation threshold data were collected from ten able-bodied, six brachial plexus injured, and five transradial amputated subjects. Dots indicate individual results ($\mathbf{n_{able} = 10}, \mathbf{n_{BPI}} = 6, \mathbf{n_{TR} = 5}$). Asterisks (*) and circles (°) denote the statistical difference in value and variance, respectively ($p<0.05$).

Comparing populations, both *AB* and *TR* show a significantly higher number than *BPI* in the *LA* ($p = 0.001$ and $p = 0.006$). Additionally, the *NDI* on the *UA* of *BPI* is significantly lower than the one of *AB* ($p = 0.008$). However, no significant differences were found between any of the groups in the *SH*-region.

Both *AB* and *TR* show a significantly lower *NDI*-variance than *BPI* in the *LA* ($p = 0.0$ and $p = 0.0$). Also, the variance in *NDI* between subjects on the *UA* of *BPI* is significantly higher than the one of *AB* ($p = 0.0.04$). No significant differences were detected between any subject group in the *SH*-region regarding *NDI*-variance (Figure 32).

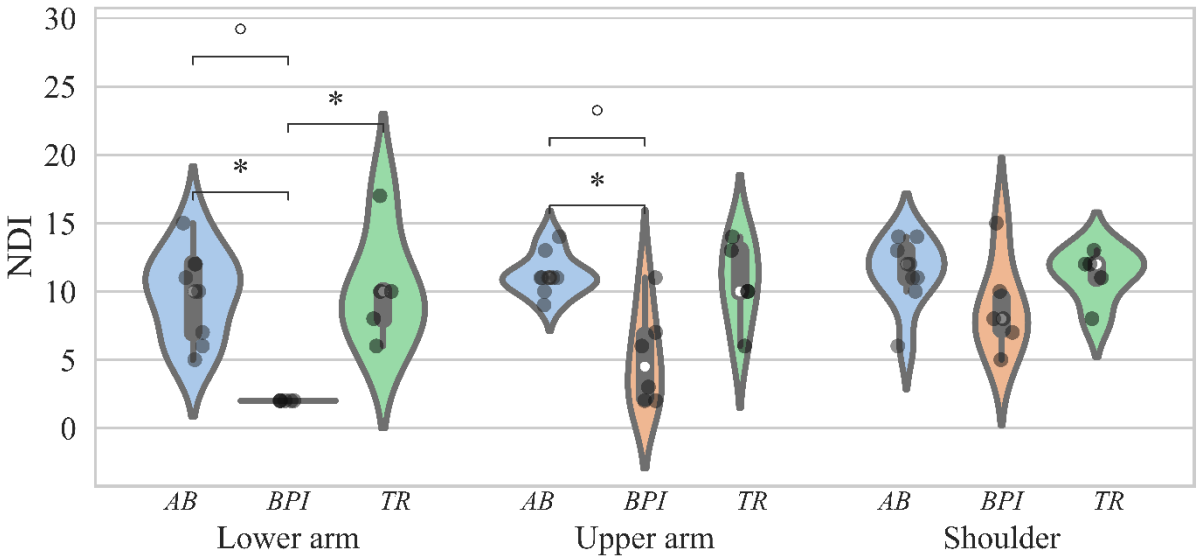

Figure 32 - Number of distinct intervals of healthy participants, BPIs and transradial amputees, comparing the single segments between populations. c. The sensation threshold data were collected from ten able-bodied, six brachial plexus injured, and five transradial amputated subjects. Dots indicate individual results ($\mathbf{n_{able} = 10}, \mathbf{n_{BPI}}$= 6, $\mathbf{n_{TR} = 5}$). Asterisks (*) and circles (°) denote the statistical difference in value and variance respectively ($p<0.05$).

Additionally, *AB* and *TR* show significantly higher NDI on *dorsal* and *ventral* compared to *BPI*. Furthermore, also the *NDI*-variance of *AB* is significantly higher in *dorsal* and *ventral* than in *BPI* (Figure 33).

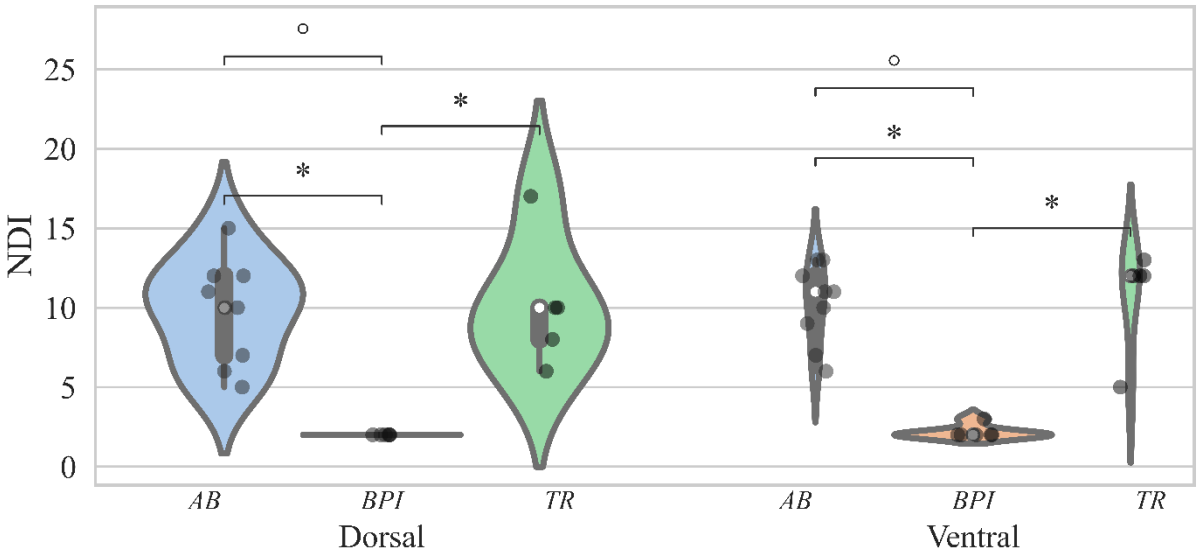

Figure 33 - Number of distinct intervals of healthy participants, BPIs and transradial amputees, comparing the dorsal and ventral sites between populations. Each violin plot represents the density of data points at different values. The white dot marks the median, and the black box represents the interquartile range (IQR). The sensation threshold data were collected from ten able-bodied, six brachial plexus injured, and five transradial amputated subjects. Dots indicate individual results ($\mathbf{n_{able} = 10}, \mathbf{n_{BPI}}$= 6, $\mathbf{n_{TR} = 5}$). Asterisks (*) and circles (°) denote the statistical difference in value and variance respectively ($p<0.05$).

3.1.2.5 Tracking performnce does not depend on the location where the feedback is provided.

The compensatory tracking task showed no significant differences between Visual (*Vis*), *LA*, *UA*, and *SH* in *BPI* or *TR,* neither regarding the delay (Figure 34A), correlation coefficient (Figure 34B), nor average rectified error (Figure 34C).

As discussed in the methods, since none of the *BPI* subjects could correctly distinguish between vibrations in the lower arm, it was not possible to perform the compensatory tracking tasks in this arm region for them. However, a significantly lower variance was detected on the *UA* of *TR* compared to the *LA* ($p = 0.001$) and *SH* ($p = 0.001$) concerning delay (Figure 34A).

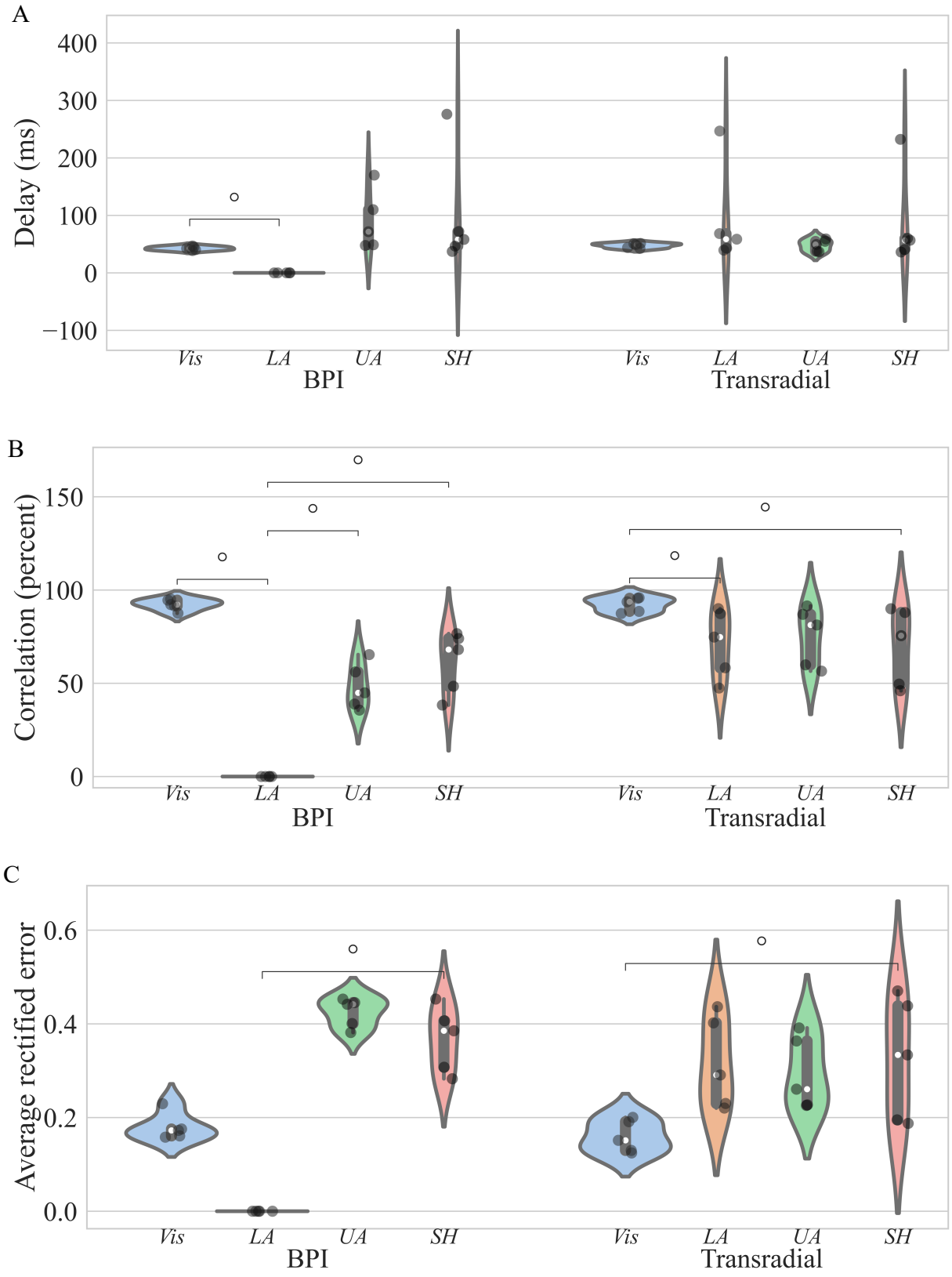

Figure 34 - Tracking task. (A) Delay (in ms), **(B)** correlation (in percent), and **(C)** average rectified error between target and cursor during the compensatory tracking task along the arm and shoulder region of BPIs and transradial amputees comparing the single segments between each other. Each violin plot represents the density of data points at different values. The white dot marks the median, and the black box represents the interquartile range (IQR). Dots indicate individual results ($\mathbf{n_{BPI}}$= 6, $\mathbf{n_{TR}}$ = **5**). Asterisks (*) and circles (°) denote the statistical difference in value and variance, respectively ($p < 0.05$).

3.1.2.6 Feedback on the shoulder/neck results in similar performance in all populations

The compensatory tracking task supplemented with visual feedback (*Vis*) showed no significant differences between populations. However, several differences were detected in the tactile feedback condition (visual feedback off).

No significant differences were found between *AB* and *TR* in any of the three outcome measurements (delay (Figure 35A), average rectified error (Figure 35B), and correlation (Figure 35C)). Additionally, all populations performed the same if feedback was applied to *SH*. However, *AB* performed the task with a significantly lower delay ($p = 0.04$), lower error ($p = 0.003$), and higher correlation ($p = 0.004$) than *BPI* if feedback was applied to the *UA*.

In terms of variance, no differences were found in the correlation. However, *AB* show a significantly lower variance in the delay than *BPI* when feedback is applied to *SH*; additionally, they show a significantly lower variance in delay ($p = 8.16e-06$) and error ($p = 0.02$) than *TR*, when feedback is applied to *SH*. Lastly, a significantly lower variance in delay was seen when comparing the *LA* of AB and *TR* ($p = 1.06e-07$).

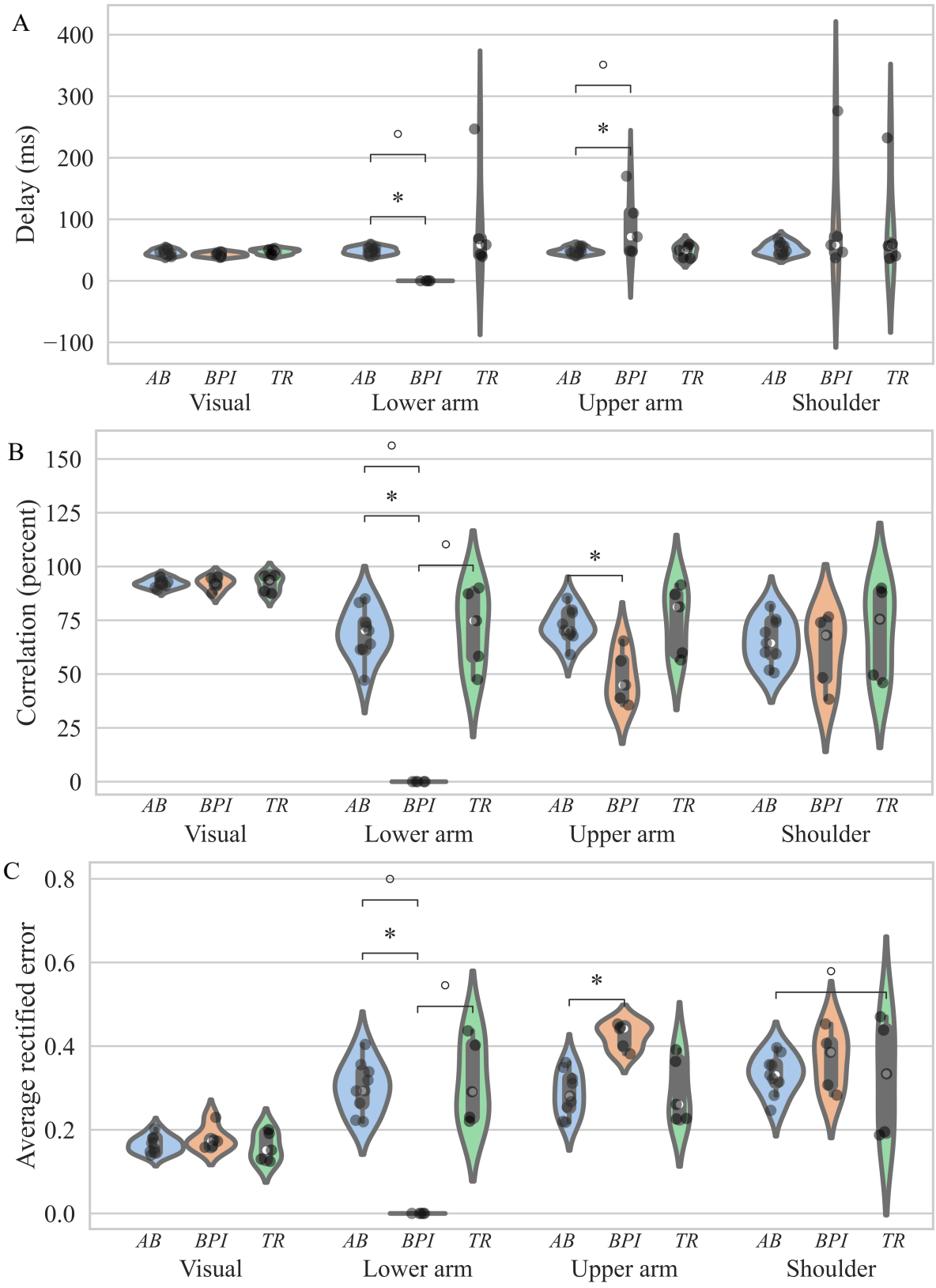

Figure 35 - Tracking task. (A) Delay (in ms), **(B)** correlation (in percent), and **(C)** average rectified error between target and cursor during the compensatory tracking task along the arm and shoulder region of healthy participants, BPIs and transradial amputees comparing the single segments between populations. Each violin plot represents the density of data points at different values. The white dot marks the median, and the black box represents the interquartile range (IQR). Dots indicate individual results ($\mathbf{n_{able} = 10}, \mathbf{n_{BPI}}$= 6, $\mathbf{n_{TR} = 5}$). Asterisks (*) and circles (°) denote the statistical difference in value and variance respectively ($p < 0.05$).

3.2 NEUROPATHOPHYSIOLOGICAL MORPHOLOGIES OF NEUROMAS

3.2.1 Morphologies of transected peripheral nerves

During microscopic analysis, neuroma and controls showed following different classes of (nervous) tissue qualities:

- Fascicles (Figure 36A); further on denominated as organized nervous tissue
- Minifascicles (Figure 36B); further on denominated as unorganized nervous tissue
- Fat (Figure 36C)
- Connective tissue (Figure 36D)
- Erythrocytes (Figure 36E)

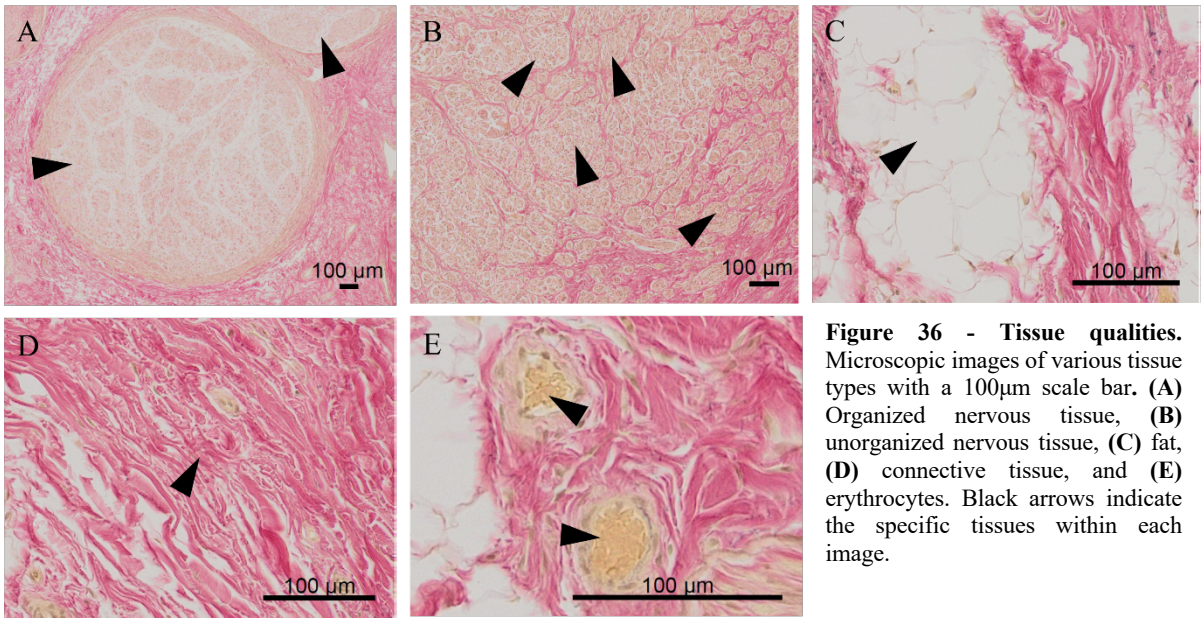

Figure 36 - Tissue qualities. Microscopic images of various tissue types with a 100µm scale bar**. (A)** Organized nervous tissue, **(B)** unorganized nervous tissue, **(C)** fat, **(D)** connective tissue, and **(E)** erythrocytes. Black arrows indicate the specific tissues within each image.

Furthermore, some samples presented organized, next to unorganized nervous tissue on the same nerve (Figure 37).

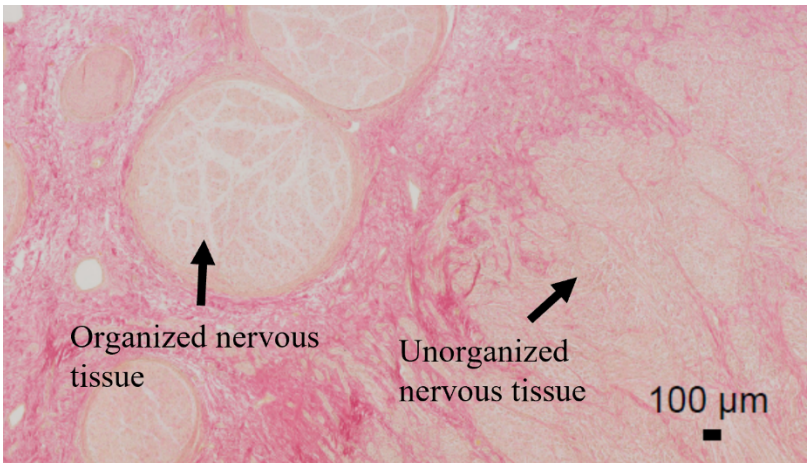

Figure 37 - Coexistence. Microscopic images of an exemplary nerve presenting organized next to unorganized nervous tissue with a 100µm scale bar.

Additionally, some samples presented fat and muscular tissue outside the nerve. These tissues were excluded from the analysis, except for muscular tissue invaded by unorganized nervous tissue (Figure 38).

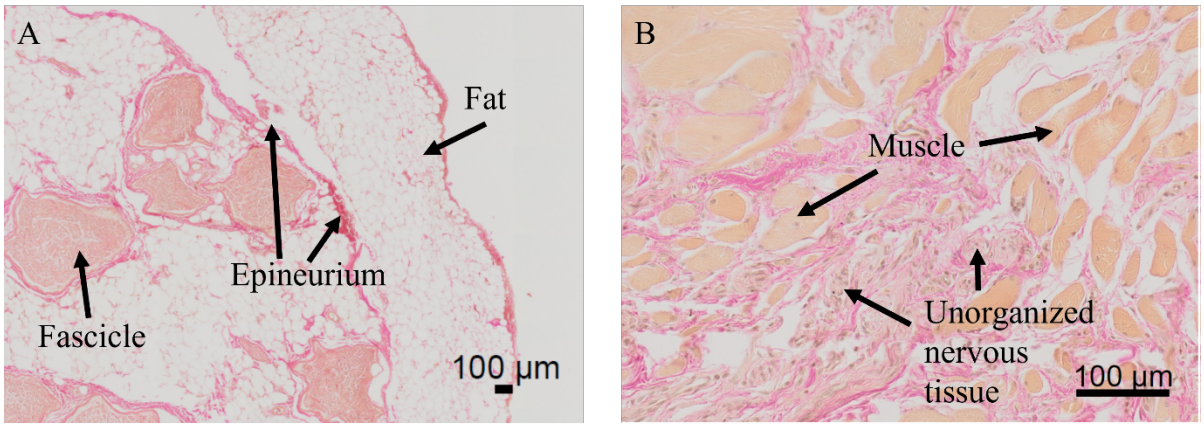

Figure 38 - Tissue exclusion. Microscopic images of **(A)** fat and **(B)** muscle outside the nerve with a 100µm scale bar**.** The fat was excluded from further analysis, muscular tissue was included in the cases in which unorganized nervous tissue intruded it.

3.2.2 Methodology and algorithms for the image analysis

3.2.2.1 Color deconvolution

Color deconvolution was verified together with the department of neuropathology and recognized as successful for random chunks of all Hematoxylin/DAB stainings (Figure 39).

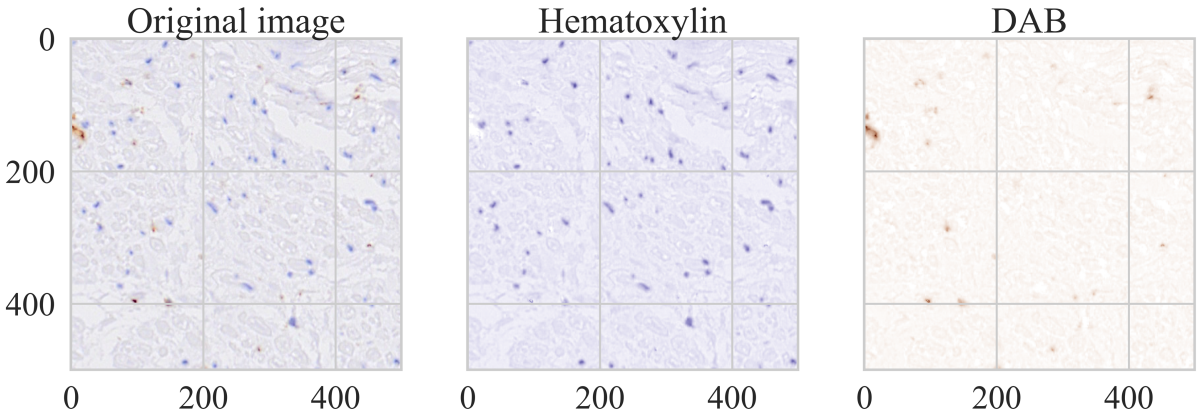

Figure 39 - Color deconvolution. The original image is separated into the different stains: Hematoxylin and DAB (exemplary for KiM1P-staining).

Nuclei and DAB-staining are successfully masked using adaptive thresholding (Figure 40). The nuclei-mask displays the nuclei's location and surrounding area, as positive staining does not necessarily overlap with the nucleus but is situated in its surroundings.

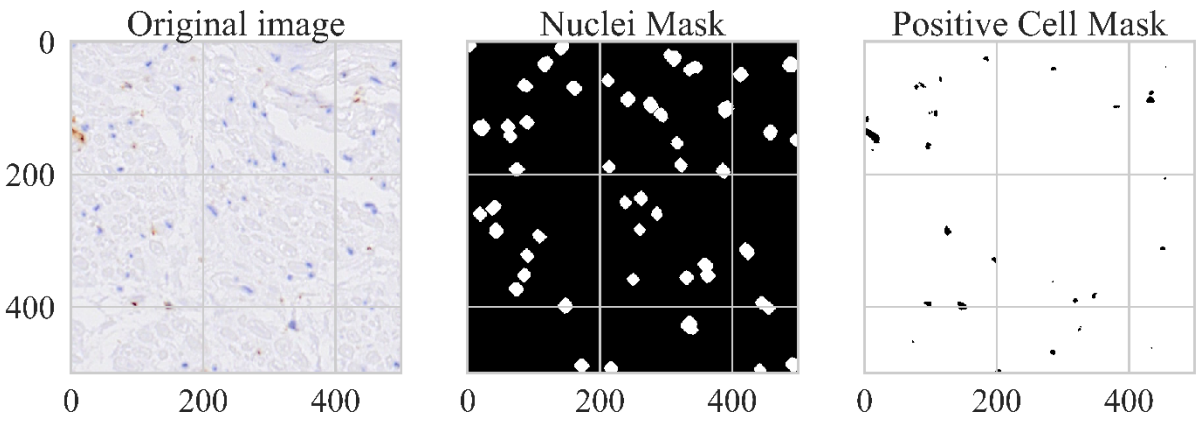

Figure 40 – Nuclei/ DAB masks for detected nuclei and DAB-positive tissue, respectively (exemplary for KiM1P-staining).

After masking the DAB-positive tissue with a mask composed of the nuclei and surrounding area, DAB-positive cells are correctly identified (Figure 41).

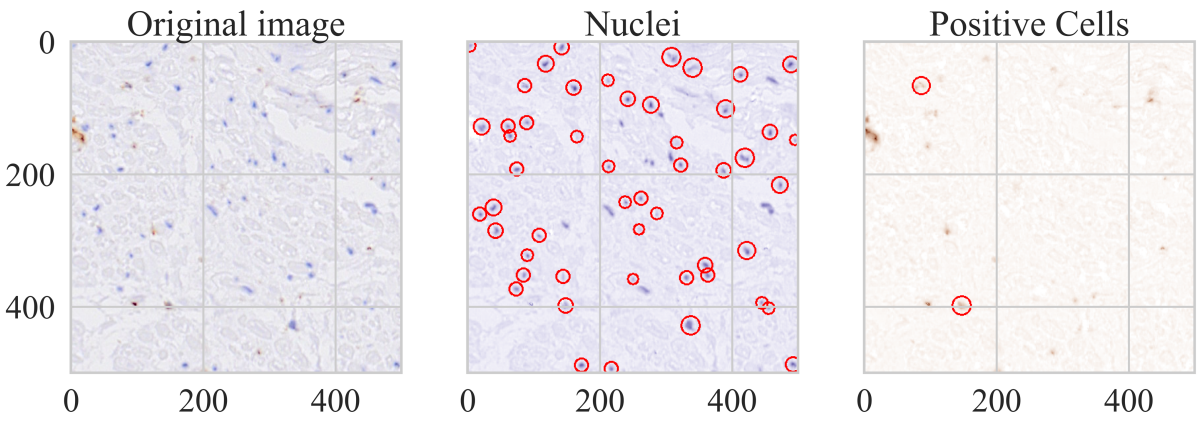

Figure 41 - Positive cell detection. Nuclei and DAB-positive cells are marked in red circles (exemplary for KiM1P-staining).

Similarly, DAB-positive Schwann-cells are correctly identified (Figure 42).

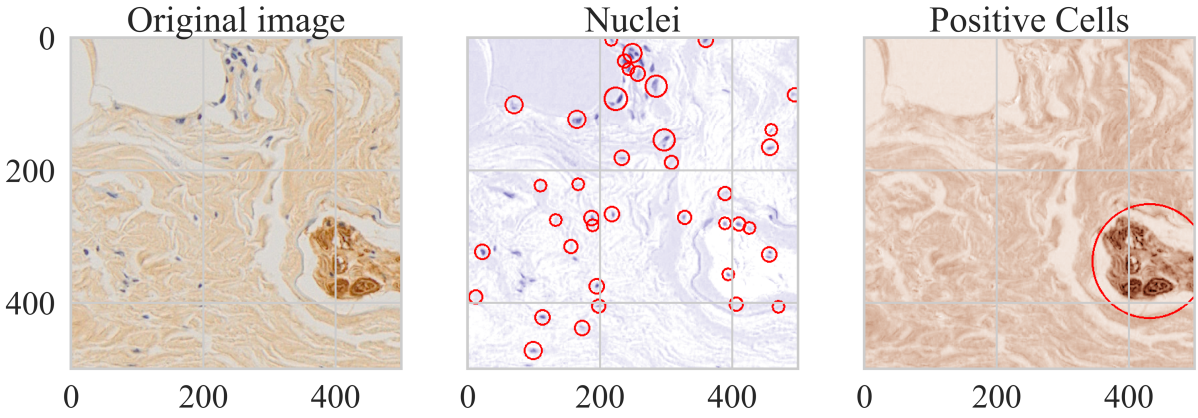

Figure 42 - S100 detection. Nuclei and DAB-positive area after filtering are marked with red circles.

3.2.2.2 Unsupervised learning using K-Means presents insufficient results.

Together with the department of neuropathology, it was verified that the image segmentation using K-Means does not properly differentiate between organized and unorganized nervous tissue (both red) (Figure 43).

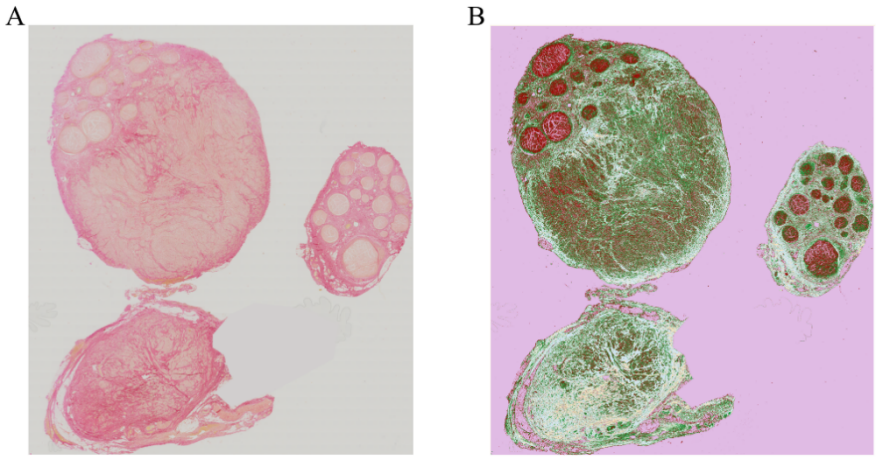

Figure 43 – K-Means result. Output of a K-Means algorithm applied to a nerve containing organized, as well as unorganized nervous tissue (exemplary for one patient). The quantized image was trained for six classes.

3.2.2.3 Supervised learning performs successful segmentation.

During the model validation, it was verified together with department of neuropathology, that the selected tissue as well as the segmentation using a Random Forest Algorithm and after postprocessing were meaningful (Figure 44).

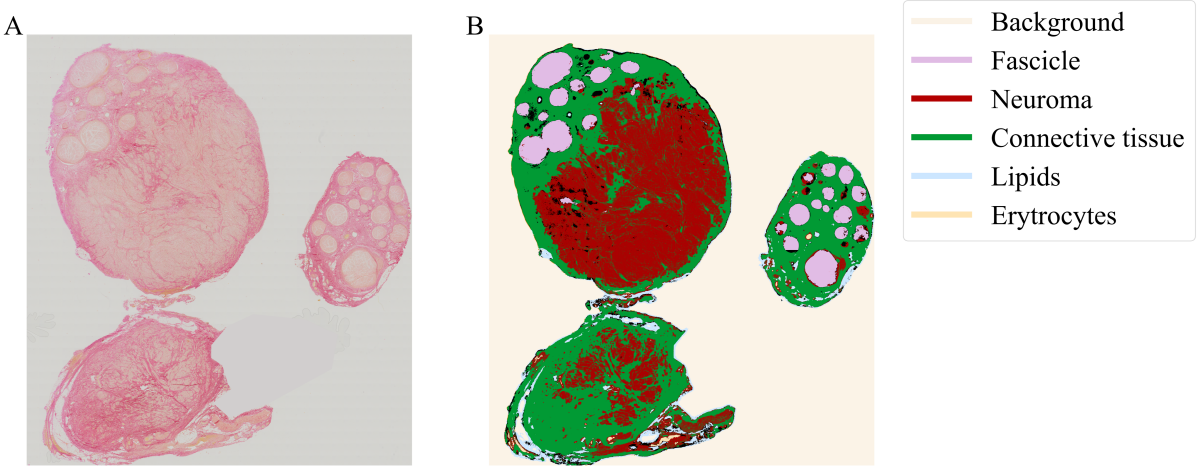

Figure 44 - Segmented nerve. (A) Nerve image from the slide scanner and **(B)** segmented image as output from the algorithm (exemplary for one patient).

Additionally, the report provided by the model itself was evaluated. The scores are calculated using each model's confusion matrix, which represents the segmentation results using the training labels (exemplary for one model in Figure 45).

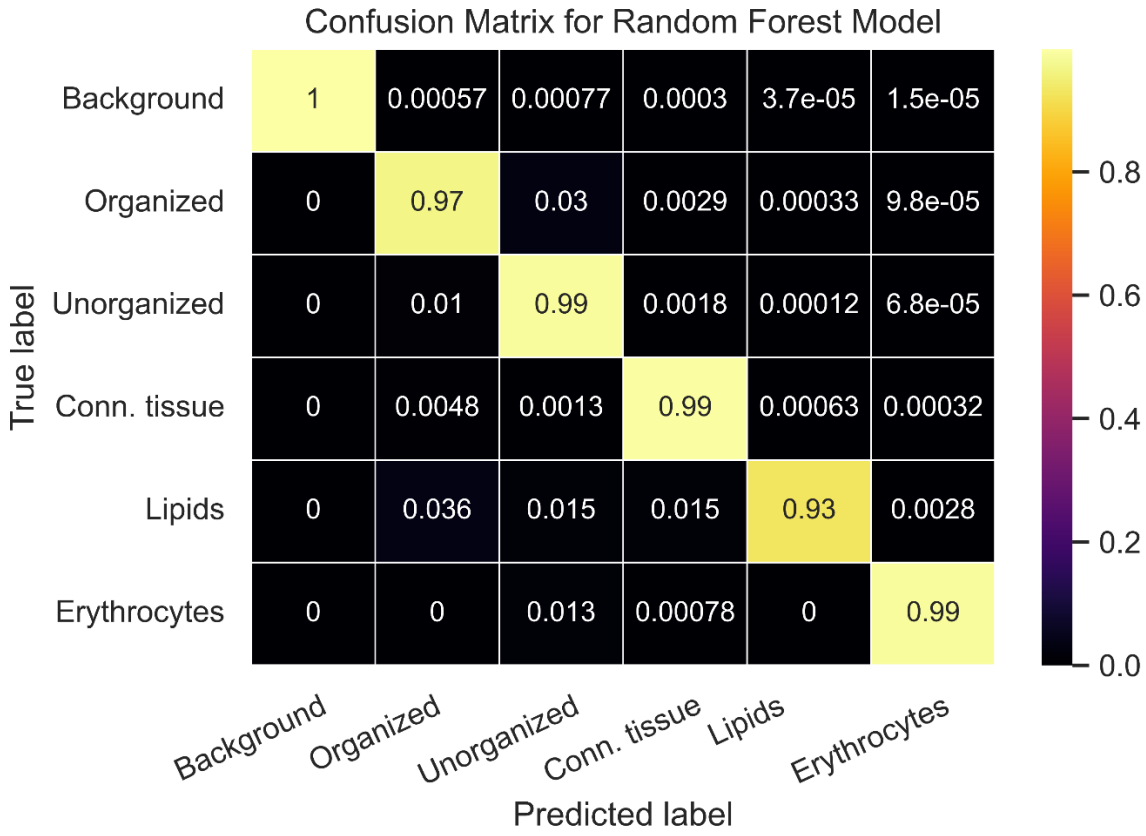

Figure 45 - Confusion matrix. Confusion matrix for the Random Forest classifier with 200 trees with a maximal depth of 30 each and with a maximum of 50% of the total samples drawn from the dataset when constructing each of it using scikit-learn. The rows represent the true labels, while the columns represent the predicted labels. Each cell value (i, j) indicates the number of samples with true label i that were classified as label j. The diagonal elements (in bold) represent the correctly classified samples, while the off-diagonal elements correspond to misclassified samples (exemplary for one model).

All models showed an accuracy, F1-score, precision, and recall above 0.95 (all scores: 0.99 [0.01]) (Figure 46).

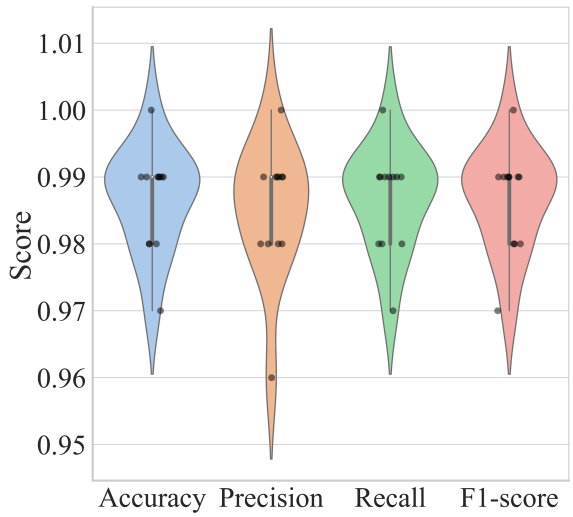

Figure 46 - Accuracy report. Performance metrics (Accuracy, F1-score, Precision, and Recall) for the different models applied to the images. Each violin represents the distribution of values for the respective performance metric, with the width indicating the density of data points at different values. The white dot marks the median, and the black box represents the interquartile range (IQR).

During K-Fold cross-validation, the model' performance and consistency across different subsets of the data. The models achieved a median accuracy of 98.7% with an IQR of 0.94% across the 10 folds (Figure 47).

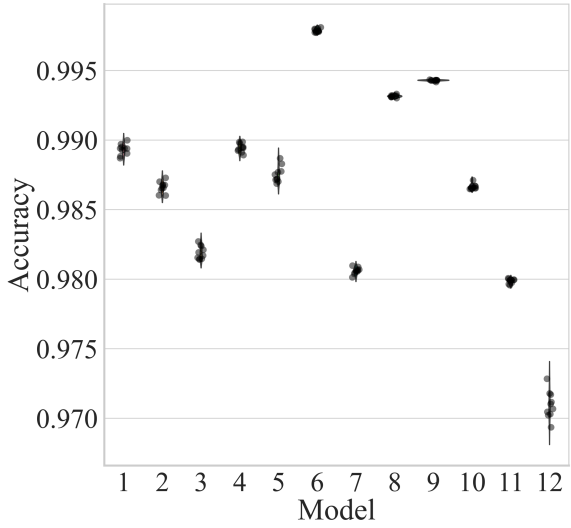

Figure 47 - K-Fold cross-validation. K-Fold cross-validation results for every model trained. K was set to 10.

Further, several random cross-predictions were performed, in which an image of a control nerve was presented to a model trained to find unorganized nervous tissue, to test the model for robustness against color variations and overfitting. When applying a model trained on an set of features from an image without unorganized nervous tissue to the image where the set of features is from, the resulting segmentation shows 50039 correctly vs. 815 incorrectly labeled pixels for "background", 52387 correctly vs 192 incorrectly labeled pixels for "organized nervous tissue", 11943 correctly vs. 161 incorrectly labeled pixels for "connective tissue", and 3688 correctly vs. 130 incorrectly labeled pixels for "fat tissue" (Figure 48; Figure 49A). When applying a model trained on a set of features from an image with unorganized nervous tissue to an image without unorganized nervous tissue, the resulting segmentation shows 50040 correctly vs 814 incorrectly labeled pixels for "background", 52390 correctly vs. 189 incorrectly labeled pixels for "organized nervous tissue", 11946 correctly vs. 158 incorrectly labeled pixels for "connective tissue", and 3685 correctly vs. 133 incorrectly labeled pixels for "fat tissue". No pixel was labeled as "unorganized nervous tissue" (Figure 48; Figure 49B).

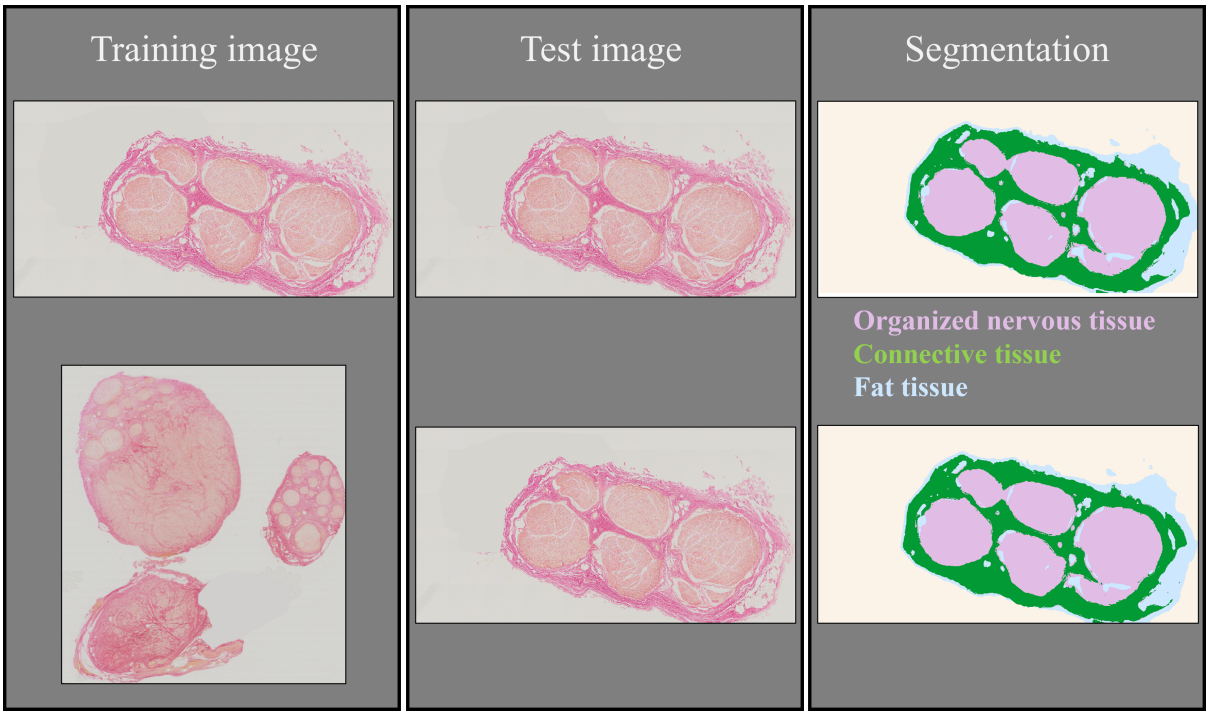

Figure 48 – Cross segmentation. The segmentation is satisfactory, no matter if the algorithm was trained using the same image (upper row) or a different image containing unorganized nervous tissue (lower row).

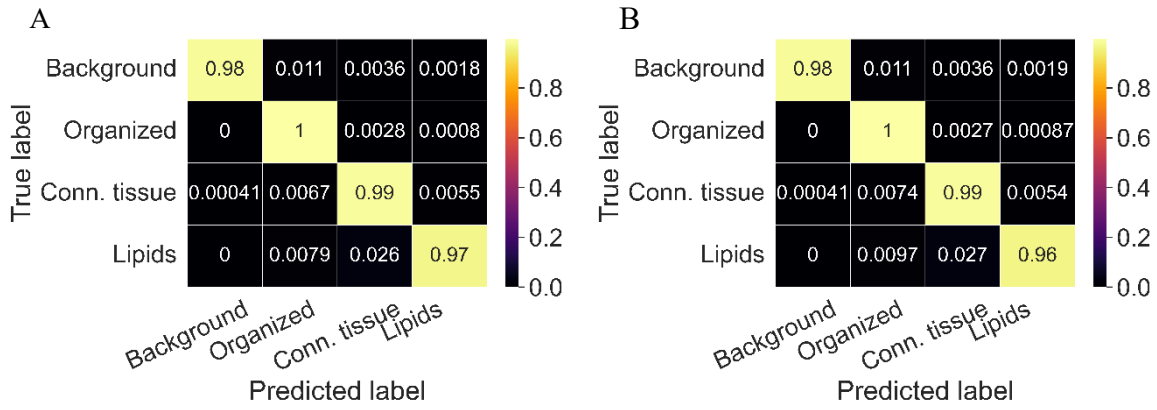

Figure 49 - Confusion matrix. Confusion matrix for the segmentation of an image without unorganized nervous tissue using a model trained on **(A)** the same image and **(B)** an image containing unorganized nervous tissue. Each cell value (i, j) indicates the number of samples with true label i that were classified as label j. The diagonal elements (in bold) represent the correctly classified samples, while the off-diagonal elements correspond to misclassified samples (exemplary for one model).

Due to the high computational costs, the images were reduced to 10% of their size before training the models and performing the segmentation. To validate if this reduction has some kind of effect on the resulting segmentation, a test was performed on a small chunk. For this purpose, three models were trained. One model was trained on the unmodified chunk, using a range of gaussian filtering values relative to the ones used during the experiments (10-160)(Figure 50C), One model was trained on the chunk with a reduced size to 10% and a range of gaussian filtering values like the ones used during the experiments (1-16) (Figure 50B), and lasty, a

model was trained on the unmodified image and a range of gaussian filtering values like the ones used during the experiments (1-16)(Figure 50D). The resulting sizes of the feature matrices were 2.53 GB for the unmodified images (Figure 50C-D) and 0.024 GB for the reduced image (Figure 50B). The overall computation times were 301.35s for the unmodified image (Figure 50C), 388.96s for the unmodified image using the relatively reduced gaussian filtering values (Figure 50D), and 5.75s for the reduced image (Figure 50B).

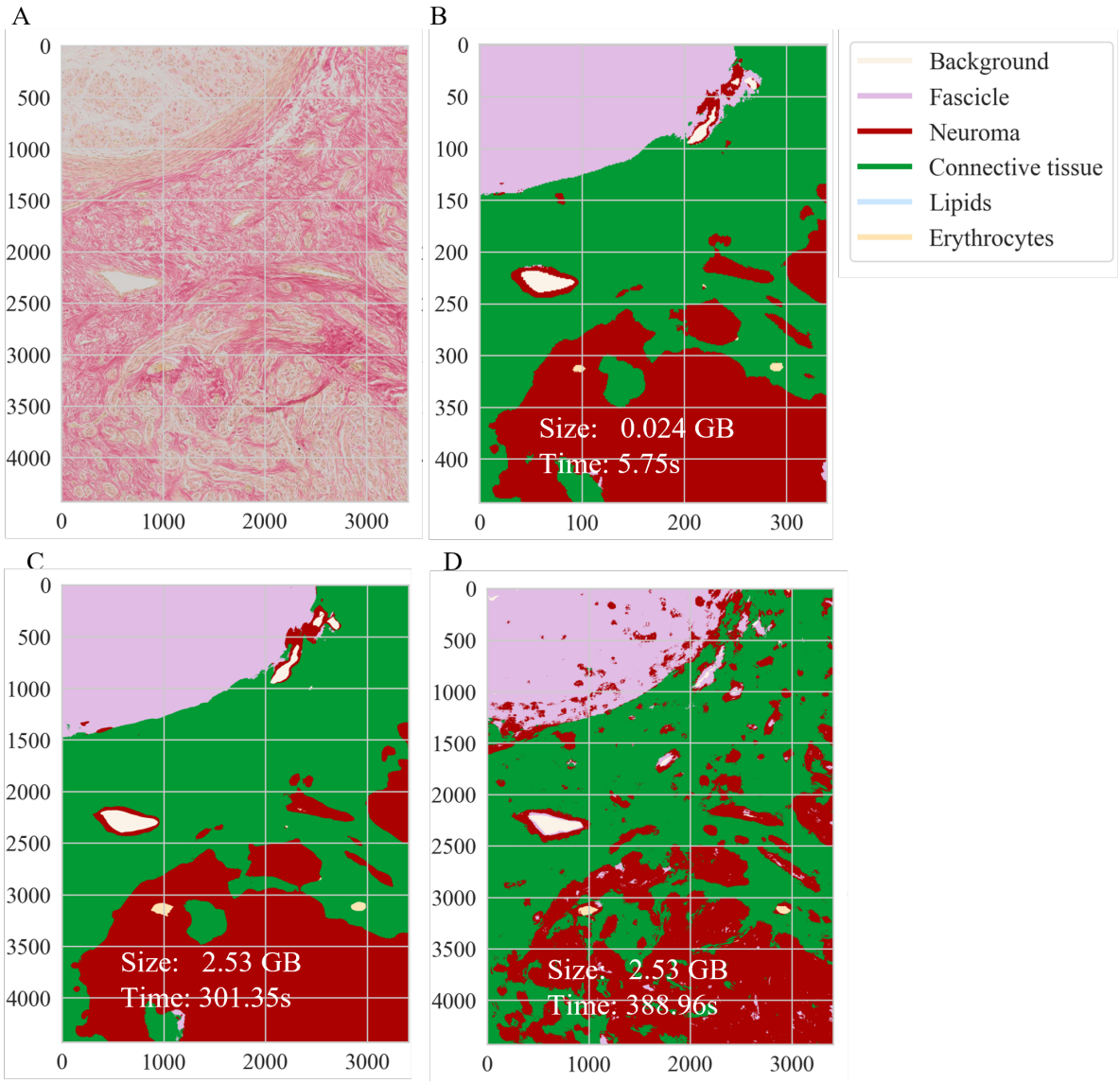

Figure 50- Image resizing. (A) Chunk from a nerve image from the slide scanner (B) the segmented image as output trained using the original sized image and a gaussian filter between 10 and 160 during feature extraction, (C) an image reduced to 10% of its size and a gaussian filter between 1 and 16 during feature extraction, and (D) the original image and a gaussian filter between 1 and 16 during feature extraction

3.2.3 Factors contributing to neuroma pain.

3.2.3.1 T-Lymphocytes

No significant difference in the normalized density of T-lymphocytes was detected comparing control nerves with neuromas. However, it was found when adding the normalized deviation of organized and unorganized tissue ($p = 0.034$) (Figure 51).

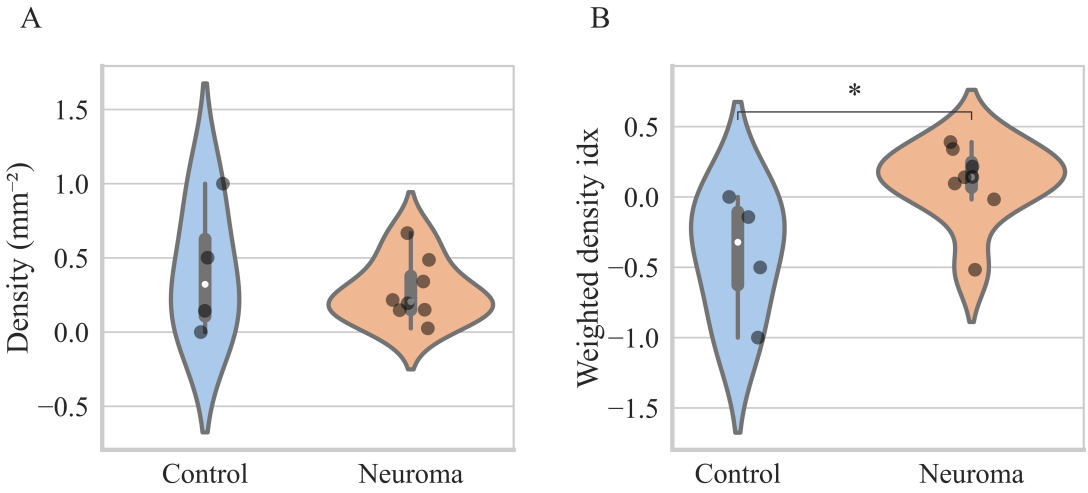

Figure 51 - T-lymphocytes: Controls vs. neuroma. (A) Normalized density and **(B)** weighted deviation index of T-lymphocytes in control patients and patients with a neuroma. Each violin plot represents the density of data points at different values. The white dot marks the median, and the black box represents the interquartile range (IQR). An asterisk (*) indicates $p < 0.05$.

Equally, no differences were detected comparing neuromas from patients who do not report pain with neuromas from patients who report neuroma-related pain in the normalized density, but they were in the weighted deviation index ($p = 0.034$) (Figure 52).

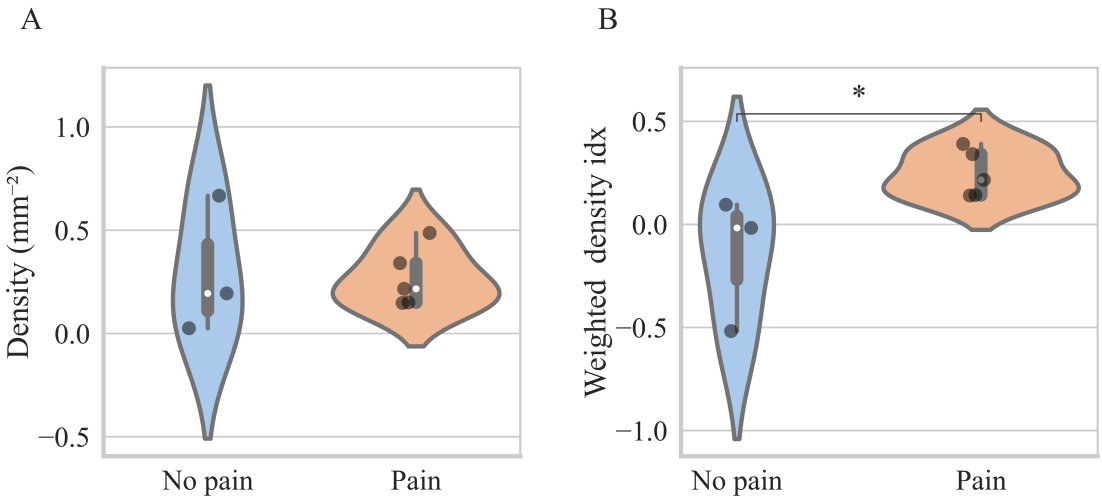

Figure 52 - T-Lymphocytes: No pain vs. pain. (A) Normalized density and **(B)** weighted deviation index of T-lymphocytes in patients with and without neuroma pain. Each violin plot represents the density of data points at different values. The white dot marks the median, and the black box represents the interquartile range (IQR). An asterisk (*) indicates $p < 0.05$.

Upon further examination of the two groups experiencing pain, a connection was found between the weighted density index of T-lymphocytes, and the level of pain reported on the VAS scale (p = 0.033) (Figure 53).

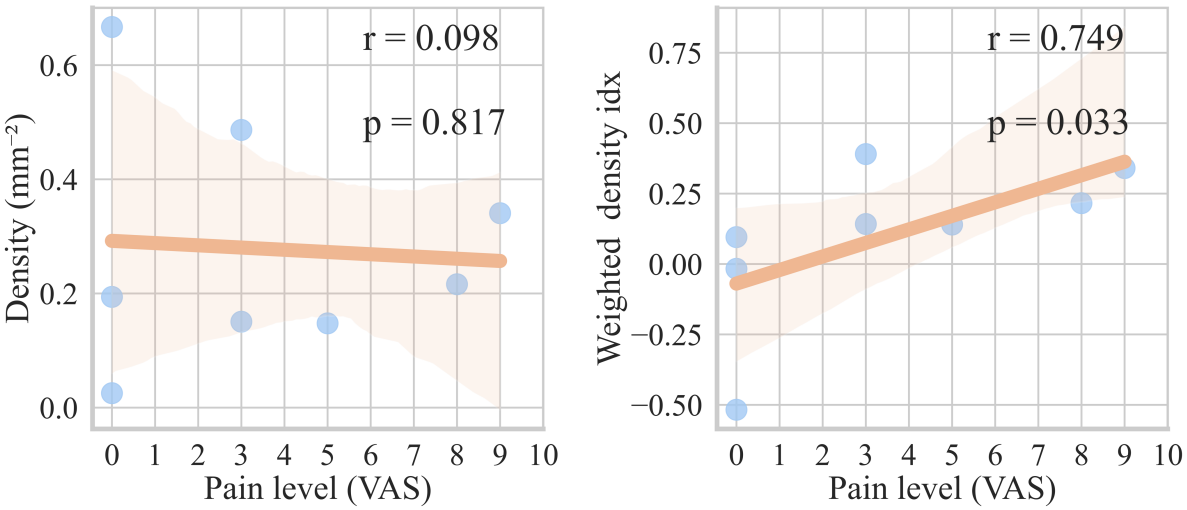

Figure 53 - Correlation of the number of T-Lymphocytes with pain. Correlation between the **(A)** normalized density and **(B)** weighted deviation index of T-lymphocytes with the pain level (VAS) reported by the patients (controls excluded). The correlation coefficient (r) and p-Value (p) where calculated using Spearman's correlation.

3.2.3.2 Schwann cells

No significant differences in the area covered by Schwann cells were detected in relation to the total area of nervous tissue while comparing control nerves with neuromas. However, when investigating the weighted area index, a significantly higher index was detected in neuroma patients (p = 0.006) (Figure 54).

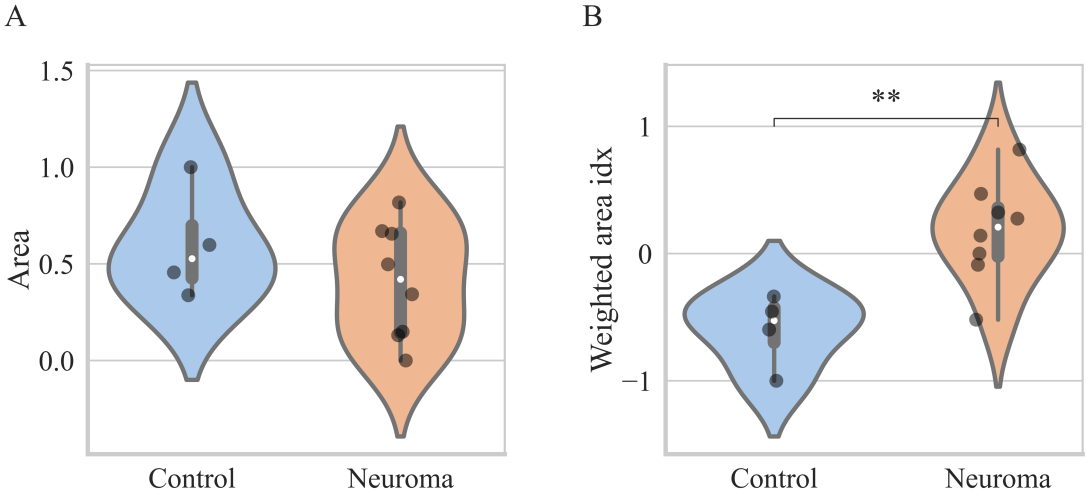

Figure 54 – Schwann cells: Controls vs. neuroma. (A) Normalized area and **(B)** weighted area index of Schwann cells in control patients and patients with a neuroma. Each violin plot represents the density of data points at different values. The white dot marks the median, and the black box represents the interquartile range (IQR). Two asterisks (**) indicate p < 0.01.

There was no significant difference comparing the neuromas of patients who did not report pain to those who experienced neuroma pain, neither in the normalized area covered Schwann-cells, nor in the weighted area index (Figure 55).

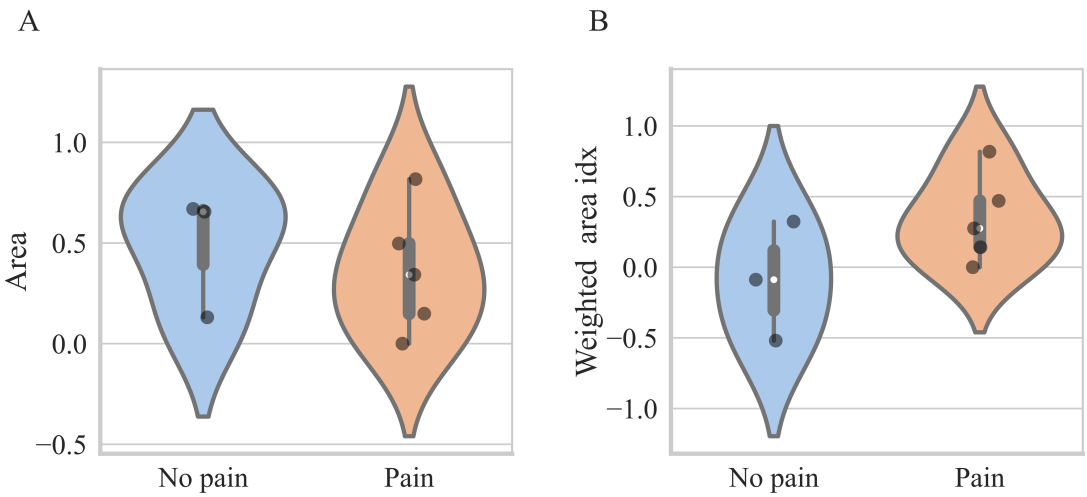

Figure 55 – Schwann cells: No pain vs. pain. (A) Normalized area and **(B)** weighted deviation index of Schwann cells in patients with and without neuroma pain. Each violin plot represents the density of data points at different values. The white dot marks the median, and the black box represents the interquartile range (IQR).

A deeper look into the two pain groups revealed a significant correlation between the area covered by Schwann cells and the reported pain level (VAS scale) related to the area covered by unorganized nervous tissue. No differences were detected either related to the full area of nervous tissue nor organized nervous tissue (Figure 56).

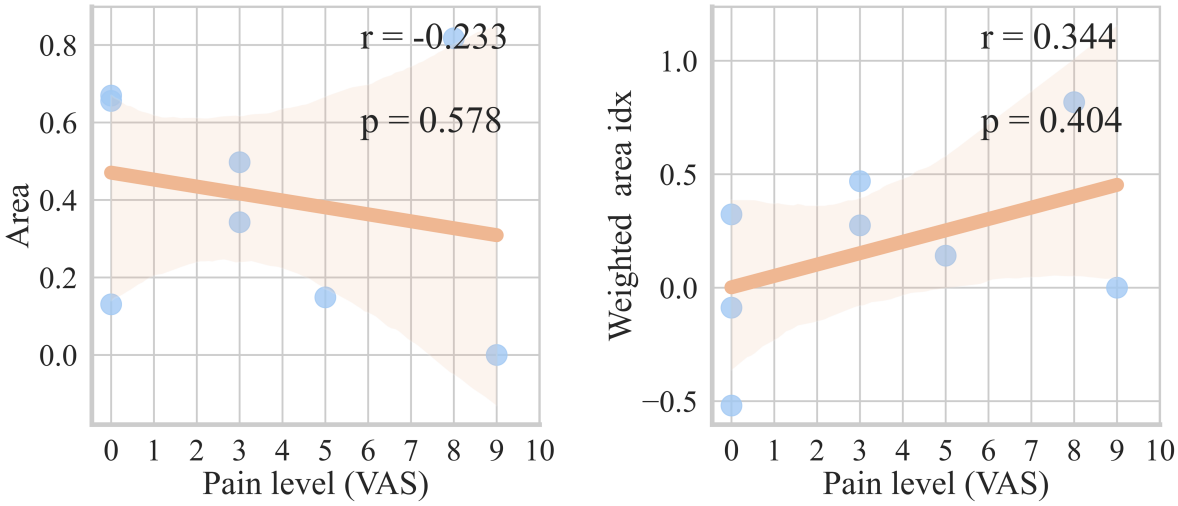

Figure 56 - Correlation of the percentual area covered by Schwann cells with pain. Correlation between the **(A)** normalized area and **(B)** weighted area index of Schwann-cells with the pain level (VAS) reported by the patients (controls excluded). The correlation coefficient (r) and p-Value (p) where calculated using Spearman's correlation.

3.2.3.3 Macrophages

No significant differences in the normalized density, nor in the weighted deviation index of macrophages were detected (Figure 57).

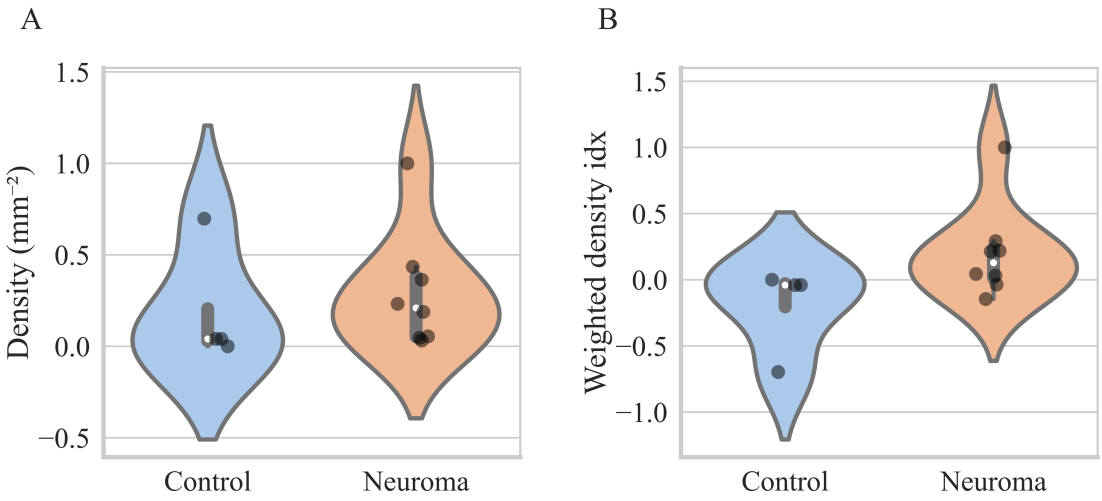

Figure 57 – Macrophages: Controls vs. neuroma. (A) Normalized density and **(B)** weighted deviation index of macrophages in control patients and patients with a neuroma. Each violin plot represents the density of data points at different values. The white dot marks the median, and the black box represents the interquartile range (IQR).

Similarly, no differences were detected in either condition comparing neuromas from patients who do not report pain with neuromas from patient who report neuroma related pain (Figure 58).

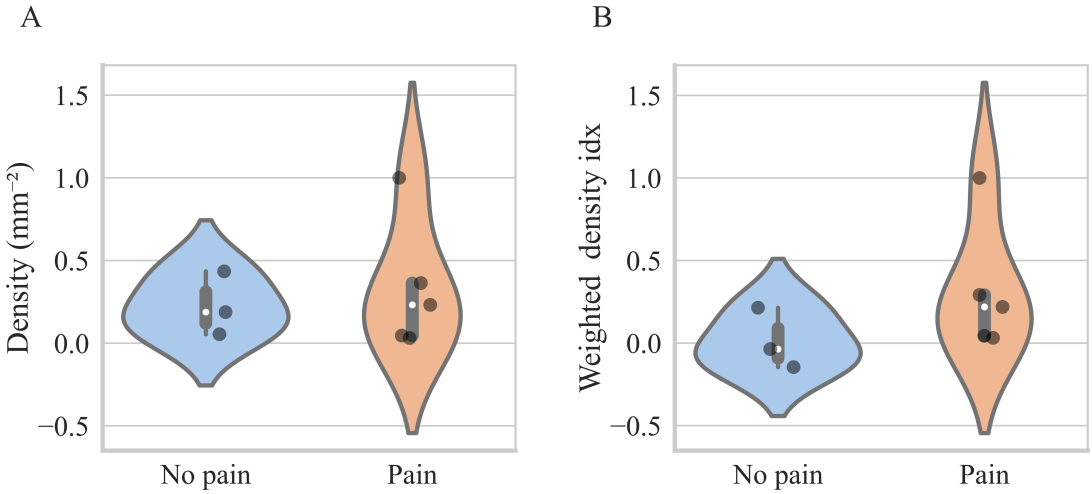

Figure 58 - Macrophages: No pain vs. pain. (A) Normalized density and **(B)** weighted deviation index of macrophages in patients with and without neuroma pain. Each violin plot represents the density of data points at different values. The white dot marks the median, and the black box represents the interquartile range (IQR).

A deeper look into the two pain groups revealed no correlation between the normalized density, or the weighted deviation index of T-lymphocytes and the reported pain level (VAS scale) (Figure 59).

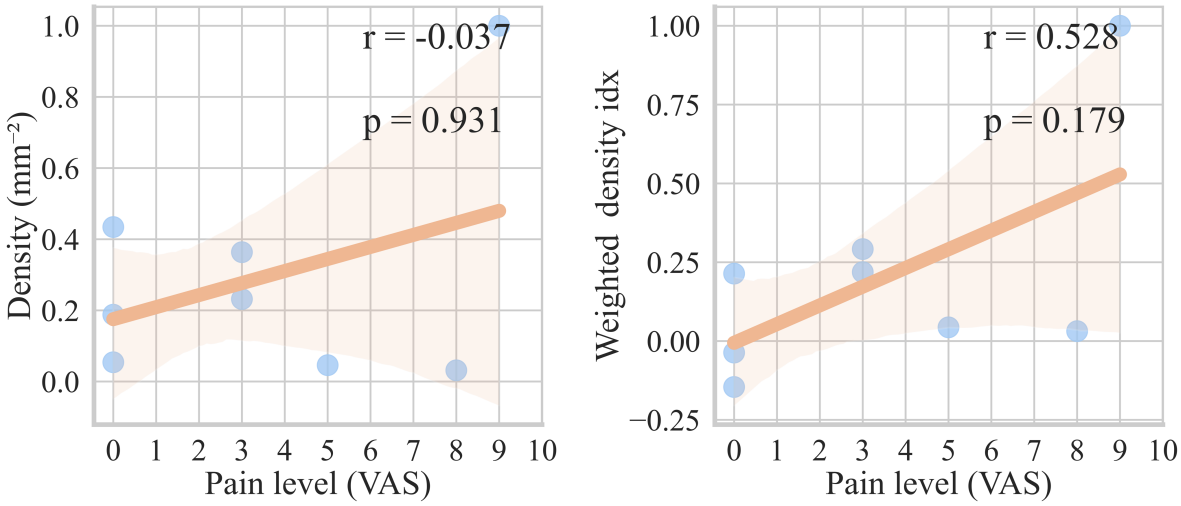

Figure 59 - Correlation of the number of macrophages with pain. Correlation between the **(A)** normalized density and **(B)** weighted deviation index of macrophages with the pain level (VAS) reported by the patients (controls excluded). The correlation coefficient (r) and p-Value (p) where calculated using Spearman's correlation.

3.2.3.4 Controls only display a higher relative amount of fat tissue.

Besides in the relative amount of unorganized nervous tissue ($p = 0.003$), significant differences between controls and patients were also found in the relative amount of fat tissue, being higher in the controls ($p = 0.01$).

However, no differences were found in the relative amount of organized nervous tissue or in the relative amount of connective tissue (Figure 60).

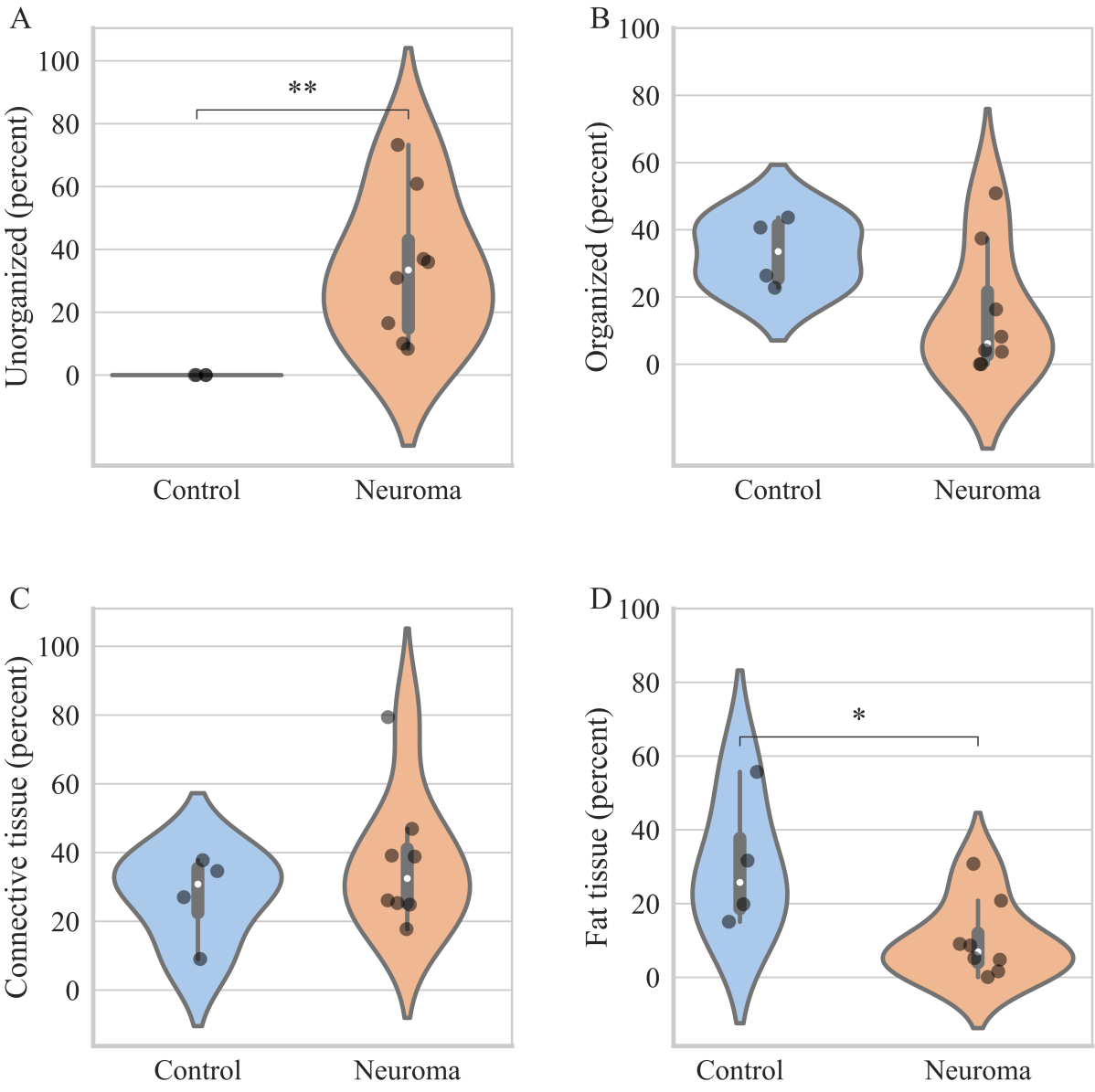

Figure 60 - Relative: Control vs. neuroma. (A) Amount of unorganized nervous tissue, **(B)** organized nervous tissue, **(C)** connective tissue, and **(D)** fat tissue in relation to the nerve's size in control patients and patients with a neuroma. Each violin plot represents the density of data points at different values. The white dot marks the median, and the black box represents the interquartile range (IQR). An asterisk (*) indicates $p < 0.05$, two asterisks (**) indicate $p < 0.01$.

In the analyses evaluating the absolute area, no significant difference between controls and patients was found regarding the total area of tissue, besides in unorganized nervous tissue ($p = 0.003$). The amount of organized nervous tissue, along with connective tissue, and fat tissue are not significantly different between populations (Figure 61).

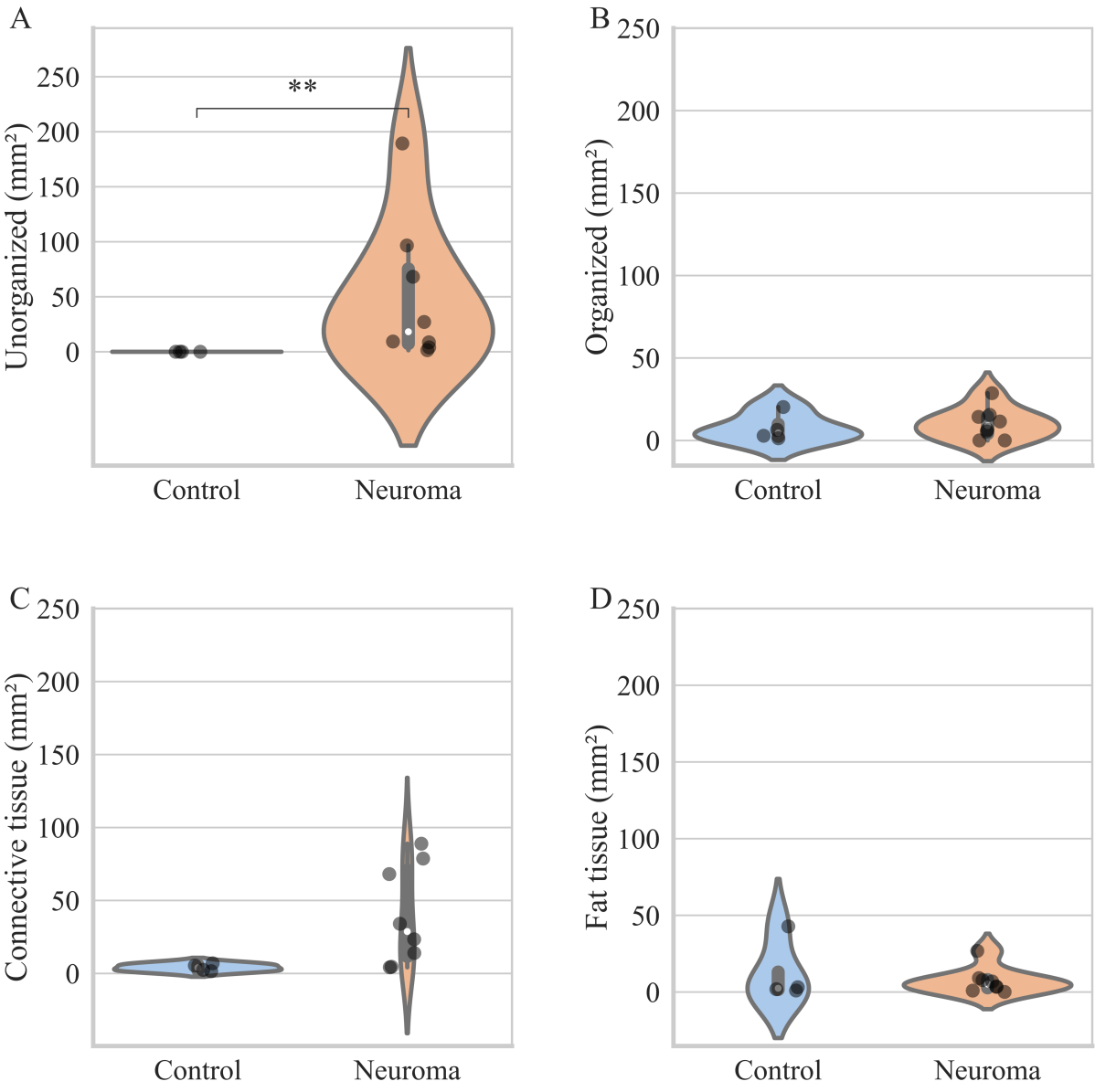

Figure 61 - Absolute: Control vs. neuroma. (A) Total area of unhealthy nervous tissue, **(B)** organized nervous tissue, **(C)** connective tissue, and **(D)** fat tissue in control patients and patients with a neuroma. Each violin plot represents the density of data points at different values. The white dot marks the median, and the black box represents the interquartile range (IQR).Two asterisks (**) indicate $p < 0.01$.

Additionally, also the total areas of the nerves are not significantly different from each other (Figure 62).

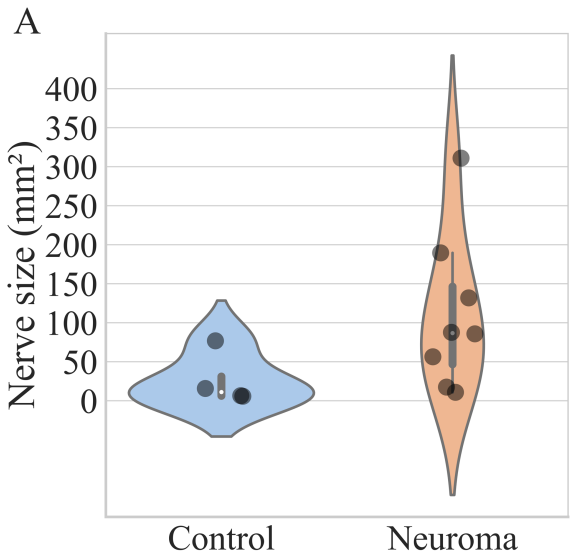

Figure 62 - Absolute nerve size. in control patients and patients with a neuroma. Each violin plot represents the density of data points at different values. The white dot marks the median, and the black box represents the interquartile range (IQR)..

3.2.3.5 Painful neuromas have lower relative amounts of organized nervous tissue.

Interestingly, the relative amount of organized nervous tissue ($p = 0.006$) is significantly higher in patients without reported neuroma-related pain; however, it does not cover a significantly larger area.

Looking into the neuroma subgroup, patients show no significant differences neither in the relative amount of unorganized nervous tissue nor in the amount of connective tissue, the relative amount of fat tissue, the relative amount of connective tissue intruding nervous tissue, and the relative amount of unorganized nervous tissue including intruding connective tissue comparing patients suffering from neuroma-related pain and patients without pain (Figure 63). Similarly, any significant dissimilarity was detected in any other tissue, including the total nerve sizes (Figure 64).

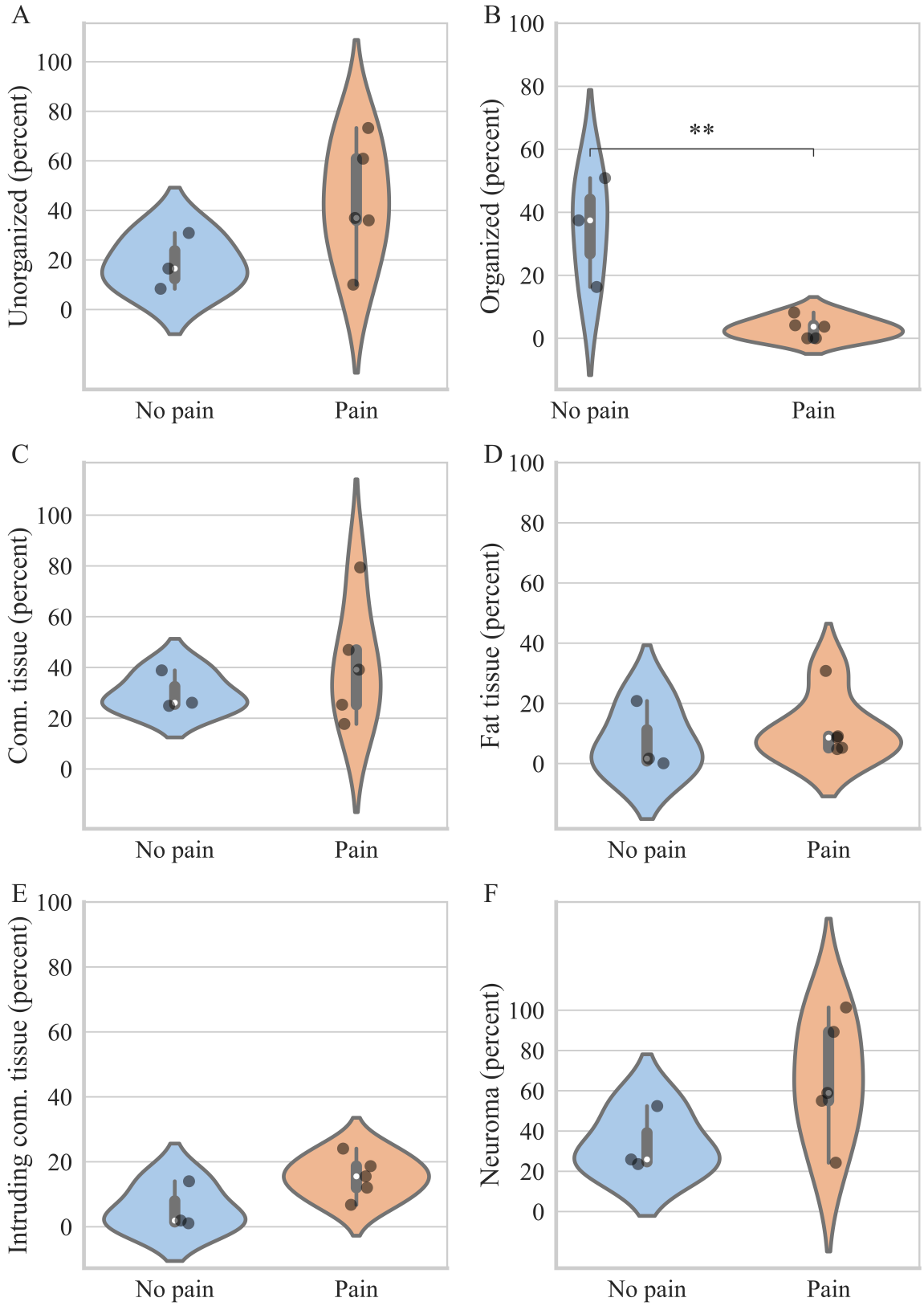

Figure 63 - Relative: Pain vs. no pain. (A) Amount of unorganized nervous tissue, **(B)** organized nervous tissue, and **(C)** connective tissue, **(D)** Fat tissue, **(E)** connective tissue intruding unorganized nervous tissue, and **(F)** Neuroma (unorganized nervous tissue including connective tissue) in relation to the nerve's size of patients with and without neuroma pain. Each violin plot represents the density of data points at different values. The white dot marks the median, and the black box represents the interquartile range (IQR). Two asterisks (**) indicate $p < 0.01$.

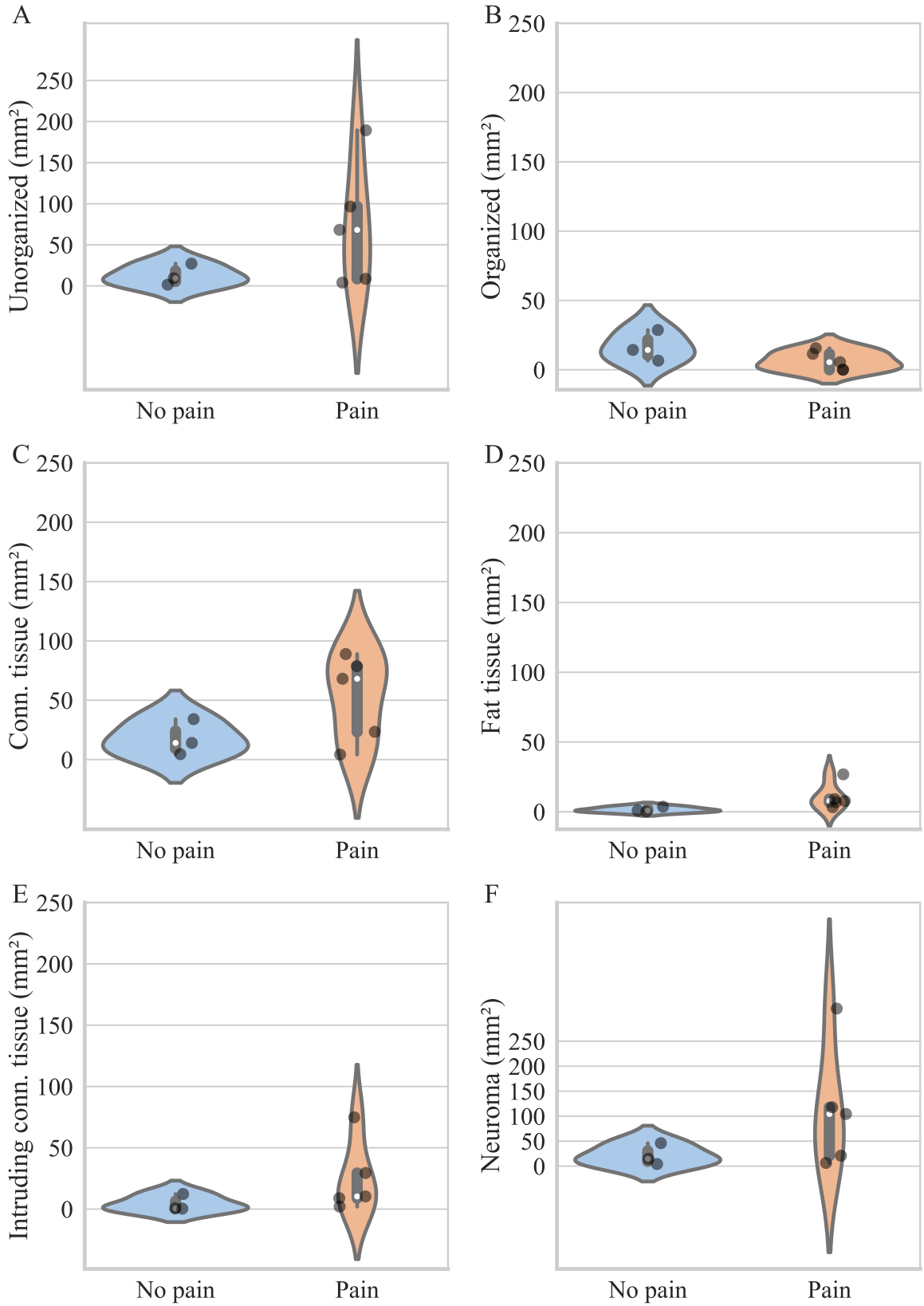

Figure 64 - Absolute: Pain vs. no pain. **(A)** Total area of unorganized nervous tissue, **(B)** organized nervous tissue, and **(C)** connective tissue, **(D)** fat tissue, **(E)** connective tissue intruding unorganized nervous tissue, and **(F)** Neuroma (unorganized nervous tissue including connective tissue) in relation to the nerve's size of patients with and without neuroma pain. Each violin plot represents the density of data points at different values. The white dot marks the median, and the black box represents the interquartile range (IQR)..

3.2.3.6 Percentual amount of organized nervous tissue negatively correlates with the pain level.

The normalized deviation between organized and unorganized nervous tissue is significantly higher in patients suffering from neuroma-pain (p = 0.006) (Figure 66), even if the nerves are the same size (Figure 65).

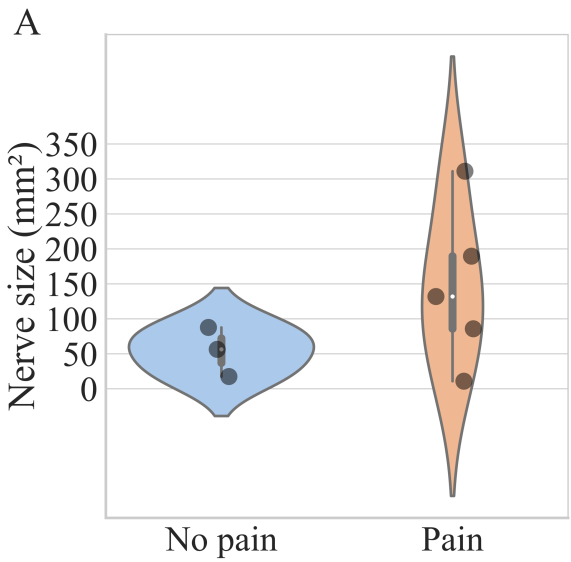

Figure 65 - Absolute nerve size of patients with and without neuroma pain. Each violin plot represents the density of data points at different values. The white dot marks the median, and the black box represents the interquartile range (IQR).

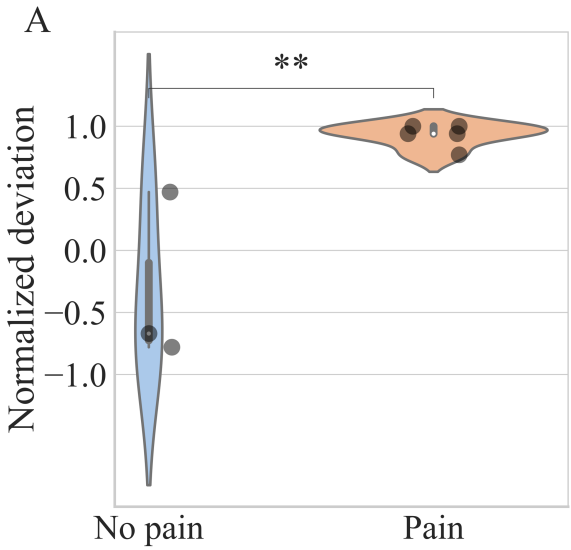

Figure 66- Normalized deviation between the organized and unorganized fascicles in patients with and without neuroma pain. Each violin plot represents the density of data points at different values. The white dot marks the median, and the black box represents the interquartile range (IQR). Two asterisks (**) indicate p < 0.01.

Additionally, the data show a significant negative correlation between the reported pain level reported (NRS) and the relative amount of organized nervous tissue (p = 1.2e-04), and a positive correlation with the normalized deviation between organized and unorganized nervous tissue (p = 1.2e-04) and reported pain level. No significant correlation between the reported pain level and the relative amount of unorganized nervous tissue was found, neither in the absolute area, nor in the absolute area of organized nervous tissue (Figure 67).

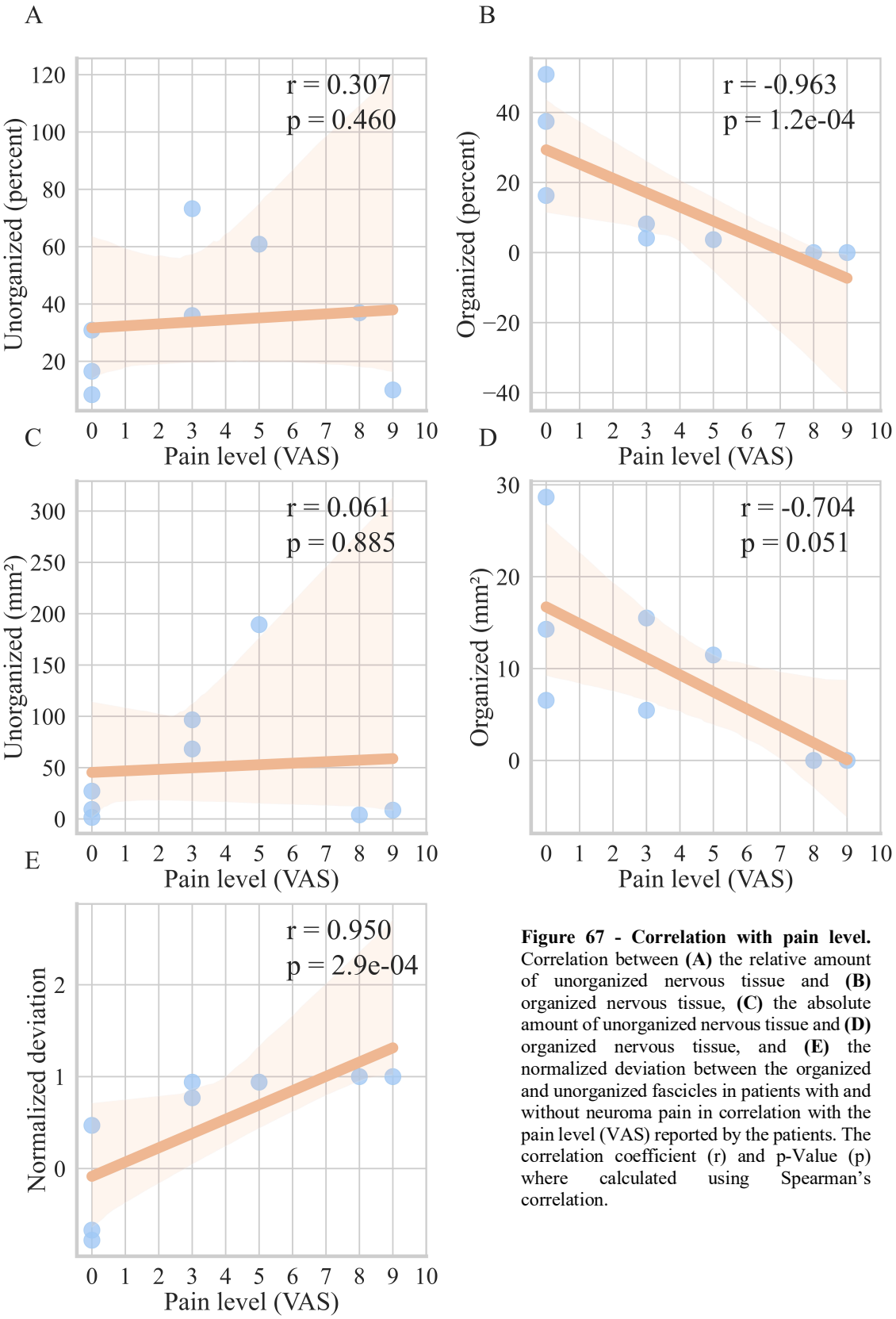

Figure 67 - Correlation with pain level. Correlation between **(A)** the relative amount of unorganized nervous tissue and **(B)** organized nervous tissue, **(C)** the absolute amount of unorganized nervous tissue and **(D)** organized nervous tissue, and **(E)** the normalized deviation between the organized and unorganized fascicles in patients with and without neuroma pain in correlation with the pain level (VAS) reported by the patients. The correlation coefficient (r) and p-Value (p) where calculated using Spearman's correlation.

4 DISCUSSION

Sensorimotor disruption is shown to take a key role in neuropathic pain [217]. Its restoration or substitution is therefore thought to be a key aspect of successful rehabilitation and pain management [173].

Due to the lack of a comprehensive map of the vibrotactile capacity on the healthy upper limb, during the present study, several experiments were conducted using the current state of the art technology on able-body participants to target the aforementioned capacity. Once a baseline was set, to further investigate the effect of hypoalgesia during rehabilitation, further mapping of the upper limb after a distal (amputation) and proximal (BPI) nerve injury was performed.

Targeting the effects proximally from the injury site and to address the reason why a neuroma is painful or not, several aspects of the neuroma were investigated. On the one side, the amount of inflammation markers and myelin. On the other side, a novel method was employed to visually segment transections obtained from patients with and without a diagnosed neuroma, differentiating between patients who do and do not experience neuroma pain.

4.1 VIBROTACTILE SENSATION ON THE HEALTHY ARM

In harmony with the findings of Neely et al. [32] who reported no gender-specific differences during vibrotactile threshold measurements in the arm region, this discussion does not differentiate between the participant's gender.

To evaluate the psychometric properties, tasks were used that quantified sensation threshold, just noticeable difference, and perception of dynamically changing vibrotactile stimuli. The arm-shoulder region was subdivided into six dermatomes and three segments - the lower arm, the upper arm, and the shoulder region, with each segment being stimulated proximally and distally. Assessing the arm's capacity towards vibration, the decision was made to vary the amplitude of stimulation while maintaining a fixed frequency at 230 Hz. Due to the coupling effect between frequency and amplitude, the amplitude will change when the tactor operates outside its optimal frequency range (200-250 Hz for the C2 tactors) even though the frequency remains unaffected when the amplitude is modulated [203]. Dideriksen [195] demonstrates that electrotactile outperforms C2 tactors at frequencies lower than 200 Hz. However, as the

frequency of the vibrotactile approaches the optimal range, the performance of both stimulation modalities becomes similar.

The data presented indicate that the receptors exhibit a similar response to relative changes in vibration stimuli, meaning changes that are normalized to the perceivable range of stimulation – both the Weber fraction and the number of distinct intervals were the same across all arm-shoulder region segments. Though, different arm segments did have distinct perceivable ranges of stimulation - the sensation threshold increased significantly from distal to proximal regions. The higher tracking error in the tracking task for the shoulder compared to the arm region might be due to the smaller perceivable stimulation range in the shoulder region (i.e., the higher sensation threshold), which leads to a reduced ability to accurately assess the magnitude of the error in the tracking task. Despite some variability, healthy individuals are capable of perceiving vibrations at 230 Hz with relatively low amplitudes (between 2-6%) in the arm and shoulder regions and can distinguish between two consecutive stimuli with amplitude differences of at least 20%. Two out of three performance measures in the compensatory tracking task were found to be independent of the arm location, indicating that the ability to perceive dynamic stimuli is only minimally affected by the location of stimulation.

This discussion assumes that Pacini corpuscles are being targeted. Although the study design does not allow determining if there are differences between receptors since the results were not correlated with histological studies, the data suggest that the receptors activated by the vibration stimuli exhibit the same behavior across all locations, regardless of their structural entity.

4.1.1 The sensation of absolute values is location dependent.

The sensation threshold, which refers to the minimum energy level required for a stimulus to produce a sensation, was among the features of human sensory perception initially assessed [218]. This concept was pivotal to Fechner's psychophysics, and his integration of Weber's law produced the first psychophysical relationship ($S = k * \log(I)$) by measuring physical intensity using the absolute threshold as the unit [218]. Weber and Fechner utilized the method of limits to identify this threshold by adjusting the energy level until the observer shifted from "no sensation" to "yes, I perceive something". The minimum energy level needed for perception was one of the first quantifiable aspects of sensory function [205, 218] and was therefore used as first assessment.

It was found that vibration applied to the shoulder/neck region needed to have a significantly higher vibration amplitude than the stimulation applied to the lower arm to be perceived. The selected vibrotactile stimulation frequency (230 Hz) mainly targets the Pacini corpuscles in the skin [19], and present findings might be explained by the fact that Pacini receptor density in the upper limb augments in the direction from the shoulder to the hand [183, 219, 220].

Studies on differences in receptor density between the ventral and dorsal sides of the arm-shoulder region are limited, as most research focuses on the hand, which has hairy skin on the dorsal side and glabrous skin on the ventral side [221, 222]. The arm is entirely covered in hairy skin, so significant differences in receptor density were not expected [223]. However, researchers found that sensation thresholds differ between the ventral and dorsal sides of the arm segments, with significant differences only in the lower arm and shoulder areas. The ventral side had a significantly lower sensation threshold in both segments, possibly due to differences in innervation or thicker muscle tissue covering the bones in the dorsal areas. In a study by Jacobs et al., they examined the effect of vibratory stimulation on the thumb and foot sole of prosthetic and normal limbs in amputees [224]. They found that bone-anchored prostheses provided better perception than socket prostheses, which rely on soft tissue support. Sensation thresholds in socket prostheses were 20% higher compared to healthy limbs, while sensation thresholds in bone-anchored prostheses were similar to control limbs. This result could explain why no significant differences were found in the upper arm, where ventral and dorsal muscle cover is similar.

All able-bodied participants could accurately identify the location of active vibrotactile units. The experiment showed that vibrotactors can be effectively distinguished at a distance of 61 mm. This finding is comparable to previously reported two-point discrimination ability in literature, which ranges from 30.7 mm to 42.4 mm in different arm regions (mid-posterior lower arm and lateral upper arm, respectively), indicating that vibrotactile localization perception is similar to two-point discrimination. [225].

4.1.2 The perception of relative changes is location independent.

The minimum amount of stimulus change needed to create a discernible difference in sensation is referred to as the just noticeable difference. Weber established that a constant fraction of the initial stimulus intensity must be added to attain a just noticeable difference in physical

stimulus intensity, expressed as Weber's law, $\frac{\Delta\Phi}{\Phi} = c$, which states that $\Delta\Phi$ represents the change in stimulus intensity necessary to reach a just noticeable difference, and c is the constant fraction of the initial stimulus intensity. Weber's law is a valuable tool for determining sensory discrimination, as it can be compared across various conditions and modalities and it has been previously used to asses sensation capacity on the arm [195].

In contrast to the ST, no significant differences in WF or NDI between any segments were found, whether comparing ventrally versus dorsally or individual segments. This is because the WF does not measure the absolute change of amplitude between two stimuli, but the relative one. Therefore, assuming that the same family of receptors is being activated over the whole arm-shoulder region, the WF and NDI are expected to be similar in every location. Present results suggest that the same types of receptors were activated at different sites of the investigated regions.

Previous studies show that the WF for vibration perception on the lower arm is in the range of 17% to 30%, which is consistent with the findings of a WF value of 20% across all locations in the arm-shoulder region at a 230 Hz stimulation frequency [226, 227]. Interestingly, the WF obtained on the fingertips using a similar setup and a frequency of 200 Hz was only about 18% lower than that of the lower arm, although the sensation threshold (ST) of the fingertip was about 63% lower than that of the lower arm [226]. This supports the claim that the sensation threshold decreases substantially more from proximal to distal on the whole limb, but the WF remains relatively consistent.

ST and WF measure different aspects of stimulation intensity perception. While the ST represents the minimum absolute value of stimulation intensity that can be detected, the WF measures the minimum relative change of stimulation intensity that can be perceived. Thus, the WF reflects the overall physiological functioning of receptors and their interaction with surrounding tissue, not just receptor density. Feedback reproduction in the healthy arm can calculate the required difference between two stimuli at all points based on the measurement of the ST at the desired points and the WF at one of these points. This is possible if all regions have the same skin and similar structure.

To test this claim, the ST was measured at various points and calculated the WF using the measured value at one point. The process was repeated for all WFs, resulting in a standard deviation of 0.31% and an absolute mean error of 0.44%. This error, which is approximately

2.2% of the average measured WF, is therefore acceptable. This method could be beneficial for feedback implementation, as calibration would only need to be done once if the frequency and amplitude target one receptor type. Stimulation could then be provided across the entire arm using the same relative signal.

4.1.3 Dynamic stimulation requires integrating the absolute and the relative amplitude.

When assessing the capability of the human arm to sense vibration targeting the design of a feedback interface, it is mandatory to not only investigate static, but also dynamic feedback, which assimilates the presented feedback in nature.

The Human Operator theory, also known as the Human-Machine System theory, was introduced by Ronald A. Hess in 1965 [228]. This theory describes how humans interact with machines and how these interactions can be optimized to achieve efficient and effective performance. According to it, the human operator can be seen as a component of a more extensive system, representing a dynamic entity that adapts to changes in the system and can influence its performance as a whole. Hess identified three main factors that influence the performance of the human operator: the characteristics of the task being performed, the characteristics of the machine or technology being used, and the characteristics of the operator themselves. These factors can be optimized to improve overall performance and efficiency. The concept is explained by Hess using the analogy of a human soldier performing a tracking task where they try to keep a moving target within the field of view of their gun. In this scenario, the input can be considered as the angular error between the target and the azimuth of the gun's view field. At the same time, the output control action is represented by a force acting on a simple gear mechanism. A mathematical transfer function is used to model the soldier as an inanimate servomechanism; therefore, the behavior is modeled as an active feedback control device using a transfer function defined by linear, constant-coefficient differential equations, with the main parameters being magnitude and phase delay [228].

During the compensatory tracking task, no significant differences between the arm regions were found. This outcome could potentially be explained by the fact that the delay of the sensory pathway was relatively small in comparison to other delays that were present in the control loop, such as motor delay and cognitive processing delay. Therefore, this delay failed to account for a substantial difference across different arm regions.

The mean distance was calculated from the site of stimulation on the lower arm to the spinal cord, which was 63 cm, from the upper arm it was 43 cm, and from the shoulder it was 13 cm for the able-bodied participants. As previously mentioned, Pacinian corpuscles are innervated by Aβ fibers with conduction velocities up to 70 m/s [229], implying a travel time of 8.96 ms from the stimulation site of the lower arm, 6.15 ms from the upper arm, and 1.8 ms from the shoulder/neck region. The observed times fall within the interquartile range of the delay for each site, so they do not account for differences in time delay, aligning with presented results. Therefore, it was concluded that the travel time of the stimuli, resulting from nerve conduction velocity, did not significantly impact the measured time delay. This also implies that the cognitive processing of stimuli and the delay in executing motor commands remain consistent, regardless of changes between stimulation regions.

In their study, Stepp et al. found that participants showed a significant improvement in performance within a single session, indicating a strong learning effect. However, the effect of the vibration site on performance was less pronounced [230]. A difference in average rectified error was found between stimulated regions, but the time delay did not depend on physiological reaction time. Rather, it depended on the user's ability to correctly classify the provided feedback and respond appropriately to it.

Similar to the experimental task in which the WF was calculated, it is possible that the subject was merely differentiating between two consecutive stimuli and deciding which one was stronger. Subsequently, a rectified error of 0 would imply that the user would have been able to distinguish between infinite NDIs. As all regions had the same NDIs, no significant differences were expected between them. Though, the tracking error was significantly higher in the shoulder compared to the upper arm. This could be explained by the subject using the previously mentioned mechanism of comparing subsequent stimulations to determine the sign of the trend of the error (i.e., to determine if the error is increasing/decreasing), but here, the subject also needed to know if the error is large or small (in absolute terms) to appropriately react. Therefore, the compensatory tracking task required a combination of skills, including the ability to differentiate between relative changes and identify the overall magnitude of the stimulation (its absolute value), similar to the sensation threshold. This second aspect may contribute to a deterioration in performance as one moves proximally. The correlation coefficient suggested a statistical trend (corrected p-value < 0.1) of worsening performance between the lower arm and the shoulder.

4.2 RELEVANCE OF THE SITE OF INJURY – THE SENSATION CAPACITY DOES NOT CHANGE PROXIMALLY FROM THE SITE OF INJURY AND DRASTICALLY DECREASES DISTALLY.

These results show that the observations on able-bodied subjects discussed in the previous chapters are applicable also to *transradial amputees* (*TR*). Namely, the two subject populations show no significant difference in any experiment or condition. As previously depicted, distally to the injury site, lost connections between sensory neurons and receptors, patients experience hypoalgesia or analgesia eliciting deafferentation pain [109]. However, during our experiment, the vibrotactile capacity of the upper arm of *TR* was only measured proximally from the injury site. Put differently, the amputation does not alter the ability to perceive vibration on the remaining limb. Moreover, comparing the segments between each other, no significant differences were found. If this is true, the level of amputation might have no impact either and the results presented could be extrapolated to other amputation levels (e.g., transcarpal, transhumeral).

In the shoulder/neck region, participants with a brachial plexus injury (*BPI*) do not defer much from the other two subject populations – the only exception is they exhibit somewhat higher shoulder ST in comparison to *AB*. However, most other parameters show that these participants perform significantly worse if the feedback is provided more distally compared to the other populations, getting worse from the *UA* to the *LA*. This goes in line with the participant's demographics, as all *brachial plexus injuries* resulted in a damage to the C5 or C6 roots, which innervate the upper trunk, without involving C3 and C4, responsible for the innervation of the shoulder/ neck region, leading to hypoalgesia and/or analgesia. After reconstruction surgery, if successful, the damaged nerves reinnervate from proximal to distal at a daily rate of about 1mm [231], explaining why the majority was not even able to successfully perceive any difference between two stimuli during the JND task.

Interestingly, *BPI* inter-subject performed least consistently comparing the three populations, which is visible in the high dispersion of the single measurement points in each boxplot and its significantly higher variance in comparison to *AB* in the ST measurements in every segment and in the WF and NDI on the *UA*. In contrast, the variance in the data obtained from *TR* does not differ from the one obtained from *AB* during these tasks. Differences in recovery stadium, performed surgeries, or severity of damage might be decisive factors determining the sensation capacity of the injured arm, and might be a reason for the high discrepancy in performance between these individuals.

4.3 PRACTICAL IMPLICATIONS FOR THE DESIGN OF VIBROTACTILE FEEDBACK MODALITIES

The lack of sensory feedback in modern prosthetic devices, both for upper and lower limbs, poses considerable challenges for amputees [181]. Sensory feedback plays a crucial role in an individual's perception and interaction with the environment, facilitating motor control, balance, and cognitive integration of limbs [197]. Upper-limb amputees report that the lack of sensory feedback hinders their ability to execute precise grip forces and fine manipulations [181]. Furthermore, the diminished physiological feedback to the central nervous system impairs the integration of the prosthesis into the individual's body schema, leading to poor embodiment and increased cognitive load during prosthesis usage [232, 233]. This results in reduced confidence in the prosthetic device and its acceptability [181, 234].

During the experiment, results that could have a significant impact on the design and evaluation of devices for vibrotactile stimulation of the upper limbs were obtained. On the healthy arm, the perception of the relative changes of the stimulation intensity was consistent across all arm regions. Moreover, the STs, although significantly different, were still relatively small compared to the overall amplitude range. None of the measured locations exhibited a ST greater than 6% of the maximal amplitude. These results have practical implications for the design of vibrotactors for the arm, as they could be of similar size and power, regardless of their location. This facilitates their optimized mechanical design, as it is not necessary to develop different sizes and power outputs for different locations on the arm. Furthermore, the delays measured during the compensatory tracking task revealed that the cognitive processing of the stimuli and the execution delay of motor commands are not significantly affected by the distance of the stimulation site to the spinal cord or its origin on the arm. This means that individuals can use feedback devices efficiently and with similar cognitive effort across all arm-shoulder dermatomes. Interestingly, if it is true, that present results can be extrapolated to all upper limb amputees, independent of their amputation level, they should all be able to perceive feedback with similar proficiency. Moreover, feedback systems for amputees could be displaced distally to the amputation without significant loss in their performance, which is a useful insight specifically in those cases where residual stump length and amputation level impose significant (space) limitations for embedding tactile interface in the prosthesis socket.

In contrast, the high inter-subject variability in sensation capacity of BPI subjects suggests that design of feedback systems for these individuals might be more challenging than for other subject populations included in this study. Namely, depending on their application, these

systems would need to be tailored specifically for every individual. Nevertheless, some generalization regarding application of feedback is still possible for *BPI*: the shoulder-neck region seems suitable in overall since the sensation capacity in it did not vary greatly (and is even significantly lower, than the one on the *UA* regarding ST) and it was largely comparable to *AB* and *TR* subjects.

A specific application scenario for this study could be vibrotactile feedback for upper-limb prostheses that communicates the prosthesis' grip force to the amputee by modulating the vibration intensity (e.g., the higher the intensity the higher the grip force [194]). Specifically, the enhanced use of an active myoelectric prosthesis in upper extremity amputees was associated with reduced phantom limb pain and reduced cortical reorganization in the homuncular organization of primary somatosensory (S1) and motor cortex (M1), in comparison to passive cosmetic prosthesis [165] The reduction in PLP correlated to the extent the user experienced that the discharged motor output of the prosthesis corresponds visually and functionally to the representations of the lost limb [165, 235, 236, 237, 238]. The new technology enabled the amputee to actively engage with the prosthetic limb through their sense of proprioception. This phenomenon is described by the term “embodiment” [235, 236, 239].

In this context, current results are promising for amputees as feedback can be delivered to various arm locations. This makes it possible to supply individuals with different amputation levels with feedback (for transradial amputees on the lower arm, for transhumeral amputates on the upper arm or on the shoulder). Since the overall implementations of the feedback and prosthetic systems are similar, and that amputees show no significant alteration in vibration sensation in comparison to able-bodies, the results suggest that both transhumeral and transradial prosthetic users may benefit from a similar proficiency level in perceiving and interpreting the feedback (i.e., the prosthesis grip force). To be more precise, the results suggest that individuals with transradial amputation may have an advantage in perceiving the actual amplitude of the prosthesis' grip force due to their lower ST in the lower arm. On the other hand, both transradial and transhumeral amputees should be able to perceive and quantify the relative changes in grip force (i.e., its relative increase or decrease from an arbitrary nominal value) since the WF was mostly invariant between the upper and lower arm. Nevertheless, this statement suggests that the difference in overall performance between the two subject groups is not likely to be significant or relevant in practical terms. This conclusion is drawn from the observation that both groups showed similar abilities in real-time interpretation of feedback

during the tracking task. This similarity indicates that the feedback interface, regardless of the specific arm region involved, plays a role in an overarching sensory-motor integration framework. This framework likely allows individuals to adapt and integrate sensory feedback effectively, regardless of minor differences in performance. This framework consisting of several intertwined layers, such as feedforward motor control, the control system, and the end-effector, which in combination with feedback ultimately decide the outcome of the user's actions. [170].

Another practical example relates to the therapeutic management of deafferentation pain, where mirror therapy has been widely used as a method of substituting the missing physiological feedback with visual one [138].

Sano et al. developed a virtual reality rehabilitation system in which the patients performed several reaching tasks using the virtual phantom limb in a mirror-therapy-based approach. Once the target was reached, all participants got auditory feedback representing the collision sound. Additionally, in one condition, subjects received tactile feedback to the fingertips of the intact hand and in another condition, no tactile feedback was provided. They found, that even in a small amount, tactile feedback to the contralateral side had a larger effect on the reduction of PLP than no feedback [240]. Again, the results suggest for amputees a wide range of possibilities to provide feedback as deafferentation pain therapy, also on the ipsilateral side and independent of amputation level. In contrast, after a plexus brachialis injury, effective therapeutic feedback would be limited to the shoulder/ neck region, as only there, sensation and inter-subject variance remains here in an acceptable margin.

In fact, as part of the BMBF-funded project “PROMPT”, in which the University Medical Center Göttingen works together with other universities and companies to combine VR-based mirror therapy with basic state-of-art vibrotactile feedback to treat deafferentation pain, presented results were used to design a setup to further develop feedback strategies and its implementation in VR. This feedback algorithm was translated into an easily understandable flowchart that was forwarded to the developers for implementation in the therapy hardware. This flowchart consisted of Input/Output tables of the feedback algorithm describing which different events (inputs) in the VR world are used to modulate the haptic stimulation parameters (outputs) defined based on the reported result. Additionally, on the hardware level, the sensation mapping was used to help finalize the feedback interface for amputees and BPI individuals, used in combination with VR, by providing specific positioning requirements for

the distinct patient populations. The developed feedback system layout allows somatotopic, high-bandwidth, and bilateral haptic mapping of events in the VR by using eight vibrotactile units placed on the affected and non-affected arm (four per arm; see Figure 68). In the case of BPI individuals, it was opted for a shoulder system, where feedback can be effectively provided to all patients. In contrast, for amputees, a more modular system was chosen, which is easy to adapt to the different amputation levels. As amputees do not significantly differ in vibration sensation on the arm compared to able-bodied, it was feasible to integrate this modularity without the need to modify the design or motors (Figure 69).

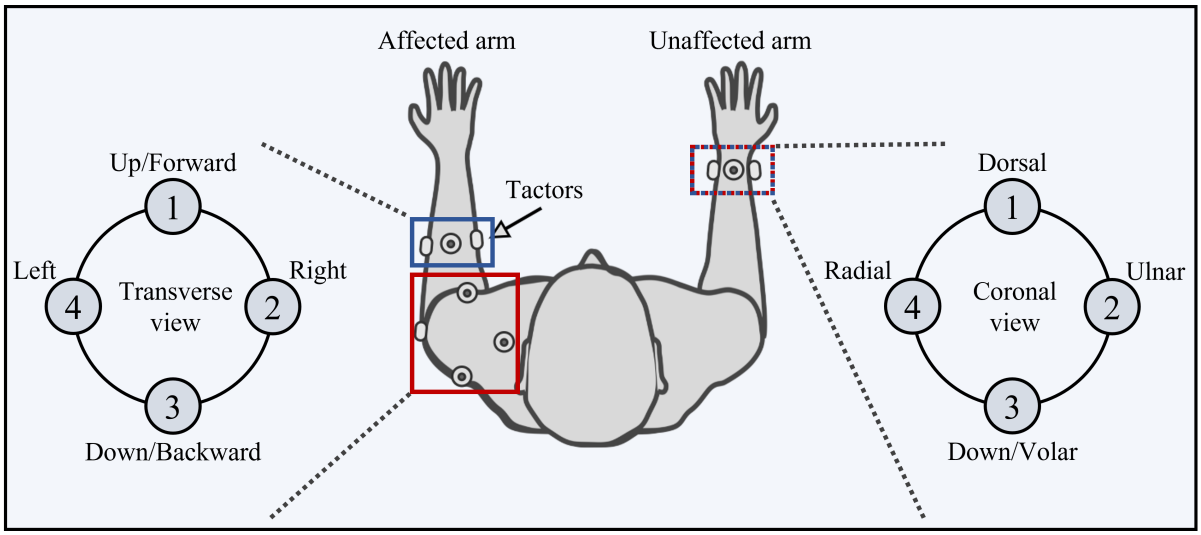

Figure 68 - Feedback system. The feedback system layout for both patient groups participating in the study: BPI (red) and amputees (blue). Note that, on the unaffected arm, the FS is placed on the same location for both subject groups.

Figure 69 - Feedback system. **(A)** depicts the feedback system for amputees consisting of a feedback system for **(B)** the healthy arm, and **(C)** the impaired arm. **(D)** shows the feedback system for BPI individual, in which feedback is provided to the shoulder and **(E)** healthy arm.

4.4 AUTOMATING NEUROMA ANALYSIS

During the analysis, it was ensured that all samples analyzed were cut in the same direction and free of extra-epineural tissue. Interestingly, unorganized nervous tissue was detected intruding muscle outside the nerve, which has been suggested as a factor in the development of intractable pathological pain [241]. However, as it was only observed in one patient and no correlations to pain were made.

During histological examinations of neuromas in this study, a detailed inspection of the samples unveiled that neuroma specimens might contain solely healthy fascicles, exclusively neuroma-associated minifascicles, or a combination of both. Consequently, further analyses were performed taking these observations into consideration.

After digitalization, to overcome the issue of overlapping absorption spectra, image analysis techniques can be used to deconvolve the stain signals and quantify the amount of each stain in the image. This process, called color deconvolution or stain separation, allows for the

accurate measurement of the staining intensity of different structures or proteins in an image [215].

Color deconvolution methods are based on mathematical algorithms that use the spectral characteristics of the stains to separate their signals. These algorithms consider the spectral overlap between the stains and the different absorption spectra of each stain. They use this information to estimate the concentration of each stain in the image [215].

Once channels are separated, various morphometric and photometric features can be measured, such as the size, shape, and intensity of specific structures as well as the co-localization of different stains, to generate quantitative data. Nonetheless, the overlapping spectral absorption of stains can pose a considerable challenge. Various approaches have been suggested to tackle this problem, such as employing color separation techniques or utilizing monochromatic dyes or narrow-band filters. Nevertheless, these methods have limitations. The color deconvolution algorithm presented by Ruifrok and Johnston in 2001 [216] overcomes these by using the information of all contributing colors, allowing for the separate presentation of stain components even if the stains show overlapping spectral absorption spectra as well as co-localization.

This method has become the prevailing standard and involves using the red, green, and blue (RGB) channels of color images to calculate the spatial distribution of the pure stain concentrations, resulting in "stain channels". It has gained widespread acceptance and has been incorporated into various commercial and open-source bio-imaging software packages.

Deconvolution was successfully performed on hematoxylin/ DAB-stainings. To be sure to correctly identify positive cells, in the case of macrophages and T-lymphocytes, positive DAB staining was filtered using a mask based on the position of the nuclei, therewith, it was ensured that random staining accumulation was excluded. These might influence the correct identification of positive cells, if for some reason, the nucleus is missing. However, this effect would affect all samples analyzed and the as a normal distribution.

Color deconvolution is a useful tool for the analysis of double-stainings, however, distinguishing between organized and unorganized tissue is an entirely new problem, for which separation several methods were tested. As a novel attempt, Hussein et al. [242] suggested an unsupervised classification method.

In recent years, image classification has been a core topic in computer vision and is the basis for various visual recognition fields such as object detection, segmentation, or tracking. Image analysis relies on the process of organizing and assigning labels to groups of pixels or vectors within an image according to particular criteria. Supervised and unsupervised classification are the primary techniques employed for this purpose in image classification.

Unsupervised classification is a fully automated process that does not require training data. Through the application of a suitable algorithm, the defined features of an image are systematically identified during the image processing phase. The classification methods used in unsupervised classification are image clustering and pattern recognition. A common example of unsupervised classification is K-means clustering.

K-means clustering, originally introduced by MacQueen in 1967 [243], building upon the work of [244], is a vector quantization technique designed to divide n data points into k distinct clusters. In this method, each data point is assigned to the cluster whose mean is the closest, acting as a representative of the cluster. Consequently, the data space is partitioned into Voronoi cells.

As a computationally light algorithm, it was tested on neuroma samples. However, similarly to deconvolution, it was rapidly noticed that unsupervised classification is not of help, as the problem of both tissue qualities stained the same remained, therefore suggesting that the differentiation of organized and unorganized nervous tissue is an entirely morphological problem.

To overcome this problem, supervised classification was employed, which is a type of machine learning technique that uses labeled data to classify new data points into predefined categories. There are several supervised classification algorithms available, such as Maximum Likelihood Classifiers [245], Support Vector Machines [246], Random Forests [247], and Neural Networks [248], among others. As the dataset is relatively small and the tissue to separate is very similar, a classifier able to handle high-dimensional feature spaces and which is less prone to overfitting was needed, leaving a Random Forest classifier as the way to go.

Random Forest (RF) is a machine learning algorithm that belongs to the ensemble learning techniques. The idea behind ensemble learning is to train multiple models on different subsets of data and combine their predictions to improve the overall accuracy of the model. Before going into detail with the actual RF, it is important to mention some basic characteristics of its subunits: the decision trees. In a decision tree, each internal node corresponds to a feature (or

attribute), while the branches represent decision rules, and every leaf node symbolizes an outcome. The resulting structure resembles a flowchart and is often used to represent decision-making processes visually. The initial node is commonly referred to as the root node, which partitions the tree based on attribute values through recursive partitioning. As a result of this tree-based visualization method, decision trees are generally considered easy to interpret and comprehend. Classification using RF involves an assembly of decision trees, where each tree is created from a random portion of the training dataset and a random subset of input features. The algorithm then takes a majority vote of the trees to predict the class label of a new data point [249].

The key advantages of Random Forest Classification are its ability to handle high-dimensional data, its robustness to noise and outliers, and its ability to handle missing values. RF also provides a measure of variable importance, which indicates how much each input feature contributes to the overall classification accuracy. Additionally, as the input features are calculated out of the pixels using a Gaussian pyramid approach, it is able to introduce qualities about the morphology of the segmented image, and not solely the color.

While decision trees are prone to overfitting because they can closely fit all the examples in the training data, the use of many decision trees in a RF reduces this risk. This is because averaging over uncorrelated trees decreases the overall variance and prediction error of the classifier [249], reducing the danger of mislabeling qualities which are under-represented in the image.

The segmentation results were visually verified and approved by the department of neuropathology of the University Medical Center Göttingen. However, the possibility to implement the designed methodology for other studies and different tissues suggested further testing with the resulting models.

All models achieved high accuracy, F1-score, precision, and recall scores above 0.95, which is indicative of their ability to correctly identify and distinguish between different tissue types (Figure 46).

It is worth noting that no pixel was labeled as “unorganized nervous tissue” when applying a model trained on an image with unorganized nervous tissue to an image without unorganized nervous tissue. This methodology could therefore provide a fast initial tissue segmentation, facilitating the neuropathologist’s work.

Due to the high computational costs, the images were reduced to 10% of their original size before training the models and performing segmentation. The comparison of segmentation results on a small chunk between unmodified images and the reduced image suggests that this reduction did not significantly impact the model's performance. This finding further supports the fact that a neuroma is not a cellular phenomenon but a rather macroscopic diagnosis, in which the different interactions of adjacent tissues.

The results demonstrate the efficacy of the employed methodology for the given use-case. Nevertheless, to enhance the model's performance and enable a single model to segment various images, further investigation into feature engineering techniques, hyperparameter optimization, or alternative algorithms may prove beneficial.

Najdavi and her group used convolutional neural network model approach to predict areas of various tissue components, such as normal epithelium, neutrophil-infiltrated epithelium, and granulation tissue of H&E-stained whole slide images of mucosal biopsies [250]. Similarly, Dhaliwal et al. used a combination of Random Forest classification and similarity network fusion to identify a short list of features, which reliably distinguish ulcerative colitis from colonic Crohn disease [251].

Supervised image segmentation algorithms hold great potential for further applications in the study and diagnosis of neurological disorders, which may ultimately contribute to improved patient outcomes. Future research may focus on the integration of these models with other imaging modalities and the development of more efficient training strategies to further enhance their performance.

4.5 NEUROINFLAMMATION IN NEUROMA PAIN

Proximally to the injury site, if reinnervation fails, a neuroma forms. Inside the neuroma, the axons are surrounded by an abnormal myelin sheath that exhibits variable degrees of thickening, resulting in several phenomena that alter the electrophysiological properties of axons. This further leads to nociceptive sensitization and, under prolonged activity, hyperalgesia and/or allodynia. Excessive inflammation is thought to play a pivotal role in this sensitization and may be implicated in both the initiation and the maintenance of persistent pain. After PNI, macrophages and T-lymphocytes are recruited to the site of injury. Recruited infiltrating macrophages join resident macrophages and, together with Schwann cells, participate in the phagocytosis of degenerating axons and myelin sheaths. In addition to this

function, macrophages secrete various pro-inflammatory cytokines, chemokines, and lipid mediators [252]. Inflammation, commencing as a natural response to injury, is universally present in patients after PNI, but not all individuals with a neuroma suffer from neuroma pain, arguing against a causal relationship between inflammation and neuroma pain. The incursion of collagen and myofibroblasts, instigating mechanical irritation and increasing the neuroma's dimensions, is due to inflammation, the driving factor behind this intrusion [102, 103, 104, 105, 106].

Wagstaff et al. [253] used electron microscopy-based cell counts and revealed that the number of Schwann cells in mouse sciatic nerves increases about 2.5 times compared to uninjured nerves two weeks after injury, remaining similar at one and 1.5 months. To assess modification in Schwann cells in our samples, a histological quantification was performed. However, no differences between either neuroma and control patients, or between patients with and without neuroma pain, were found in the normalized area. Yet, this goes in line with the results presented by Siironen in 1994 [254]. Using S100 to identify Schwann cells in injured rat sciatic nerves, they showed a 3-4 times increase at one to two weeks, with little change at 1.5 months, additionally reporting a significant decrease between 1.5 and two months. Nonetheless, since S100 levels decrease after injury, these figures, as well as the here presented results, might overemphasize the reduction in Schwann cell numbers. As stated, the literature agrees that several kinds of inflammatory cells are involved in neuropathic pain and symptoms as hyperalgesia and allodynia. T-lymphocytes, for example, infiltrate the dorsal root ganglia (DRG) and release pro-algesic mediators leading to mechanical allodynia [255]. Similarly, the density of macrophages increases in the DRG one week after nerve transection and remains elevated for at least three months, releasing pro-inflammatory mediators [256], sensitizing and stimulating nociceptors. However, in the present results, no differences were detected regarding the number of macrophages, nor T-lymphocytes between controls and neuroma patients or between patients suffering and patients not suffering from neuroma pain in the normalized density. A reason might be, that these cells did contribute to maintain prolonged inflammation, but this led secondarily to mechanisms in the neuroma leading to mechanical irritation and neuroma pain, like the intrusion of collagen and myofibroblasts [102, 103, 104, 105, 106]. Consequently, macrophages and T-lymphocytes do not necessarily need to be present in persistent neuroma pain.

4.6 NEUROMA MORPHOLOGY AND REMAINING HEALTHY NERVOUS TISSUE

As none of the previously investigated pro-inflammatory aspects explains differences between painful and non-pain-full neuroma in the patient population included, morphological aspects of neuroma were analyzed, taking a special look into the normalized deviation between organized and unorganized nervous tissue. For this purpose, a Random Forest Algorithm was employed to visually segment transactions obtained from patients with and without a diagnosed neuroma. The generated masks were then used to describe the nerves' morphology quantitatively.

4.6.1 The amount of connective tissue is not increased in the neuroma.

While the primary feature of a neuroma is the proliferation of nervous tissue, the involvement of connective tissue in the formation of neuromas is not entirely clear. Several studies report an increase in the amount in connective tissue in the neuroma. Yet, present results show no differences between either the relative ($p = 0.515$) or absolute amount ($p = 0.066$) of connective tissue. Dömer et al. report an increase of connective tissue in neuromas [257]. However, this study does not provide a direct comparison between patients with and without neuromas, but between the distal and proximal parts of neuromas. Interestingly, Kim et al. showed that the amount of connective tissue proliferation depends on the surgery performed during nerve repair in rats, which might account for the present findings [258]. Furthermore, the medians and IQRs show that the neuroma group tends to have larger values than the control group (controls: 3.9 [3.6]mm^2; neuroma: 28.1 [38.8]mm^2). This tendency suggests that there might be a difference between the two populations, but the statistical test did not find it significant enough to confirm as indicated by the IQRs. It might be worth performing a proper power calculation to define the proper sample size, as this could help to detect a statistically significant difference if one exists.

Connective tissue is partially responsible for the mechanical irritation in neuromas [102, 103, 104, 105, 106], even though it is probably due to its proximity to the axons, rather than to its overall amount. However, as there are no differences between patients reporting, or not reporting pain, it is neither the amount itself nor the amount “entrapped” by unorganized nervous tissue. Therefore, it is not the determinant factor in answering the question of why some neuromas are painful and some are not.

4.6.2 The relative amount of fat tissue is decreased in neuromas.

The results show significant differences between control nerves and those with a neuroma regarding the relative amount of fat tissue. While this is not typically considered a primary factor in the development of pain associated with the neuroma, it is suggested that changes in lipid metabolism may play a role in the development of nerve injury and nerve repair. Studies have found an increase in the levels of specific lipids, such as phosphatidylcholine, sphingomyelin, and ceramides in the injured nerve tissue, respectively, and that levels of ceramides were positively correlated with the severity of diabetic neuropathy. However, it is unclear if these lipid metabolism changes are specific to neuromas or if they are a general response to nerve injury. Interestingly, comparing the areas covered by fat tissue inside the nerves, it seems that the absolute amount does not differ between controls and patients. These findings, together with the fact that both populations do not present any difference in the total size of the nerve, lead to the conclusion that the amount of fat tissue is not increasing. However, the growing neuroma is causing the relative amount of the other tissue to diminish. More than energy stores, fat tissue can protect its surrounding tissue to a certain extent. Hanno Millesi, a renowned peripheral nerve surgeon, implemented the use of fat pads in nerve surgery. Millesi found that placing a free fat pad graft around a repaired nerve could help to prevent the development of postoperative neuromas and protect the nerve from external compressive forces [259]. The fat pad provides a cushioning effect around the nerve, isolating it from surrounding tissues and reducing the risk of neuroma formation and pain [260, 259]. Even if the measured fat tissue is inside and not around the nerve during the present study, it might contribute to certain protection of the fascicles. The higher pressure and reduced cushioning effect might evoke increased spontaneous afferent input to the spinal cord, even if the axon is appropriately functioning. This might have an increased effect on the unprotected nociceptive fibers, increasing peripheral and central sensitization.

However, there are no differences between patients with and without pain, so it is not the decisive factor in the aspect of whether the neuroma patient suffers from pain or not.

4.6.3 The proportion of organized nervous tissue negatively correlates to the pain level.

Interestingly, during the study of inflammation-related cells, significance can be detected in several observations if the normalized deviation of organized and unorganized nervous tissue is applied to the density/area of the investigated cells. The observations indicate that this might be the determinant factor.

In fact, taking a deeper look into patients who do or do not report pain, it was found that neuroma patients suffering from pain displayed a higher amount of unorganized nervous tissue in relation to organized one and a significantly lower relative amount of organized nervous tissue. This result is supported after analyzing the absolute size of the area covered by each tissue. It was discovered that all tissues cover similar areas, and only the area covered by organized nervous tissues is significantly higher in patients who reported no neuroma-related pain.

Additionally, the obtained parameters were used to establish a correlation between pain level and morphological criteria. Here, no significant correlation between either the relative or the absolute amount of identified morphological criteria and pain level were found. Interestingly, the absolute and relative amount of organized nervous tissue and the normalized deviation between organized and unorganized nervous tissue significantly correlate with pain level.

An explanation for the observed phenomenon might rely on the Gate Control Theory of Pain [88], which suggests that pain perception is modulated by the interplay between pain-inhibiting and pain-facilitating impulses in the nervous system. Following this theory, after a peripheral nerve injury, organized nervous tissue can help maintain the integrity of sensory information and prevent chronic pain by transmitting accurate information about tissue damage to the central nervous system. By contrast, when the number of organized nervous tissue is reduced, the transmission of aberrant information may become more prevalent, leading to increased sensitivity to pain and the development of chronic pain.

If the ratio between nociceptive and non-nociceptive fibers in nerves and fascicles, which is highly variable [261], was maintained in neuromas, the Gate Control Theory would not explain the correlation between organized nervous tissue and neuroma pain. However, it was shown that unmyelinated C- and thin Aδ-fibers are predominant in neuromas [143, 262] (some studies suggesting a massive predominance of unmyelinated fibers by 20:1 [143]). The increase in the proportion of unmyelinated fibers is caused by the upregulation of neurotrophic factors during nerve regeneration like neuron growth factor (NFG), which promote the regeneration of these types of fibers [263]. Therefore, a higher relative amount of unorganized nervous tissue would highly increase the proportion of nociceptive signals to the dorsal horn and at the same time, decrease the amount of counteracting signals from myelinated non-nociceptive fibers.

In fact, the Gate Control Theory does not specifically address whether the non-nociceptive signals must be from actual sensory receptors or if they can be aberrant signals. However, it is

plausible that any signal activating the non-nociceptive fibers, whether from a sensory receptor or an aberrant source, could potentially modulate the gate mechanism and influence the perception of pain.

Furthermore, transcutaneous electrical nerve stimulation (TENS) [134] is a treatment modality that is often used to provide pain relief by stimulating non-nociceptive fibers. This is performed by applying short current pulses (50-200μs) at a high frequency (50-100Hz), taking advantage of the relatively lower threshold of Aβ-fibers [264]. TENS has been the subject of numerous studies, and its effectiveness in pain relief can be seen as evidence supporting the Gate Control Theory [265]. Although not explicitly designed to investigate aberrant signals, it indirectly suggests that non-nociceptive signals from various sources, including those generated by TENS, can modulate pain perception.

These factors might counteract sensitization and help prevent the chronification of neuropathic neuroma pain.

5 LIMITATIONS OF THE STUDY

During the assessment of vibration sensation in the arms of able-bodied, transradial amputees, and BPI participants, the variability between individual BPI participants was often significantly higher than in the other groups. This could be attributed to the unique recovery rate and pathology of each participant, making the interpretation and discussion of the results highly individualized.

Furthermore, no significant differences were found between the sensation capacity on the arm of transradial amputees and able-bodies. However, in contrast to what was found on the healthy arm, transradial amputees show no significant differences between the lower arm and the shoulder, nor between the ventral and dorsal sites. This might be explained by the low number of patients that participated in the study.

The healthy participants were asked to move the joystick during the tracking task with the stimulated arm, whereas BPI and transradial amputees used the healthy, unstimulated arm. However, as the control interface used was a modified joystick with removed spring, excessive contraction of the forearm muscles (e.g., moving the wrist too much) would have resulted in a poor execution of the task, which would have been noticed by the experimenter. Therefore, it is assumable that moving the arm while stimulating does not influence the perception.

During the vibrotactile experiments, the frequency is not modulated. Therefore, other frequencies are not investigated. In vibrotactile devices, the frequency and amplitude are coupled in the sense that, although the user can change both parameters independently, the reproducibility of the amplitude at different frequencies is not guaranteed. Put differently, while the frequency will remain unaffected when amplitude is modulated, the amplitude will change when frequency is modulated. More specifically, when used outside the optimal frequency range, which is around 200-250Hz, the amplitude of the tactor will drop. Only within the optimal frequency range the tactor can deliver full stimulation power, thus the name “the resonant frequency”. Outside this range, the tactor will not be able to achieve its peak performance. Therefore, the frequency and amplitude are intrinsically coupled, although they can be modulated independently. In general, there is no vibrotactile technology available on the market that avoids this kind of coupling effect between the frequency and the amplitude. An option would be to use electrotactile stimulation instead of vibrotactile, because an electrotactile interface has no mechanical components and, unlike vibrotactile, can maintain

the same amplitude over a range of different frequencies. However, this was not feasible during the present study, as its extensive and sometimes painful use during rehabilitation therapies in both patient groups might psychologically modify its perception.

Pacini corpuscles might adapt if the stimulation is too continuous. To avoid this, during the first experiment, regarding the sensation threshold, the applied vibration increased in amplitude over time, starting from 0%. The experiment was stopped as soon as the participant was able to feel the stimulation, therewith preventing adaptation. Additionally, each stimulation lasted for 1.25s and was followed by 0.5s break before the amplitude was increased. This way, the continuous vibration, which is probably the greatest contributor to adaptation was avoided. During the second experiment, regarding the just noticeable difference, breaks of 1s between two stimulations of 0.5s were applied. Again, in this way, the continuous vibration was effectively avoided. Additionally, the use of a (constant) lower amplitude as the base signal and the (decreasing) higher amplitude as the test signal to deliver as little stimulation as possible further avoided adaptation (doing it other way around - higher stimuli as the base, lower stimuli as the test - would result in higher chance for adaptation). The nature of the last experiment (the compensatory tracking task) did not allow any specific measures to be implemented to mitigate the adaptation effect. However, any worsening was measured in the participants' performance across consecutive trials. Additionally, the participants had a break of 1 to 2 min after each trial and the stimulation amplitude range was limited to [sensation threshold + 15% of the intensity range, sensation threshold + 90% of the intensity range].

Bias during neuroma surgery are inevitable, as surgeons are aware of the patient's diagnosis. This knowledge may result in subtle differences in the amount of nerve tissue removed, depending on whether the surgery was specifically indicated for neuroma-related pain or if the neuroma was discovered incidentally during another procedure. However, since only the distal part of the neuroma was analyzed, this bias should not significantly impact the study results.

During automatic cell detection after deconvolution, it is not feasible to check every single portion of an image for correct labeling and only aleatory checks were performed. However, the benefit of automatic detection also includes that, unlike during visual counting, the way of measuring and the ranges used remain the same for every chunk. Therefore, as normalized values were used during comparisons, errors in the individual count should not have any effect on the relative difference between populations.

Similarly, during image segmentation, it is not feasible to check every pixel for correct labeling. However, also here, miss labeling of single pixels is inevitable during manual segmentation, with the addition that during manual analysis, the personal features used might vary every day. In contrast, during automatic segmentation, the features leading to miss-labeling remain constant for every pixel and relative differences between populations should not be affected.

Pain experiences can vary greatly from person to person and there is no pain-measurement with fully foundation and science needs to rely on pain questionnaires. Taking this into account and after discussions with pain experts, VAS-scale levels below level three were set to zero to avoid including patients misinterpreting other pain sources as neuroma pain. However, the results of the correlations remained the same (results not shown).

Each neuroma is examined at a single time point, and numerous factors can influence its development. Consequently, the comparison is not between neuromas of the same age or growth conditions, and this limitation is not considered in the discussion.

6 CONCLUSION AND OUTLOOK

The data presented in this study offers insights into the role of peripheral nerve injuries (PNI) in sensory changes, particularly in relation to vibrotactile sensation capacity of the upper extremity. It was found that the healthy arm and shoulder region can perceive vibrations at 230Hz at relatively low amplitudes (in the range of 2-6%) and differentiate between two sequential stimulations if their amplitudes differ by 20%. Moreover, the compensatory tracking task indicates that the ability of subjects to perceive dynamically changing stimuli is independent of the location of the stimulus.

Remarkably, when vibration is applied proximally from the site of injury in transradial amputees, the response is similar to that observed in a healthy arm. In fact, all outcomes were the same in all tests, suggesting that receptors proximal to the injury are not adversely affected. In contrast, the sensation capacity distal to the site of injury is substantially reduced. Patients with a brachial plexus injury were less able to perceive absolute amplitude and relative differences between stimuli than able-bodied participants. In other words, the sensation threshold is higher, and the Weber fraction and the number of distinct intervals is lower in the lower arm and upper arm. The sensation is only comparable to that of a healthy arm when vibrotactile feedback is applied to the shoulder/neck region. This finding is further supported by the fact that, among BPI participants, the sensation capacity significantly deteriorates when moving distally from the site of injury.

Interestingly, no participants reported pain or displayed better perception when applying the feedback proximal to the injury site. This finding suggests that the provided feedback at selected parameters does not elicit negative symptoms such as hyperalgesia or allodynia, thereby supporting vibration as a viable option for feedback.

In overall, the experiments provide elementary insights regarding the vibrotactile sensation capacity of the upper extremity. Since vibrotactile displays are the State-of-Art in a wide array of applications, these results might contribute to their increased effectiveness, specially, in their implementation in prostheses and pain therapies.

Investigating neuromas, no increased amount of inflammation related cells was found. Inflammation is a key factor during the first weeks and months after injury. However, the main factor of pain might not be the presence of these cells, but their promotion of the sensitization of nociceptive neurons and the intrusion of fibrous tissue into the neuroma, provoking

entanglement between minifascicles and connective tissue, provoking increased mechanical stress. In contrast, the amount of remaining organized nervous tissue might have significant implications in pain. Through an inhibition mechanism in the dorsal horn, a certain proportion of signals from organized Aβ-fibers might counteract the increased firing of small nociceptive fibers and, therewith, counteract pain chronification.

These findings suggest that for the prevention of painful neuroma formation, it is key to promote the regeneration or maintenance of organized fascicles. Additionally, it could help clinicians identify patients who are at higher risk for developing painful neuromas, potentially guiding preemptive interventions.

In conclusion, after PNI, patients need to cope with several changes distally and proximally from the site of injury. Due to the superordinate factor of losing the connection between the peripheral receptors and the CNS, sensation capacity is drastically reduced distally from the site of injury, but fully maintained proximally from it. However, in case of a neuroma formation, local factors might be decisive in the presence of neuroma pain. Therefore, presented results might help to better understand neuropathic pain, the design of therapies, and its prevention.

7 BIBLIOGRAPHY

[1] M. Bear, B. Connors and M. A. Paradiso, Neuroscience: exploring the brain, enhanced edition: exploring the brain, Jones & Bartlett Learning, 2020.

[2] E. R. Kandel, J. H. Schwartz, T. M. Jessell, S. A. Siegelbaum and A. J. Hudspeth, "Principles of neural science, fifth editon," in *Principles of Neural Science*, McGraw-Hill Education, 2013.

[3] B. A. Barres, "The mystery and magic of glia: a perspective on their roles in health and disease," *Neuron,* vol. 60, p. 430–440, 2008.

[4] T. C. Südhof, "Towards an understanding of synapse formation," *Neuron,* vol. 100, p. 276–293, 2018.

[5] G. A. Thibodeau and K. T. Patton, Estructura y función del cuerpo humano, Elsevier, 2012.

[6] P. E. Ludwig, V. Reddy and M. Varacallo, "Neuroanatomy, Neurons," in *StatPearls [Internet]*, StatPearls Publishing, 2022.

[7] V. V. Banin and E. K. Gasymov, "Distribution of proteins in neural membranes as a factor of reabsorption of endoneural (interstitial) fluid," *Arkhiv Anatomii, Gistologii i Embriologii,* vol. 99, p. 47–54, 1990.

[8] H. S. Gasser and J. Erlanger, "The role played by the sizes of the constituent fibers of a nerve trunk in determining the form of its action potential wave," *American Journal of Physiology-Legacy Content,* vol. 80, p. 522–547, 1927.

[9] G. M. Manzano, L. M. P. Giuliano and J. A. M. Nóbrega, "A brief historical note on the classification of nerve fibers," *Arquivos de neuro-psiquiatria,* vol. 66, p. 117–119, 2008.

[10] I. Varga and B. Mravec, "Nerve fiber types," in *Nerves and nerve injuries*, Elsevier, 2015, p. 107–113.

[11] P. Kumar and N. R. Prabhakar, "Peripheral chemoreceptors: function and plasticity of the carotid body," *Comprehensive Physiology,* vol. 2, p. 141, 2012.

[12] R. N. Lemon, "Descending pathways in motor control," *Annu. Rev. Neurosci.,* vol. 31, p. 195–218, 2008.

[13] R. J. Morecraft, J. L. Louie, J. L. Herrick and K. S. Stilwell-Morecraft, "Cortical innervation of the facial nucleus in the non-human primate: a new interpretation of the effects of stroke and related subtotal brain trauma on the muscles of facial expression," *Brain,* vol. 124, p. 176–208, 2001.

[14] A. E. Dubin, A. Patapoutian and others, "Nociceptors: the sensors of the pain pathway," *The Journal of clinical investigation,* vol. 120, p. 3760–3772, 2010.

[15] B. L. Riemann and S. M. Lephart, "The sensorimotor system, part I: the physiologic basis of functional joint stability," *Journal of athletic training,* vol. 37, p. 71, 2002.

[16] S. Hecht, S. Shlaer and M. H. Pirenne, "Energy, quanta, and vision," *The Journal of general physiology,* vol. 25, p. 819–840, 1942.

[17] A. J. Hudspeth and P. G. Gillespie, "Pulling springs to tune transduction: adaptation by hair cells," *Neuron,* vol. 12, p. 1–9, 1994.

[18] I. Darian-Smith, "The sense of touch: performance and peripheral neural processes," *Sensory Processes,* 1984.

[19] A. E. Saddik, M. Orozco, M. Eid and J. Cha, "Human haptic perception," in *Haptics Technologies*, Springer, 2011, p. 45–66.

[20] K. O. Johnson, *The roles and functions of cutaneous mechanoreceptors,* vol. 11, 2001, p. 455–461.

[21] A. I. Basbaum, D. M. Bautista, G. Scherrer and D. Julius, "Cellular and molecular mechanisms of pain," *Cell,* vol. 139, p. 267–284, 2009.

[22] C. J. Woolf and Q. Ma, "Nociceptors—noxious stimulus detectors," *Neuron,* vol. 55, p. 353–364, 2007.

[23] H. J. Seddon, "A classification of nerve injuries," *British medical journal,* vol. 2, p. 237, 1942.

[24] M. G. Burnett and E. L. Zager, "Pathophysiology of peripheral nerve injury: a brief review," *Neurosurgical focus,* vol. 16, p. 1–7, 2004.

[25] S. Sunderland and K. C. Bradley, "Stress-strain phenomena in human peripheral nerve trunks," *Brain,* vol. 84, p. 102–119, 1961.

[26] S. Sunderland, "A classification of peripheral nerve injuries producing loss of function," *Brain,* vol. 74, p. 491–516, 1951.

[27] M. Asplund, M. Nilsson, A. Jacobsson and H. Von Holst, "Incidence of traumatic peripheral nerve injuries and amputations in Sweden between 1998 and 2006," *Neuroepidemiology,* vol. 32, p. 217–228, 2009.

[28] P. W. Nathan, "Effects on movement of surgical incisions into the human spinal cord," *Brain,* vol. 117, p. 337–346, 1994.

[29] T. S. Jensen and N. B. Finnerup, "Allodynia and hyperalgesia in neuropathic pain: clinical manifestations and mechanisms," *The Lancet Neurology,* vol. 13, p. 924–935, 2014.

[30] M. Costigan, J. Scholz and C. J. Woolf, "Neuropathic pain: a maladaptive response of the nervous system to damage," *Annual review of neuroscience,* vol. 32, p. 1–32, 2009.

[31] W. W. Campbell, "Evaluation and management of peripheral nerve injury," *Clinical neurophysiology,* vol. 119, p. 1951–1965, 2008.

[32] A. Citri and R. C. Malenka, "Synaptic plasticity: multiple forms, functions, and mechanisms," *Neuropsychopharmacology,* vol. 33, p. 18–41, 2008.

[33] E. R. Kandel, "The molecular biology of memory storage: a dialogue between genes and synapses," *Science,* vol. 294, p. 1030–1038, 2001.

[34] T. V. P. Bliss and G. L. Collingridge, "A synaptic model of memory: long-term potentiation in the hippocampus," *Nature,* vol. 361, p. 31–39, 1993.

[35] X. Navarro, M. Vivó and A. Valero-Cabré, "Neural plasticity after peripheral nerve injury and regeneration," *Progress in neurobiology,* vol. 82, p. 163–201, 2007.

[36] J. Sandkuhler, "Models and mechanisms of hyperalgesia and allodynia," *Physiological reviews,* vol. 89, p. 707–758, 2009.

[37] C. Antfolk, M. D'alonzo, B. Rosén, G. Lundborg, F. Sebelius and C. Cipriani, "Sensory feedback in upper limb prosthetics," *Expert review of medical devices,* vol. 10, p. 45–54, 2013.

[38] A. Valero-Cabré and X. Navarro, "H reflex restitution and facilitation after different types of peripheral nerve injury and repair," *Brain research,* vol. 919, p. 302–312, 2001.

[39] T. Gordon, N. Tyreman and M. A. Raji, "The basis for diminished functional recovery after delayed peripheral nerve repair," *Journal of Neuroscience,* vol. 31, p. 5325–5334, 2011.

[40] A. V. Waller, "XX. Experiments on the section of the glossopharyngeal and hypoglossal nerves of the frog, and observations of the alterations produced thereby in the structure of their primitive fibres," *Philosophical transactions of the Royal society of London,* p. 423–429, 1850.

[41] A. L. Dellon, S. E. Mackinnon and A. Pestronk, "Implantation of sensory nerve into muscle: preliminary clinical and experimental observations on neuroma formation," *Annals of plastic surgery,* vol. 12, p. 30–40, 1984.

[42] O. A. R. Sulaiman and T. Gordon, "Role of chronic Schwann cell denervation in poor functional recovery after nerve injuries and experimental strategies to combat it," *Neurosurgery,* vol. 65, p. A105–A114, 2009.

[43] C. A. von Hehn, R. Baron and C. J. Woolf, "Deconstructing the neuropathic pain phenotype to reveal neural mechanisms," *Neuron,* vol. 73, p. 638–652, 2012.

[44] H. Flor, T. Elbert, S. Knecht, C. Wienbruch, C. Pantev, N. Birbaumers, W. Larbig and E. Taub, "Phantom-limb pain as a perceptual correlate of cortical reorganization following arm amputation," *Nature,* vol. 375, p. 482, 1995.

[45] M. Lotze, H. Flor, W. Grodd, W. Larbig and N. Birbaumer, "Phantom movements and pain An fMRI study in upper limb amputees," *Brain,* vol. 124, p. 2268–2277, 2001.

[46] Z. Sun, W. Wei, H. Liu, J. Ma, M. Hu and H. Huang, "Acute Response of Neurons: An early event of neuronal cell death after facial nerve injury," *World neurosurgery,* vol. 109, p. e252–e257, 2018.

[47] J. Arvidsson, J. Ygge and G. Grant, "Cell loss in lumbar dorsal root ganglia and transganglionic degeneration after sciatic nerve resection in the rat," *Brain research,* vol. 373, p. 15–21, 1986.

[48] T. X. Hoang, J. H. Nieto, N. J. K. Tillakaratne and L. A. Havton, "Autonomic and motor neuron death is progressive and parallel in a lumbosacral ventral root avulsion model of cauda equina injury," *Journal of Comparative Neurology,* vol. 467, p. 477–486, 2003.

[49] P. Dubovỳ, I. Klusáková, I. Hradilová-Svíženská, V. Brázda, M. Kohoutková and M. Joukal, "A conditioning sciatic nerve lesion triggers a pro-regenerative state in primary sensory neurons also of dorsal root ganglia non-associated with the damaged nerve," *Frontiers in Cellular Neuroscience,* vol. 13, p. 11, 2019.

[50] X.-J. Kang, Y.-N. Chi, W. Chen, F.-Y. Liu, S. Cui, F.-F. Liao, J. Cai and Y. Wan, "Increased expression of CaV3. 2 T-type calcium channels in damaged DRG neurons contributes to neuropathic pain in rats with spared nerve injury," *Molecular pain,* vol. 14, p. 1744806918765808, 2018.

[51] J. Qin, J.-C. Wu, Q.-H. Wang, S.-L. Zhou, S.-S. Mao and C. Yao, "Transcription factor networks involved in cell death in the dorsal root ganglia following peripheral nerve injury," *Neural regeneration research,* vol. 13, p. 1622, 2018.

[52] E. J. Huang and L. F. Reichardt, "Neurotrophins: roles in neuronal development and function," *Annual review of neuroscience,* vol. 24, p. 677–736, 2001.

[53] J. Qiu, D. Cai and M. T. Filbin, "Glial inhibition of nerve regeneration in the mature mammalian CNS," *Glia,* vol. 29, p. 166–174, 2000.

[54] K. K. Park, K. Liu, Y. Hu, P. D. Smith, C. Wang, B. Cai, B. Xu, L. Connolly, I. Kramvis, M. Sahin and others, "Promoting axon regeneration in the adult CNS by modulation of the PTEN/mTOR pathway," *Science,* vol. 322, p. 963–966, 2008.

[55] S. Wu, B. Marie Lutz, X. Miao, L. Liang, K. Mo, Y.-J. Chang, P. Du, P. Soteropoulos, B. Tian, A. G. Kaufman and others, "Dorsal root ganglion transcriptome analysis following peripheral nerve injury in mice," *Molecular pain,* vol. 12, p. 1744806916629048, 2016.

[56] M. P. Jankowski, S. L. McIlwrath, X. Jing, P. K. Cornuet, K. M. Salerno, H. R. Koerber and K. M. Albers, "Sox11 transcription factor modulates peripheral nerve regeneration in adult mice," *Brain research,* vol. 1256, p. 43–54, 2009.

[57] P. Topilko, S. Schneider-Maunoury, G. Levi, A. Baron-Van Evercooren, A. B. Y. Chennoufi, T. Seitanidou, C. Babinet and P. Charnay, "Krox-20 controls myelination in the peripheral nervous system," *Nature,* vol. 371, p. 796, 1994.

[58] J. C. Elfar, J. A. Jacobson, J. E. Puzas, R. N. Rosier and M. J. Zuscik, "Erythropoietin accelerates functional recovery after peripheral nerve injury," *The Journal of bone and joint surgery. American volume,* vol. 90, p. 1644, 2008.

[59] H. Funakoshi, J. Frisén, G. Barbany, T. Timmusk, O. Zachrisson, V. M. Verge and H. Persson, "Differential expression of mRNAs for neurotrophins and their receptors after axotomy of the sciatic nerve.," *The Journal of cell biology,* vol. 123, p. 455–465, 1993.

[60] R. G. Pellegrino and P. S. Spencer, "Schwann cell mitosis in response to regenerating peripheral axons in vivo," *Brain research,* vol. 341, p. 16–25, 1985.

[61] D. B. Parkinson, A. Bhaskaran, P. Arthur-Farraj, L. A. Noon, A. Woodhoo, A. C. Lloyd, M. L. Feltri, L. Wrabetz, A. Behrens, R. Mirsky and others, "c-Jun is a negative regulator of myelination," *The Journal of cell biology,* vol. 181, p. 625–637, 2008.

[62] F. Reichert, A. Saada and S. Rotshenker, "Peripheral nerve injury induces Schwann cells to express two macrophage phenotypes: phagocytosis and the galactose-specific lectin MAC-2," *Journal of Neuroscience,* vol. 14, p. 3231–3245, 1994.

[63] W. Brück, "The role of macrophages in Wallerian degeneration," *Brain pathology,* vol. 7, p. 741–752, 1997.

[64] P. Chen, X. Piao and P. Bonaldo, "Role of macrophages in Wallerian degeneration and axonal regeneration after peripheral nerve injury," *Acta neuropathologica,* vol. 130, p. 605–618, 2015.

[65] T. Gordon and A. W. English, "Strategies to promote peripheral nerve regeneration: electrical stimulation and/or exercise," *European Journal of Neuroscience,* vol. 43, p. 336–350, 2016.

[66] T. Gordon, "Peripheral nerve regeneration and muscle reinnervation," *International journal of molecular sciences,* vol. 21, p. 8652, 2020.

[67] D. W. Zochodne and D. Levy, "Nitric oxide in damage, disease and repair of the peripheral nervous system.," *Cellular and molecular biology (Noisy-le-Grand, France),* vol. 51, p. 255–267, 2005.

[68] E. R. Lunn, M. C. Brown and V. H. Perry, "The pattern of axonal degeneration in the peripheral nervous system varies with different types of lesion," *Neuroscience,* vol. 35, p. 157–165, 1990.

[69] M. A. L. Nicolelis, R. Lin, D. J. Woodward and J. K. Chapin, "Induction of immediate spatiotemporal changes in thalamic networks by peripheral block of ascending cutaneous information," *Nature,* vol. 361, p. 533–536, 1993.

[70] S. L. Florence, T. A. Hackett and F. Strata, "Thalamic and cortical contributions to neural plasticity after limb amputation," *Journal of neurophysiology,* vol. 83, p. 3154–3159, 2000.

[71] C. B. Mohanty, D. Bhat and B. Indira Devi, "Role of central plasticity in the outcome of peripheral nerve regeneration," *Neurosurgery,* vol. 77, p. 418–423, 2015.

[72] H. Flor, L. Nikolajsen and T. S. Jensen, "Phantom limb pain: a case of maladaptive CNS plasticity?," *Nature Reviews Neuroscience,* vol. 7, p. 873, 2006.

[73] B. D. Dickinson, C. A. Head, S. Gitlow and A. J. Osbahr III, "Maldynia: pathophysiology and management of neuropathic and maladaptive pain—a report of the AMA Council on Science and Public Health," *Pain Medicine,* vol. 11, p. 1635–1653, 2010.

[74] C. J. Woolf and R. J. Mannion, "Neuropathic pain: aetiology, symptoms, mechanisms, and management," *The lancet,* vol. 353, p. 1959–1964, 1999.

[75] R. P. Iacono, J. Linford and R. Sandyk, "Pain management after lower extremity amputation," *Neurosurgery,* vol. 20, p. 496–500, 1987.

[76] A. M. Kelahan and G. S. Doetsch, "Time-dependent changes in the functional organization of somatosensory cerebral cortex following digit amputation in adult raccoons," *Somatosensory research,* vol. 2, p. 49–81, 1984.

[77] M. M. Merzenich, J. H. Kaas, J. Wall, R. J. Nelson, M. Sur and D. Felleman, "Topographic reorganization of somatosensory cortical areas 3b and 1 in adult monkeys following restricted deafferentation," *Neuroscience,* vol. 8, p. 33–55, 1983.

[78] D. D. Rasmusson, "Reorganization of raccoon somatosensory cortex following removal of the fifth digit," *Journal of Comparative Neurology,* vol. 205, p. 313–326, 1982.

[79] M. M. Merzenich, J. H. Kaas, J. T. Wall, M. Sur, R. J. Nelson and D. J. Felleman, "Progression of change following median nerve section in the cortical representation of the hand in areas 3b and 1 in adult owl and squirrel monkeys," *Neuroscience,* vol. 10, p. 639–665, 1983.

[80] D. Borsook, L. Becerra, S. Fishman, A. Edwards, C. L. Jennings, M. Stojanovic, L. Papinicolas, V. S. Ramachandran, R. G. Gonzalez and H. Breiter, "Acute plasticity in

the human somatosensory cortex following amputation," *Neuroreport,* vol. 9, p. 1013–1017, 1998.

[81] B.-B. Bao, D.-Q. Qu, H.-Y. Zhu, T. Gao and X.-Y. Zheng, "Brain remodeling after chronic median nerve compression in a rat model," *Neural regeneration research,* vol. 13, p. 704, 2018.

[82] H. Flor, "Remapping somatosensory cortex after injury.," *Advances in neurology,* vol. 93, p. 195–204, 2003.

[83] C. S. McCabe, R. C. Haigh, P. W. Halligan and D. R. Blake, "Simulating sensory–motor incongruence in healthy volunteers: implications for a cortical model of pain," *Rheumatology,* vol. 44, p. 509–516, 2005.

[84] M. M. Merzenich, R. J. Nelson, M. P. Stryker, M. S. Cynader, A. Schoppmann and J. M. Zook, "Somatosensory cortical map changes following digit amputation in adult monkeys," *Journal of comparative Neurology,* vol. 224, p. 591–605, 1984.

[85] K. L. Collins, H. G. Russell, P. J. Schumacher, K. E. Robinson-Freeman, E. C. O'Conor, K. D. Gibney, O. Yambem, R. W. Dykes, R. S. Waters and J. W. Tsao, "A review of current theories and treatments for phantom limb pain," *The Journal of clinical investigation,* vol. 128, p. 2168–2176, 2018.

[86] H. Merskey, "Clarifying definition of neuropathic pain," *Pain,* vol. 96, p. 408–409, 2002.

[87] M. S. Gold and G. F. Gebhart, "Nociceptor sensitization in pain pathogenesis," *Nature medicine,* vol. 16, p. 1248–1257, 2010.

[88] R. Melzack and P. D. Wall, "Pain Mechanisms: A New Theory: A gate control system modulates sensory input from the skin before it evokes pain perception and response.," *Science,* vol. 150, p. 971–979, 1965.

[89] R. C. Coghill, "Individual differences in the subjective experience of pain: new insights into mechanisms and models," *Headache: The Journal of Head and Face Pain,* vol. 50, p. 1531–1535, 2010.

[90] A. I. Basbaum, "Basic mechanisms," *Pain Management Secrets E-Book,* p. 19, 2009.

[91] R. H. Dworkin, M. Backonja, M. C. Rowbotham, R. R. Allen, C. R. Argoff, G. J. Bennett, M. C. Bushnell, J. T. Farrar, B. S. Galer, J. A. Haythornthwaite and others, "Advances in neuropathic pain: diagnosis, mechanisms, and treatment recommendations," *Archives of neurology,* vol. 60, p. 1524–1534, 2003.

[92] T. S. Jensen, R. Baron, M. Haanpää, E. Kalso, J. D. Loeser, A. S. C. Rice and R.-D. Treede, "A new definition of neuropathic pain," *Pain,* vol. 152, p. 2204–2205, 2011.

[93] J. N. Campbell and R. A. Meyer, "Mechanisms of neuropathic pain," *Neuron,* vol. 52, p. 77–92, 2006.

[94] M. Devor, "Ectopic discharge in Aβ afferents as a source of neuropathic pain," *Experimental brain research,* vol. 196, p. 115–128, 2009.

[95] A. Latremoliere and C. J. Woolf, "Central sensitization: a generator of pain hypersensitivity by central neural plasticity," *The journal of pain,* vol. 10, p. 895–926, 2009.

[96] D. M. Ehde, J. M. Czerniecki, D. G. Smith, K. M. Campbell, W. T. Edwards, M. P. Jensen and L. R. Robinson, "Chronic phantom sensations, phantom pain, residual limb pain, and other regional pain after lower limb amputation," *Archives of physical medicine and rehabilitation,* vol. 81, p. 1039–1044, 2000.

[97] J. W. Griffin, M. V. Hogan, A. B. Chhabra and D. N. Deal, "Peripheral nerve repair and reconstruction," *Jbjs,* vol. 95, p. 2144–2151, 2013.

[98] S. G. Waxman, "The molecular pathophysiology of pain: abnormal expression of sodium channel genes and its contributions to hyperexcitability of primary sensory neurons," *Pain,* vol. 82, p. S133–S140, 1999.

[99] C. Yao, X. Zhou, B. Zhao, C. Sun, K. Poonit and H. Yan, "Treatments of traumatic neuropathic pain: a systematic review," *Oncotarget,* vol. 8, p. 57670, 2017.

[100] L. Leung and C. M. Cahill, "TNF-α and neuropathic pain-a review," *Journal of neuroinflammation,* vol. 7, p. 27, 2010.

[101] T. A. Wynn, "Common and unique mechanisms regulate fibrosis in various fibroproliferative diseases," *The Journal of clinical investigation,* vol. 117, p. 524–529, 2007.

[102] T. A. Wynn and T. R. Ramalingam, "Mechanisms of fibrosis: therapeutic translation for fibrotic disease," *Nature medicine,* vol. 18, p. 1028, 2012.

[103] H. Yan, W. Gao, Z. Pan, F. Zhang and C. Fan, "The expression of α-SMA in the painful traumatic neuroma: potential role in the pathobiology of neuropathic pain," *Journal of neurotrauma,* vol. 29, p. 2791–2797, 2012.

[104] G. Penkert and H. Fansa, "Trauma-Related Limb Nerve Lesions," in *Peripheral Nerve Lesions*, Springer, 2004, p. 69–104.

[105] T. Kretschmer, L. T. Happel, J. D. England, D. H. Nguyen, R. L. Tiel, R. W. Beuerman and D. G. Kline, "Clinical article accumulation of PN1 and PN3 sodium channels in painful human neuroma-evidence from immunocytochemistry," *Acta neurochirurgica,* vol. 144, p. 803–810, 2002.

[106] T. Kretschmer, J. D. England, L. T. Happel, Z. P. Liu, C. L. Thouron, D. H. Nguyen, R. W. Beuerman and D. G. Kline, "Ankyrin G and voltage gated sodium channels colocalize in human neuroma–key proteins of membrane remodeling after axonal injury," *Neuroscience letters,* vol. 323, p. 151–155, 2002.

[107] N. S. Buch, E. Qerama, N. B. Finnerup and L. Nikolajsen, "Neuromas and postamputation pain," *Pain,* vol. 161, p. 147–155, 2020.

[108] F. Pedregosa, G. Varoquaux, A. Gramfort, V. Michel, B. Thirion, O. Grisel, M. Blondel, P. Prettenhofer, R. Weiss, V. Dubourg and others, "Scikit-learn: Machine learning in Python," *the Journal of machine Learning research,* vol. 12, p. 2825–2830, 2011.

[109] C. Sherrington, "The integrative action of the nervous system.," *The Journal of Nervous and Mental Disease,* vol. 34, p. 801–802, 1907.

[110] V. S. Ramachandran and W. Hirstein, "The perception of phantom limbs. The DO Hebb lecture.," *Brain: a journal of neurology,* vol. 121, p. 1603–1630, 1998.

[111] A. Karl, N. Birbaumer, W. Lutzenberger, L. G. Cohen and H. Flor, "Reorganization of motor and somatosensory cortex in upper extremity amputees with phantom limb pain," *Journal of Neuroscience,* vol. 21, p. 3609–3618, 2001.

[112] T. Weiss, H. Koehler and I. Croy, "Pain and Reorganization after Amputation: Is Interoceptive Prediction a Key?," *The Neuroscientist,* p. 10738584221112591, 2022.

[113] T. R. Makin and H. Flor, "Brain (re) organisation following amputation: Implications for phantom limb pain," *Neuroimage,* vol. 218, p. 116943, 2020.

[114] N. B. Finnerup, N. Attal, S. Haroutounian, E. McNicol, R. Baron, R. H. Dworkin, I. Gilron, M. Haanpää, P. Hansson, T. S. Jensen and others, "Pharmacotherapy for neuropathic pain in adults: a systematic review and meta-analysis," *The Lancet Neurology,* vol. 14, p. 162–173, 2015.

[115] E. Kalso, D. J. Aldington and R. A. Moore, "Drugs for neuropathic pain," *Bmj,* vol. 347, 2013.

[116] H. Flor, "Phantom-limb pain: characteristics, causes, and treatment," *The Lancet Neurology,* vol. 1, p. 182–189, 2002.

[117] L. H. Poppler, R. P. Parikh, M. J. Bichanich, K. Rebehn, C. R. Bettlach, S. E. Mackinnon and A. M. Moore, "Surgical interventions for the treatment of painful neuroma: a comparative meta-analysis," *Pain,* vol. 159, p. 214, 2018.

[118] G. A. Dumanian, B. K. Potter, L. M. Mioton, J. H. Ko, J. E. Cheesborough, J. M. Souza, W. J. Ertl, S. M. Tintle, G. P. Nanos, I. L. Valerio and others, "Targeted muscle reinnervation treats neuroma and phantom pain in major limb amputees: a randomized clinical trial," *Annals of surgery,* vol. 270, p. 238–246, 2019.

[119] U. Eichenberger, F. Neff, G. Sveticic, S. Björgo, S. Petersen-Felix, L. Arendt-Nielsen and M. Curatolo, "Chronic phantom limb pain: the effects of calcitonin, ketamine, and their combination on pain and sensory thresholds," *Anesthesia & Analgesia,* vol. 106, p. 1265–1273, 2008.

[120] C. Maier, R. Dertwinkel, N. Mansourian, I. Hosbach, P. Schwenkreis, I. Senne, G. Skipka, M. Zenz and M. Tegenthoff, "Efficacy of the NMDA-receptor antagonist memantine in patients with chronic phantom limb pain–results of a randomized double-blinded, placebo-controlled trial," *Pain,* vol. 103, p. 277–283, 2003.

[121] B. J. Urban, R. D. France, E. K. Steinberger, D. L. Scott and A. A. Maltbie, "Long-term use of narcotic/antidepressant medication in the management of phantom limb pain," *Pain,* vol. 24, p. 191–196, 1986.

[122] P. Dharmshaktu, V. Tayal and B. S. Kalra, "Efficacy of antidepressants as analgesics: a review," *The Journal of Clinical Pharmacology,* vol. 52, p. 6–17, 2012.

[123] M. Bone, P. Critchley and D. J. Buggy, "Gabapentin in postamputation phantom limb pain: a randomized, double-blind, placebo-controlled, cross-over study," *Regional Anesthesia & Pain Medicine,* vol. 27, p. 481–486, 2002.

[124] W. S. Smith, G. Sung, S. Starkman, J. L. Saver, C. S. Kidwell, Y. P. Gobin, H. L. Lutsep, G. M. Nesbit, T. Grobelny, M. M. Rymer and others, "Safety and efficacy of mechanical embolectomy in acute ischemic stroke: results of the MERCI trial," *Stroke,* vol. 36, p. 1432–1438, 2005.

[125] K. U. Kern, H. Baust, W. Hofmann, R. Holzmüller, C. Maihöfner and M. L. Heskamp, "Capsaicin 8% cutaneous patches for phantom limb pain. Results from everyday practice (non-interventional study)," *Schmerz (Berlin, Germany),* vol. 28, p. 374–383, 2014.

[126] D. T. Cannon and Y. Wu, "Topical capsaicin as an adjuvant analgesic for the treatment of traumatic amputee neurogenic residual limb pain," *Archives of physical medicine and rehabilitation,* vol. 79, p. 591–593, 1998.

[127] C. Simanski, M. Lempa, G. Koch, T. Tiling and E. Neugebauer, "Therapy of phantom pain with salmon calcitonin and effect on postoperative patient satisfaction," *Der Chirurg; Zeitschrift fur Alle Gebiete der Operativen Medizen,* vol. 70, p. 674–681, 1999.

[128] H. Jaeger and C. Maier, "Calcitonin in phantom limb pain: a double-blind study," *Pain,* vol. 48, p. 21–27, 1992.

[129] E. Huse, W. Larbig, H. Flor and N. Birbaumer, "The effect of opioids on phantom limb pain and cortical reorganization," *Pain,* vol. 90, p. 47–55, 2001.

[130] L. Nikolajsen, N. B. Finnerup, S. Kramp, A.-S. Vimtrup, J. Keller and T. S. Jensen, "A randomized study of the effects of gabapentin on postamputation pain," *Anesthesiology: The Journal of the American Society of Anesthesiologists,* vol. 105, p. 1008–1015, 2006.

[131] L. Nikolajsen, H. Gottrup, A. G. D. Kristensen and T. S. Jensen, "Memantine (a N-methyl-D-aspartate receptor antagonist) in the treatment of neuropathic pain after

amputation or surgery: a randomized, double-blinded, cross-over study," *Anesthesia & Analgesia,* vol. 91, p. 960–966, 2000.

[132] M. P. Willand, E. Rosa, B. Michalski, J. J. Zhang, T. Gordon, M. Fahnestock and G. H. Borschel, "Electrical muscle stimulation elevates intramuscular BDNF and GDNF mRNA following peripheral nerve injury and repair in rats," *Neuroscience,* vol. 334, p. 93–104, 2016.

[133] C.-H. Kao, J.-J. J. Chen, Y.-M. Hsu, D.-T. Bau, C.-H. Yao and Y.-S. Chen, "High-frequency electrical stimulation can be a complementary therapy to promote nerve regeneration in diabetic rats," *PLoS One,* vol. 8, p. e79078, 2013.

[134] A. Heidland, G. Fazeli, A. Klassen, K. Sebekova, H. Hennemann, U. Bahner and B. Di Iorio, "Neuromuscular electrostimulation techniques: historical aspects and current possibilities in treatment of pain and muscle waisting," *Clin Nephrol,* vol. 79, p. S12–S23, 2013.

[135] A. E.-S. Allam, A. A. F. Khalil, B. A. Eltawab, W.-T. Wu and K.-V. Chang, "Ultrasound-guided intervention for treatment of trigeminal neuralgia: an updated review of anatomy and techniques," *Pain Research and Management,* vol. 2018, 2018.

[136] C. M. Brummett, E. K. Hong, A. M. Janda, F. S. Amodeo and R. Lydic, "Perineural dexmedetomidine added to ropivacaine for sciatic nerve block in rats prolongs the duration of analgesia by blocking the hyperpolarization-activated cation current," *The Journal of the American Society of Anesthesiologists,* vol. 115, p. 836–843, 2011.

[137] J. M. Climent, F. Mondéjar-Gómez, C. Rodríguez-Ruiz, I. Díaz-Llopis, D. Gómez-Gallego and P. Martín-Medina, "Treatment of Morton neuroma with botulinum toxin A: a pilot study," *Clinical drug investigation,* vol. 33, p. 497–503, 2013.

[138] V. S. Ramachandran and D. Rogers-Ramachandran, "Synaesthesia in phantom limbs induced with mirrors," *Proceedings of the Royal Society of London. Series B: Biological Sciences,* vol. 263, p. 377–386, 1996.

[139] M. E. H. Boeckstyns, A. I. Sørensen, J. F. Viñeta, B. Rosén, X. Navarro, S. J. Archibald, J. Valss-Solé, M. Moldovan and C. Krarup, "Collagen conduit versus microsurgical neurorrhaphy: 2-year follow-up of a prospective, blinded clinical and electrophysiological multicenter randomized, controlled trial," *The Journal of hand surgery,* vol. 38, p. 2405–2411, 2013.

[140] A. Hallgren, A. Björkman, A. Chemnitz and L. B. Dahlin, "Subjective outcome related to donor site morbidity after sural nerve graft harvesting: a survey in 41 patients," *BMC surgery,* vol. 13, p. 1–7, 2013.

[141] J. M. Souza, C. A. Purnell, J. E. Cheesborough, A. S. Kelikian and G. A. Dumanian, "Treatment of foot and ankle neuroma pain with processed nerve allografts," *Foot & Ankle International,* vol. 37, p. 1098–1105, 2016.

[142] K. Gorkisch, J. Boese-Landgraf and E. Vaubel, "Treatment and prevention of amputation neuromas in hand surgery.," *Plastic and reconstructive surgery,* vol. 73, p. 293–299, 1984.

[143] C. Lu, X. Sun, C. Wang, Y. Wang and J. Peng, "Mechanisms and treatment of painful neuromas," *Reviews in the Neurosciences,* vol. 29, p. 557–566, 2018.

[144] L. F. Domeshek, E. M. Krauss, A. K. Snyder-Warwick, O. Laurido-Soto, J. M. Hasak, G. B. Skolnick, C. B. Novak, A. M. Moore and S. E. Mackinnon, "Surgical treatment of neuromas improves patient-reported pain, depression, and quality of life," *Plastic and reconstructive surgery,* vol. 139, p. 407–418, 2017.

[145] J. González-Darder, J. Barberá, M. J. Abellán and A. Mora, "Centrocentral anastomosis in the prevention and treatment of painful terminal neuroma: an experimental study in the rat," *Journal of neurosurgery,* vol. 63, p. 754–758, 1985.

[146] C. Lidor, R. L. Hall and J. A. Nunley, "Centrocentral anastomosis with autologous nerve graft treatment of foot and ankle neuromas," *Foot & ankle international,* vol. 17, p. 85–88, 1996.

[147] M. Kon and J. J. Bloem, "The treatment of amputation neuromas in fingers with a centrocentral nerve union.," *Annals of plastic surgery,* vol. 18, p. 506–510, 1987.

[148] I. Ducic, A. N. Mesbahi, C. E. Attinger and K. Graw, "The role of peripheral nerve surgery in the treatment of chronic pain associated with amputation stumps," *Plastic and reconstructive surgery,* vol. 121, p. 908–914, 2008.

[149] M. V. Edds, "Prevention of nerve regeneration and neuroma formation by caps of synthetic resin," *Journal of Neurosurgery,* vol. 2, p. 507–509, 1945.

[150] M. Galeano, B. Manasseri, G. Risitano, S. Geuna, F. Di Scipio, P. La Rosa, G. Delia, F. S. D'Alcontres and M. R. Colonna, "A free vein graft cap influences neuroma formation after nerve transection," *Microsurgery: Official Journal of the International Microsurgical Society and the European Federation of Societies for Microsurgery,* vol. 29, p. 568–572, 2009.

[151] J. W. Tupper and D. M. Booth, "Treatment of painful neuromas of sensory nerves in the hand: a comparison of traditional and newer methods," *The Journal of hand surgery,* vol. 1, p. 144–151, 1976.

[152] I. C. Sando, M. K. Leach, S. L. Woo, J. D. Moon, P. S. Cederna, N. B. Langhals and M. G. Urbanchek, "Regenerative peripheral nerve interface for prostheses control: electrode comparison," *Journal of Reconstructive Microsurgery,* vol. 32, p. 194–199, 2016.

[153] J. B. Hijjawi, T. A. Kuiken, R. D. Lipschutz, L. A. Miller, K. A. Stubblefield and G. A. Dumanian, "Improved myoelectric prosthesis control accomplished using multiple nerve transfers," *Plastic and reconstructive surgery,* vol. 118, p. 1573–1578, 2006.

[154] T. A. Kuiken, G. A. Dumanian, R. D. Lipschutz, L. A. Miller and K. A. Stubblefield, "The use of targeted muscle reinnervation for improved myoelectric prosthesis control in a bilateral shoulder disarticulation amputee," *Prosthetics and orthotics international,* vol. 28, p. 245–253, 2004.

[155] T. A. Kuiken, L. A. Miller, R. D. Lipschutz, B. A. Lock, K. Stubblefield, P. D. Marasco, P. Zhou and G. A. Dumanian, "Targeted reinnervation for enhanced prosthetic arm function in a woman with a proximal amputation: a case study," *The Lancet,* vol. 369, p. 371–380, 2007.

[156] O. C. Aszmann, H. Dietl and M. Frey, "Selektive Nerventransfers zur verbesserten Steuerung myoelektrischer Armprothesen," *Handchirurgie\textperiodcentered Mikrochirurgie\textperiodcentered Plastische Chirurgie,* vol. 40, p. 60–65, 2008.

[157] A. D. Roche, H. Rehbaum, D. Farina and O. C. Aszmann, "Prosthetic myoelectric control strategies: a clinical perspective," *Current Surgery Reports,* vol. 2, p. 44, 2014.

[158] L. E. Miller, M. R. Longo and A. P. Saygin, "Tool morphology constrains the effects of tool use on body representations.," *Journal of Experimental Psychology: Human Perception and Performance,* vol. 40, p. 2143, 2014.

[159] J. M. Souza, J. E. Cheesborough, J. H. Ko, M. S. Cho, T. A. Kuiken and G. A. Dumanian, "Targeted muscle reinnervation: a novel approach to postamputation neuroma pain," *Clinical Orthopaedics and Related Research®,* vol. 472, p. 2984–2990, 2014.

[160] P. S. Kim, J. H. Ko, K. K. O'Shaughnessy, T. A. Kuiken, E. A. Pohlmeyer and G. A. Dumanian, "The effects of targeted muscle reinnervation on neuromas in a rabbit rectus abdominis flap model," *The Journal of hand surgery,* vol. 37, p. 1609–1616, 2012.

[161] A. J. Harris, "Cortical origin of pathological pain," *The Lancet,* vol. 354, no. 9188, pp. 1464-1466, 1999.

[162] J. Andoh, C. Milde, J. W. Tsao and H. Flor, "Cortical plasticity as a basis of phantom limb pain: Fact or fiction?," *Neuroscience,* vol. 387, p. 85–91, 2018.

[163] J. Andoh, C. Milde, M. Diers, R. Bekrater-Bodmann, J. Trojan, X. Fuchs, S. Becker, S. Desch, O. Meijer and H. Flor, "Assessment of cortical reorganization and preserved function in phantom limb pain: a methodological perspective," *arXiv preprint arXiv:1902.07268,* 2019.

[164] M. Ortiz-Catalan, R. A. Gumundsdóttir, M. B. Kristoffersen, A. Zepeda-Echavarria, K. Caine-Winterberger, K. Kulbacka-Ortiz, C. Widehammar, K. Eriksson, A. Stockselius, C. Ragnö and others, "Phantom motor execution facilitated by machine learning and augmented reality as treatment for phantom limb pain: a single group, clinical trial in patients with chronic intractable phantom limb pain," *The Lancet,* vol. 388, no. 10062, pp. 2885-2894, 2016.

[165] M. Lotze, W. Grodd, N. Birbaumer, M. Erb, E. Huse and H. Flor, "Does use of a myoelectric prosthesis prevent cortical reorganization and phantom limb pain?," *Nature neuroscience,* vol. 2, p. 501, 1999.

[166] S. Preißler, D. Thielemann, C. Dietrich, G. O. Hofmann, W. H. R. Miltner and T. Weiss, "Preliminary evidence for training-induced changes of morphology and phantom limb pain," *Frontiers in human neuroscience,* vol. 11, p. 319, 2017.

[167] A. Aternali and J. Katz, "Recent advances in understanding and managing phantom limb pain," *F1000Research,* vol. 8, 2019.

[168] P. D. Marasco, A. E. Schultz and T. A. Kuiken, "Sensory capacity of reinnervated skin after redirection of amputated upper limb nerves to the chest," *Brain,* vol. 132, p. 1441–1448, 2009.

[169] J. S. Hebert, J. L. Olson, M. J. Morhart, M. R. Dawson, P. D. Marasco, T. A. Kuiken and K. M. Chan, "Novel targeted sensory reinnervation technique to restore functional hand sensation after transhumeral amputation," *IEEE Transactions on Neural Systems and Rehabilitation Engineering,* vol. 22, p. 765–773, 2013.

[170] J. W. Sensinger and S. Dosen, "A review of sensory feedback in upper-limb prostheses from the perspective of human motor control," *Frontiers in neuroscience,* vol. 14, p. 345, 2020.

[171] G. S. Dhillon and K. W. Horch, "Direct neural sensory feedback and control of a prosthetic arm," *IEEE transactions on neural systems and rehabilitation engineering,* vol. 13, p. 468–472, 2005.

[172] C. Dietrich, K. Walter-Walsh, S. Preißler, G. O. Hofmann, O. W. Witte, W. H. R. Miltner and T. Weiss, "Sensory feedback prosthesis reduces phantom limb pain: proof of a principle," *Neuroscience letters,* vol. 507, p. 97–100, 2012.

[173] S. Raspopovic, M. Capogrosso, F. M. Petrini, M. Bonizzato, J. Rigosa, G. Di Pino, J. Carpaneto, M. Controzzi, T. Boretius, E. Fernandez and others, "Restoring natural sensory feedback in real-time bidirectional hand prostheses," *Science translational medicine,* vol. 6, p. 222ra19–222ra19, 2014.

[174] M. Markovic, H. Karnal, B. Graimann, D. Farina and S. Dosen, "GLIMPSE: Google Glass interface for sensory feedback in myoelectric hand prostheses," *Journal of neural engineering,* vol. 14, p. 036007, 2017.

[175] S. Dosen, M. Markovic, C. Hartmann and D. Farina, "Sensory feedback in prosthetics: a standardized test bench for closed-loop control," *IEEE Transactions on Neural Systems and Rehabilitation Engineering,* vol. 23, p. 267–276, 2014.

[176] M. A. Schweisfurth, M. Markovic, S. Dosen, F. Teich, B. Graimann and D. Farina, "Electrotactile EMG feedback improves the control of prosthesis grasping force," *Journal of neural engineering,* vol. 13, p. 056010, 2016.

[177] G. Rognini, F. M. Petrini, S. Raspopovic, G. Valle, G. Granata, I. Strauss, M. Solcà, J. Bello-Ruiz, B. Herbelin, R. Mange and others, "Multisensory bionic limb to achieve prosthesis embodiment and reduce distorted phantom limb perceptions," *Journal of Neurology, Neurosurgery & Psychiatry,* vol. 90, p. 833–836, 2019.

[178] F. M. Petrini, M. Bumbasirevic, G. Valle, V. Ilic, P. Mijović, P. Čvančara, F. Barberi, N. Katic, D. Bortolotti, D. Andreu and others, "Sensory feedback restoration in leg amputees improves walking speed, metabolic cost and phantom pain," *Nature medicine,* vol. 25, p. 1356–1363, 2019.

[179] T. R. Clites, M. J. Carty, J. B. Ullauri, M. E. Carney, L. M. Mooney, J.-F. Duval, S. S. Srinivasan and H. M. Herr, "Proprioception from a neurally controlled lower-extremity prosthesis," *Science Translational Medicine,* vol. 10, p. eaap8373, 2018.

[180] P. Svensson, U. Wijk, A. Björkman and C. Antfolk, "A review of invasive and non-invasive sensory feedback in upper limb prostheses," *Expert review of medical devices,* vol. 14, p. 439–447, 2017.

[181] E. Biddiss and T. Chau, "Upper-limb prosthetics: critical factors in device abandonment," *American journal of physical medicine & rehabilitation,* vol. 86, p. 977–987, 2007.

[182] S. Salminger, H. Stino, L. H. Pichler, C. Gstoettner, A. Sturma, J. A. Mayer, M. Szivak and O. C. Aszmann, "Current rates of prosthetic usage in upper-limb amputees–have innovations had an impact on device acceptance?," *Disability and Rehabilitation,* p. 1–12, 2020.

[183] R. S. Johansson and K. J. Cole, "Sensory-motor coordination during grasping and manipulative actions," *Current opinion in neurobiology,* vol. 2, p. 815–823, 1992.

[184] G. Lundborg and B. Rosen, "Sensory substitution in prosthetics," *Hand clinics,* vol. 17, p. 481–488, 2001.

[185] J. S. Schneider, S. G. Diamond and C. H. Markham, "Parkinson's disease: sensory and motor problems in arms and hands," *Neurology,* vol. 37, p. 951–951, 1987.

[186] S. F. Tyson, M. Hanley, J. Chillala, A. B. Selley and R. C. Tallis, "Sensory loss in hospital-admitted people with stroke: characteristics, associated factors, and relationship with function," *Neurorehabilitation and Neural Repair,* vol. 22, p. 166–172, 2008.

[187] T. H. H. Tung and S. E. Mackinnon, "Brachial plexus injuries," *Clinics in plastic surgery,* vol. 30, p. 269–287, 2003.

[188] M. L. Auld, R. N. Boyd, G. L. Moseley, R. S. Ware and L. M. Johnston, "Impact of tactile dysfunction on upper-limb motor performance in children with unilateral cerebral palsy," *Archives of physical medicine and rehabilitation,* vol. 93, p. 696–702, 2012.

[189] M. Botvinick and J. Cohen, "Rubber hands ‘feel’touch that eyes see," *Nature,* vol. 391, p. 756–756, 1998.

[190] H. H. Ehrsson, B. Rosén, A. Stockselius, C. Ragnö, P. Köhler and G. Lundborg, "Upper limb amputees can be induced to experience a rubber hand as their own," *Brain,* vol. 131, p. 3443–3452, 2008.

[191] R. H. Da-Silva, F. van Wijck, L. Shaw, H. Rodgers, M. Balaam, L. Brkic, T. Ploetz, D. Jackson, K. Ladha and C. I. Price, "Prompting arm activity after stroke: A clinical proof of concept study of wrist-worn accelerometers with a vibrating alert function," *Journal of Rehabilitation and Assistive Technologies Engineering,* vol. 5, p. 2055668318761524, 2018.

[192] E. Tanaka, W.-L. Lian, Y.-T. Liao, H. Yang, L.-N. Li, H.-H. Lee and M. Shimodozono, "Development of a Tele-Rehabilitation System Using an Upper Limb Assistive Device," *Journal of Robotics and Mechatronics,* vol. 33, p. 877–886, 2021.

[193] A. Orand, E. Erdal Aksoy, H. Miyasaka, C. Weeks Levy, X. Zhang and C. Menon, "Bilateral tactile feedback-enabled training for stroke survivors using microsoft kinecttm," *Sensors,* vol. 19, p. 3474, 2019.

[194] B. Stephens-Fripp, G. Alici and R. Mutlu, "A review of non-invasive sensory feedback methods for transradial prosthetic hands," *IEEE Access,* vol. 6, p. 6878–6899, 2018.

[195] J. Dideriksen, M. Markovic, S. Lemling, D. Farina and S. Dosen, "Electrotactile and vibrotactile feedback enable similar performance in psychometric tests and closed-loop control," *IEEE Transactions on Haptics,* vol. 15, p. 222–231, 2021.

[196] B. Stephens-Fripp, R. Mutlu and G. Alici, "Using vibration motors to create tactile apparent movement for transradial prosthetic sensory feedback," in *2018 7th IEEE International Conference on Biomedical Robotics and Biomechatronics (Biorob)*, 2018.

[197] P. D. Marasco, J. S. Hebert, J. W. Sensinger, C. E. Shell, J. S. Schofield, Z. C. Thumser, R. Nataraj, D. T. Beckler, M. R. Dawson, D. H. Blustein and others, "Illusory movement perception improves motor control for prosthetic hands," *Science translational medicine,* vol. 10, p. eaao6990, 2018.

[198] M. A. Wilke, C. Niethammer, B. Meyer, D. Farina and S. Dosen, "Psychometric characterization of incidental feedback sources during grasping with a hand prosthesis," *Journal of neuroengineering and rehabilitation,* vol. 16, p. 1–13, 2019.

[199] V. A. Shah, M. Casadio, R. A. Scheidt and L. A. Mrotek, "Spatial and temporal influences on discrimination of vibrotactile stimuli on the arm," *Experimental brain research,* vol. 237, p. 2075–2086, 2019.

[200] M. Guemann, S. Bouvier, C. Halgand, F. Paclet, L. Borrini, D. Ricard, E. Lapeyre, D. Cattaert and A. d. Rugy, "Effect of vibration characteristics and vibror arrangement on

the tactile perception of the upper arm in healthy subjects and upper limb amputees," *Journal of neuroengineering and rehabilitation,* vol. 16, p. 1–16, 2019.

[201] B. L. Chang, J. Mondshine, C. M. Fleury, C. E. Attinger and G. M. Kleiber, "Incidence and nerve distribution of symptomatic neuromas and phantom limb pain after below-knee amputation," *Plastic and Reconstructive Surgery,* vol. 149, p. 976–985, 2022.

[202] E. B. List, D. D. Krijgh, E. Martin and J. H. Coert, "Prevalence of residual limb pain and symptomatic neuromas after lower extremity amputation: a systematic review and meta-analysis," *Pain,* vol. 162, p. 1906–1913, 2021.

[203] Engineering Acoustics Inc, [Online]. Available: https://www.eaiinfo.com/product/c2/. [Accessed 20 08 2021].

[204] L. A. Pardo Jr, M. Markovic, A. F. Schilling, M. A. Wilke and J. Ernst, "Vibrotactile mapping of the upper extremity: Absolute perceived intensity is location-dependent; perception of relative changes is not," *Frontiers in Neuroscience,* vol. 16, 2022.

[205] E. H. Weber, "De Tactu (“Concerning Touch”)," *De Pulsu, Resorptione, Auditu, et Tactu. Annotationes Anatomicae et Physiologicae [Concerning pulse, respiration, hearing, and touch: Anatomical and physiological notes],* p. 44–174, 1834.

[206] D. McRuer and D. H. Weir, "Theory of manual vehicular control," *Ergonomics,* vol. 12, p. 599–633, 1969.

[207] C. M. Balch, L. B. Riley, Y. J. Bae, M. A. Salmeron, C. D. Platsoucas, A. Von Eschenbach and K. Itoh, "Patterns of human tumor-infiltrating lymphocytes in 120 human cancers," *Archives of Surgery,* vol. 125, p. 200–205, 1990.

[208] P. J. Austin, A. Wu and G. Moalem-Taylor, "Chronic constriction of the sciatic nerve and pain hypersensitivity testing in rats," *JoVE (Journal of Visualized Experiments),* p. e3393, 2012.

[209] J. Frisen, M. Risling and K. Fried, "Distribution and axonal relations of macrophages in a neuroma," *Neuroscience,* vol. 55, p. 1003–1013, 1993.

[210] D. B. Zimmer, E. H. Cornwall, A. Landar and W. Song, "The S100 protein family: history, function, and expression," *Brain research bulletin,* vol. 37, p. 417–429, 1995.

[211] A. Faroni, S. A. Mobasseri, P. J. Kingham and A. J. Reid, "Peripheral nerve regeneration: experimental strategies and future perspectives," *Advanced drug delivery reviews,* vol. 82, p. 160–167, 2015.

[212] V. Kazlouskaya, S. Malhotra, J. Lambe, M. H. Idriss, D. Elston and C. Andres, "The utility of elastic Verhoeff-Van Gieson staining in dermatopathology," *Journal of cutaneous pathology,* vol. 40, p. 211–225, 2013.

[213] A. C. Ruifrok, D. A. Johnston and others, "Quantification of histochemical staining by color deconvolution," *Analytical and quantitative cytology and histology,* vol. 23, p. 291–299, 2001.

[214] G. Bradski, "The openCV library.," *Dr. Dobb's Journal: Software Tools for the Professional Programmer,* vol. 25, p. 120–123, 2000.

[215] S. Van der Walt, J. L. Schönberger, J. Nunez-Iglesias, F. Boulogne, J. D. Warner, N. Yager, E. Gouillart and T. Yu, "scikit-image: image processing in Python," *PeerJ,* vol. 2, p. e453, 2014.

[216] M. Ojala and G. C. Garriga, "Permutation tests for studying classifier performance.," *Journal of machine learning research,* vol. 11, 2010.

[217] A. D. Vittersø, M. Halicka, G. Buckingham, M. J. Proulx and J. H. Bultitude, "The sensorimotor theory of pathological pain revisited," *Neuroscience & Biobehavioral Reviews,* p. 104735, 2022.

[218] G. T. Fechner, Elemente der psychophysik, vol. 2, Breitkopf u. Härtel, 1860.

[219] D. Quintero, "Properties of cutaneous mechanoreceptors in the human hand-related to touch sensation," 1984.

[220] W. Montagna, "The skin," *Scientific American,* vol. 212, no. 2, pp. 56-69, 1965.

[221] Y. Liu and H. Wang, "Peripheral nerve injury induced changes in the spinal cord and strategies to counteract/enhance the changes to promote nerve regeneration," *Neural Regeneration Research,* vol. 15, p. 189, 2020.

[222] L. Li, M. Rutlin, V. E. Abraira, C. Cassidy, L. Kus, S. Gong, M. P. Jankowski, W. Luo, N. Heintz, H. R. Koerber and others, "The functional organization of cutaneous low-threshold mechanosensory neurons," *Cell,* vol. 147, no. 7, pp. 1615-1627, 2011.

[223] A. Zimmerman, L. Bai and D. D. Ginty, "The gentle touch receptors of mammalian skin," *Science,* vol. 346, p. 950–954, 2014.

[224] R. Jacobs, R. Brånemark, K. Olmarker, B. Rydevik, D. v. Steenberghe and P.-I. Brånemark, "Evaluation of the psychophysical detection threshold level for vibrotactile and pressure stimulation of prosthetic limbs using bone anchorage or soft tissue support," *Prosthetics and orthotics international,* vol. 24, p. 133–142, 2000.

[225] M. F. Nolan, "Two-point discrimination assessment in the upper limb in young adult men and women," *Physical therapy,* vol. 62, p. 965–969, 1982.

[226] D. A. Mahns, N. M. Perkins, V. Sahai, L. Robinson and M. J. Rowe, "Vibrotactile frequency discrimination in human hairy skin," *Journal of neurophysiology,* vol. 95, p. 1442–1450, 2006.

[227] M. Rothenberg, R. T. Verrillo, S. A. Zahorian, M. L. Brachman and S. J. Bolanowski Jr, "Vibrotactile frequency for encoding a speech parameter," *The Journal of the Acoustical Society of America,* vol. 62, p. 1003–1012, 1977.

[228] R. A. Hess, "The human operator as an element in a control system with time varying dynamics," 1965.

[229] J. A. Montaño, P. Pérez-Piñera, O. García-Suárez, J. Cobo and J. A. Vega, "Development and neuronal dependence of cutaneous sensory nerve formations: Lessons from neurotrophins," *Microscopy research and technique,* vol. 73, p. 513–529, 2010.

[230] C. E. Stepp and Y. Matsuoka, "Object manipulation improvements due to single session training outweigh the differences among stimulation sites during vibrotactile feedback," *IEEE Transactions on Neural Systems and Rehabilitation Engineering,* vol. 19, p. 677–685, 2011.

[231] J. B. Recknor and S. K. Mallapragada, "Nerve regeneration: tissue engineering strategies," in *Tissue Engineering and Artificial Organs*, CRC Press, 2016, p. 759–780.

[232] R. Rackerby, S. Lukosch and D. Munro, "On Understanding and Measuring the Cognitive Load of Amputees for Rehabilitation and Prosthetic Development," *Archives of Rehabilitation Research and Clinical Translation,* p. 100216, 2022.

[233] S. Raspopovic, "Advancing limb neural prostheses," *Science,* vol. 370, p. 290–291, 2020.

[234] S. Raspopovic, G. Valle and F. M. Petrini, "Sensory feedback for limb prostheses in amputees," *Nature Materials,* vol. 20, p. 925–939, 2021.

[235] M. J. Giummarra, N. Georgiou-Karistianis, M. E. R. Nicholls, S. J. Gibson, M. Chou and J. L. Bradshaw, "Corporeal awareness and proprioceptive sense of the phantom," *British Journal of Psychology,* vol. 101, p. 791–808, 2010.

[236] M. J. Giummarra, S. J. Gibson, N. Georgiou-Karistianis and J. L. Bradshaw, *Mechanisms underlying embodiment, disembodiment and loss of embodiment,* vol. 32, 2008, p. 143–160.

[237] M. Diers, C. Christmann, C. Koeppe, M. Ruf and H. Flor, "Mirrored, imagined and executed movements differentially activate sensorimotor cortex in amputees with and without phantom limb pain," *PAIN®,* vol. 149, p. 296–304, 2010.

[238] J. Foell, R. Bekrater-Bodmann, M. Diers and H. Flor, "Mirror therapy for phantom limb pain: brain changes and the role of body representation," *European journal of pain,* vol. 18, p. 729–739, 2014.

[239] H. De Preester and M. Tsakiris, "Body-extension versus body-incorporation: Is there a need for a body-model?," *Phenomenology and the cognitive sciences,* vol. 8, p. 307–319, 2009.

[240] Y. Sano, N. Wake, A. Ichinose, M. Osumi, R. Oya, M. Sumitani, S.-i. Kumagaya and Y. Kuniyoshi, "Tactile feedback for relief of deafferentation pain using virtual reality system: a pilot study," *Journal of neuroengineering and rehabilitation,* vol. 13, no. 1, p. 61, 2016.

[241] M. W. Neumeister and J. N. Winters, "Neuroma," *Clinics in plastic surgery,* vol. 47, p. 279–283, 2020.

[242] Z. R. Hussein, A. I. Mahameed and J. A. Fadhil, "Distinguishing of Different Tissue Types Using K-Means Clustering of Color Segmentation," *Eastern-European Journal of Enterprise Technologies,* vol. 5, p. 113, 2021.

[243] J. MacQueen, "Classification and analysis of multivariate observations," in *5th Berkeley Symp. Math. Statist. Probability*, 1967.

[244] S. P. Lloyd and B. McMillan, "Linear least squares filtering and prediction of sampled signals," in *Proc. Symp. on Modern Network Synthesis*, 1955.

[245] R. A. Fisher, "On the mathematical foundations of theoretical statistics," *Philosophical transactions of the Royal Society of London. Series A, containing papers of a mathematical or physical character,* vol. 222, p. 309–368, 1922.

[246] O. Chapelle, P. Haffner and V. N. Vapnik, "Support vector machines for histogram-based image classification," *IEEE transactions on Neural Networks,* vol. 10, p. 1055–1064, 1999.

[247] L. Breiman, "Random forests," *Machine learning,* vol. 45, p. 5–32, 2001.

[248] W. S. McCulloch and W. Pitts, "A logical calculus of the ideas immanent in nervous activity," *The bulletin of mathematical biophysics,* vol. 5, p. 115–133, 1943.

[249] O. Sagi and L. Rokach, "Ensemble learning: A survey," *Wiley Interdisciplinary Reviews: Data Mining and Knowledge Discovery,* vol. 8, p. e1249, 2018.

[250] F. Najdawi, K. Sucipto, P. Mistry, S. Hennek, C. K. B. Jayson, M. Lin, D. Fahy, S. Kinsey, I. Wapinski, A. H. Beck and others, "Artificial intelligence enables quantitative assessment of ulcerative colitis histology," *Modern Pathology,* vol. 36, p. 100124, 2023.

[251] J. Dhaliwal, L. Erdman, E. Drysdale, F. Rinawi, J. Muir, T. D. Walters, I. Siddiqui, A. M. Griffiths and P. C. Church, "Accurate classification of pediatric colonic inflammatory bowel disease subtype using a random forest machine learning classifier," *Journal of Pediatric Gastroenterology and Nutrition,* vol. 72, p. 262–269, 2021.

[252] A. Ellis and D. L. H. Bennett, "Neuroinflammation and the generation of neuropathic pain," *British journal of anaesthesia,* vol. 111, p. 26–37, 2013.

[253] L. J. Wagstaff, J. A. Gomez-Sanchez, S. V. Fazal, G. W. Otto, A. M. Kilpatrick, K. Michael, L. Y. N. Wong, K. H. Ma, M. Turmaine, J. Svaren and others, "Failures of nerve regeneration caused by aging or chronic denervation are rescued by restoring Schwann cell c-Jun," *Elife,* vol. 10, p. e62232, 2021.

[254] J. Siironen, Y. Collan and M. Röyttä, "Axonal reinnervation does not influence Schwann cell proliferation after rat sciatic nerve transection," *Brain research,* vol. 654, p. 303–311, 1994.

[255] L. Vicuña, D. E. Strochlic, A. Latremoliere, K. K. Bali, M. Simonetti, D. Husainie, S. Prokosch, P. Riva, R. S. Griffin, C. Njoo and others, "The serine protease inhibitor SerpinA3N attenuates neuropathic pain by inhibiting T cell–derived leukocyte elastase," *Nature medicine,* vol. 21, p. 518–523, 2015.

[256] M. Zelenka, M. Schäfers and C. Sommer, "Intraneural injection of interleukin-1β and tumor necrosis factor-alpha into rat sciatic nerve at physiological doses induces signs of neuropathic pain," *Pain,* vol. 116, p. 257–263, 2005.

[257] P. Dömer, B. Kewitz, C. P. G. Heinen, U. Janssen-Bienhold and T. Kretschmer, "Analysis of regeneration-and myelination-associated proteins in human neuroma in continuity and discontinuity," *Acta Neurochirurgica,* vol. 160, p. 1269–1281, 2018.

[258] P. D. Kim, A. Hayes, F. Amin, Y. Akelina, A. P. Hays and M. P. Rosenwasser, "Collagen nerve protector in rat sciatic nerve repair: A morphometric and histological analysis," *Microsurgery,* vol. 30, p. 392–396, 2010.

[259] H. Millesi, G. Meissl and A. Berger, "The interfascicular nerve-grafting of the median and ulnar nerves," *JBJS,* vol. 54, p. 727–750, 1972.

[260] H. Millesi, Bridging defects: autologous nerve grafts, Springer, 2007.

[261] L. Djouhri and S. N. Lawson, "Aβ-fiber nociceptive primary afferent neurons: a review of incidence and properties in relation to other afferent A-fiber neurons in mammals," *Brain research reviews,* vol. 46, p. 131–145, 2004.

[262] A. R. Vora, A. R. Loescher, F. M. Boissonade and P. P. Robinson, "Ultrastructural characteristics of axons in traumatic neuromas of the human lingual nerve.," *Journal of orofacial pain,* vol. 19, 2005.

[263] T. Weng, P. Wu, W. Zhang, Y. Zheng, Q. Li, R. Jin, H. Chen, C. You, S. Guo, C. Han and others, "Regeneration of skin appendages and nerves: current status and further challenges," *Journal of translational medicine,* vol. 18, p. 1–17, 2020.

[264] J. E. Charlton, Core curriculum for professional education in pain, IASP press Seattle, 2005.

[265] T. Lin, A. Gargya, H. Singh, E. Sivanesan and A. Gulati, "Mechanism of peripheral nerve stimulation in chronic pain," *Pain Medicine,* vol. 21, p. S6–S12, 2020.

[266] M. L. Waskom, "seaborn: statistical data visualization," *Journal of Open Source Software,* vol. 6, p. 3021, 2021.

[267] F. Charlier, M. Weber, D. Izak, E. Harkin, M. Magnus, J. Lalli, L. Fresnais, M. Chan, N. Markov, O. Amsalem, S. Proost, A. Krasoulis, getzze and S. Repplinger, *Statannotations,* Zenodo, 2022.

8 SUPPLEMENTARY MATERIALS

8.1 RESULT TABLES

8.1.1 Psychophysical changes after PNI

8.1.1.1 Sensation Threshold

Experiment 1, Sensation threshold: Comparisons between participants

Population	Segment 1	Segment 2	median[IQR] 1	median[IQR] 2	p-value
AB	Lower arm	Upper arm	2.3 [1.0]	2.7 [1.1]	0.1641
	Lower arm	Shoulder	2.3 [1.0]	3.1 [1.8]	0.0039
	Upper arm	Shoulder	2.7 [1.1]	3.1 [1.8]	0.1289
BPI	Lower arm	Upper arm	83.8 [69.4]	29.4 [32.1]	0.0313
	Lower arm	Shoulder	83.8 [69.4]	11.8 [5.1]	0.0625
	Upper arm	Shoulder	29.4 [32.1]	11.8 [5.1]	0.0625
TR	Lower arm	Upper arm	3.7 [3.3]	4.5 [0.6]	0.3125
	Lower arm	Shoulder	3.7 [3.3]	3.3 [2.4]	1.0000
	Upper arm	Shoulder	4.5 [0.6]	3.3 [2.4]	0.6250

Table 3 - Sensation threshold: Between participants (LA vs. UA vs. SH)

Experiment 1, Sensation threshold variance: Comparisons between participants

Population	Segment 1	Segment 2	Variance 1	Variance 2	p-value
AB	Lower arm	Upper arm	0.84	1.30	0.8974
	Lower arm	Shoulder	0.84	2.07	0.3152
	Upper arm	Shoulder	1.30	2.07	0.4354
BPI	Lower arm	Upper arm	1436.98	733.08	0.4032
	Lower arm	Shoulder	1436.98	45.24	0.0318
	Upper arm	Shoulder	733.08	45.24	0.0743
TR	Lower arm	Upper arm	3.17	14.66	0.6747
	Lower arm	Shoulder	3.17	22.20	0.5466
	Upper arm	Shoulder	14.66	22.20	0.8246

Table 4 - Sensation variance: Between participants (LA vs. UA vs. SH)

Experiment 1, Sensation threshold: Comparisons between participants

Population	Segment 1	Segment 2	median[IQR] 1	median[IQR] 2	p-value
AB	Dorsal	Ventral	2.9 [1.4]	2.3 [1.4]	0.0078
BPI	Dorsal	Ventral	41.4 [28.6]	47.7 [36.0]	0.1563
TR	Dorsal	Ventral	4.2 [1.4]	2.8 [2.7]	1.0000

Table 5 - Sensation threshold: Between participants (ventral vs. dorsal)

Experiment 1, Sensation threshold variance: Comparisons between participants

Population	Segment 1	Segment 2	Variance 1	Variance 2	p-value
AB	Dorsal	Ventral	1.54	0.87	0.7711
BPI	Dorsal	Ventral	359.16	490.64	0.7324
TR	Dorsal	Ventral	6.37	15.84	0.6908

Table 6 – Sensation threshold variance: Between participants (ventral vs. dorsal)

Experiment 1, Sensation threshold: Comparisons between populations

Population	Segment 1	Segment 2	median[IQR] 1	median[IQR] 2	p-value
Lower arm	AB	BPI	2.3 [1.0]	83.8 [69.4]	0.0015
	AB	TR	2.3 [1.0]	3.7 [3.3]	0.3173
	BPI	TR	83.8 [69.4]	3.7 [3.3]	0.0062
Upper arm	AB	BPI	2.7 [1.1]	29.4 [32.1]	0.0015
	AB	TR	2.7 [1.1]	4.5 [0.6]	0.0719
	BPI	TR	29.4 [32.1]	4.5 [0.6]	0.0176
Shoulder	AB	BPI	3.1 [1.8]	11.8 [5.1]	0.0032
	AB	TR	3.1 [1.8]	3.3 [2.4]	0.6407
	BPI	TR	11.8 [5.1]	3.3 [2.4]	0.0679

Table 7 - Sensation threshold: Between populations (LA vs. UA vs. SH)

Experiment 1, Sensation threshold variance: Comparisons between populations

Population	Segment 1	Segment 2	Variance 1	Variance 2	p-value
AB	AB	BPI	0.84	1436.98	0.0029
	AB	TR	0.84	3.17	0.0667
	BPI	TR	1436.98	3.17	0.0301
BPI	AB	BPI	1.30	733.08	0.0065
	AB	TR	1.30	14.66	0.2447
	BPI	TR	733.08	14.66	0.0612
TR	AB	BPI	2.07	45.24	0.0380
	AB	TR	2.07	22.20	0.2828
	BPI	TR	45.24	22.20	0.5007

Table 8 – Sensation threshold variance: Between populations (LA vs. UA vs. SH)

Experiment 1, Sensation threshold: Comparisons between populations

Population	Segment 1	Segment 2	median[IQR] 1	median[IQR] 2	p-value
Dorsal	AB	BPI	2.9 [1.4]	41.4 [28.6]	0.0015
	AB	TR	2.9 [1.4]	4.2 [1.4]	0.2571
	BPI	TR	41.4 [28.6]	4.2 [1.4]	0.0062
Ventral	AB	BPI	2.3 [1.4]	47.7 [36.0]	0.0015
	AB	TR	2.3 [1.4]	2.8 [2.7]	0.2053
	BPI	TR	47.7 [36.0]	2.8 [2.7]	0.0106

Table 9 - Sensation threshold: Between populations (dorsal vs. ventral)

Experiment 1, Sensation threshold variance: Comparisons between populations

Population	Segment 1	Segment 2	Variance 1	Variance 2	p-value
Dorsal	AB	BPI	1.54	359.16	0.0033
	AB	TR	1.54	6.37	0.3086
	BPI	TR	359.16	6.37	0.0377
Ventral	AB	BPI	0.87	490.64	0.0024
	AB	TR	0.87	15.84	0.2027
	BPI	TR	490.64	15.84	0.0423

Table 10 - Sensation variance: Between populations (dorsal vs. ventral)

8.1.1.2 Weber fraction

Experiment 2, Weber Fraction: Comparisons between participants

Population	Segment 1	Segment 2	median[IQR] 1	median[IQR] 2	p-value
AB	Lower arm	Upper arm	19.5 [4.4]	17.5 [3.3]	0.4961
	Lower arm	Shoulder	19.5 [4.4]	18.1 [3.8]	0.6523
	Upper arm	Shoulder	17.5 [3.3]	18.1 [3.8]	0.8203
BPI	Lower arm	Upper arm	100.0 [0.0]	39.6 [28.7]	0.0313
	Lower arm	Shoulder	100.0 [0.0]	19.5 [3.3]	0.0313
	Upper arm	Shoulder	39.6 [28.7]	19.5 [3.3]	0.0313
TR	Lower arm	Upper arm	17.7 [1.9]	18.8 [0.9]	1.0000
	Lower arm	Shoulder	17.7 [1.9]	17.6 [1.3]	0.4375
	Upper arm	Shoulder	18.8 [0.9]	17.6 [1.3]	0.3125

Table 11 - Weber fraction: Between participants (LA vs. UA vs. SH)

Experiment 2, Weber Fraction variance: Comparisons between participants

Population	Segment 1	Segment 2	median[IQR] 1	median[IQR] 2	p-value
AB	Lower arm	Upper arm	26.40	7.71	0.6053
	Lower arm	Shoulder	26.40	34.05	0.8042
	Upper arm	Shoulder	7.71	34.05	0.4440
BPI	Lower arm	Upper arm	191.81	257.52	0.2617
	Lower arm	Shoulder	191.81	68.83	0.8580
	Upper arm	Shoulder	257.52	68.83	0.0563
TR	Lower arm	Upper arm	90.06	17.05	0.5037
	Lower arm	Shoulder	90.06	1.97	0.2850
	Upper arm	Shoulder	17.05	1.97	0.3264

Table 12 - Weber fraction variance: Between participants (LA vs. UA vs. SH)

Experiment 2, Weber Fraction: Comparisons between participants

Population	Segment 1	Segment 2	median[IQR] 1	median[IQR] 2	p-value
AB	Dorsal	Ventral	18.3 [1.3]	19.0 [3.4]	0.0742
BPI	Dorsal	Ventral	53.3 [15.0]	48.3 [11.1]	0.4375
TR	Dorsal	Ventral	17.6 [2.7]	18.1 [0.5]	0.3125

Table 13 - Weber fraction: Between participants (dorsal vs. ventral)

Experiment 2, Weber Fraction variance: Comparisons between participants

Population	Segment 1	Segment 2	Variance 1	Variance 2	p-value
AB	Dorsal	Ventral	5.06	13.23	0.3532
BPI	Dorsal	Ventral	170.94	64.72	0.2526
TR	Dorsal	Ventral	17.16	33.05	0.8916

Table 14 - Weber fraction variance: Between participants (dorsal v. ventral)

Experiment 2, Weber Fraction: Comparisons between populations

Population	Segment 1	Segment 2	median[IQR] 1	median[IQR] 2	p-value

Lower arm	AB	BPI	19.5 [4.4]	100.0 [0.0]	0.0015
	AB	TR	19.5 [4.4]	17.7 [1.9]	0.7389
	BPI	TR	100.0 [0.0]	17.7 [1.9]	0.0062
Upper arm	AB	BPI	17.5 [3.3]	39.6 [28.7]	0.0339
	AB	TR	17.5 [3.3]	18.8 [0.9]	0.8415
	BPI	TR	39.6 [28.7]	18.8 [0.9]	0.0679
Shoulder	AB	BPI	18.1 [3.8]	19.5 [3.3]	0.8137
	AB	TR	18.1 [3.8]	17.6 [1.3]	0.3861
	BPI	TR	19.5 [3.3]	17.6 [1.3]	0.2733

Table 15 - Weber fraction: Between populations (LA vs. UA vs. SH)

Experiment 2, Weber Fraction variance: Comparisons between populations

Population	Segment 1	Segment 2	Variance 1	Variance 2	p-value
AB	AB	BPI	26.40	191.81	0.5812
	AB	TR	26.40	90.06	0.4735
	BPI	TR	191.81	90.06	0.9681
BPI	AB	BPI	7.71	257.52	0.0005
	AB	TR	7.71	17.05	0.7687
	BPI	TR	257.52	17.05	0.0125
TR	AB	BPI	34.05	68.83	0.7275
	AB	TR	34.05	1.97	0.2720
	BPI	TR	68.83	1.97	0.2944

Table 16 - Weber fraction variance: Between populations (LA vs. UA vs. SH)

Experiment 2, Weber Fraction: Comparisons between populations

Population	Segment 1	Segment 2	median[IQR] 1	median[IQR] 2	p-value
Dorsal	AB	BPI	18.3 [1.3]	53.3 [15.0]	0.0015
	AB	TR	18.3 [1.3]	17.6 [2.7]	0.6407
	BPI	TR	53.3 [15.0]	17.6 [2.7]	0.0062
Ventral	AB	BPI	19.0 [3.4]	48.3 [11.1]	0.0015
	AB	TR	19.0 [3.4]	18.1 [0.5]	0.3173
	BPI	TR	48.3 [11.1]	18.1 [0.5]	0.0062

Table 17 - Weber fraction: Between populations (dorsal vs. ventral)

Experiment 2, Weber Fraction variance: Comparisons between populations

Population	Segment 1	Segment 2	Variance 1	Variance 2	p-value
Dorsal	AB	BPI	5.06	170.94	0.0024
	AB	TR	5.06	17.16	0.2932
	BPI	TR	170.94	17.16	0.0503
Ventral	AB	BPI	13.23	64.72	0.0887
	AB	TR	13.23	33.05	0.7380
	BPI	TR	64.72	33.05	0.3606

Table 18 - Weber fraction variance: Between participants (dorsal vs. ventral)

8.1.1.3 Number of distinct intervals

Experiment 2, Number of distinct intervals: Comparisons between participants

Population	Segment 1	Segment 2	median[IQR] 1	median[IQR] 2	p-value
AB	Lower arm	Upper arm	10.0 [5.0]	11.0 [0.0]	0.2500
	Lower arm	Shoulder	10.0 [5.0]	12.0 [2.0]	0.2567
	Upper arm	Shoulder	11.0 [0.0]	12.0 [2.0]	0.6148
BPI	Lower arm	Upper arm	2.0 [0.0]	4.5 [4.5]	0.0679
	Lower arm	Shoulder	2.0 [0.0]	8.0 [2.2]	0.0313
	Upper arm	Shoulder	4.5 [4.5]	8.0 [2.2]	0.0313
TR	Lower arm	Upper arm	10.0 [2.0]	10.0 [3.0]	0.7855
	Lower arm	Shoulder	10.0 [2.0]	12.0 [1.0]	0.4652
	Upper arm	Shoulder	10.0 [3.0]	12.0 [1.0]	1.0000

Table 19 - Number of distinct intervals: Comparisons between participants (LA vs. UA vs. SH)

Experiment 2, Number of distinct intervals variance: Comparisons between participants

Population	Segment 1	Segment 2	Variance 1	Variance 2	p-value
AB	Lower arm	Upper arm	9.28	1.95	0.0562
	Lower arm	Shoulder	9.28	5.36	0.3918
	Upper arm	Shoulder	1.95	5.36	0.2933
BPI	Lower arm	Upper arm	0.00	10.47	0.0039
	Lower arm	Shoulder	0.00	9.81	0.0721
	Upper arm	Shoulder	10.47	9.81	0.6241
TR	Lower arm	Upper arm	13.76	7.84	0.8103
	Lower arm	Shoulder	13.76	2.96	0.3829
	Upper arm	Shoulder	7.84	2.96	0.4194

Table 20 - Number of distinct intervals variance: Comparisons between participants (LA vs. UA vs. SH)

Experiment 2, Number of distinct intervals: Comparisons between participants

Population	Segment 1	Segment 2	median[IQR] 1	median[IQR] 2	p-value
AB	Dorsal	Ventral	10.0 [5.0]	11.0 [3.0]	0.7344
BPI	Dorsal	Ventral	2.0 [0.0]	2.0 [0.0]	0.3173
TR	Dorsal	Ventral	10.0 [2.0]	12.0 [0.0]	0.8125

Table 21 - Number of distinct intervals: Comparisons between participants (dorsal vs. ventral)

Experiment 2, Number of distinct intervals variance: Comparisons between participants

Population	Segment 1	Segment 2	Variance 1	Variance 2	p-value
AB	Dorsal	Ventral	9.28	5.51	0.5269
BPI	Dorsal	Ventral	0.00	0.14	0.3409
TR	Dorsal	Ventral	13.76	8.56	0.6134

Table 22 - Number of distinct intervals variance: Comparisons between participants (dorsal vs. ventral)

Experiment 2, Number of distinct intervals: Comparisons between populations

Population	Segment 1	Segment 2	median[IQR] 1	median[IQR] 2	p-value
Lower arm	AB	BPI	10.0 [5.0]	2.0 [0.0]	0.0015
	AB	TR	10.0 [5.0]	10.0 [2.0]	0.8939
	BPI	TR	2.0 [0.0]	10.0 [2.0]	0.0062
Upper arm	AB	BPI	11.0 [0.0]	4.5 [4.5]	0.0080
	AB	TR	11.0 [0.0]	10.0 [3.0]	0.6407

	BPI	TR	4.5 [4.5]	10.0 [3.0]	0.0552
Shoulder	AB	BPI	12.0 [2.0]	8.0 [2.2]	0.1116
	AB	TR	12.0 [2.0]	12.0 [1.0]	0.7897
	BPI	TR	8.0 [2.2]	12.0 [1.0]	0.1441

Table 23 - Number of distinct intervals: Comparisons between populations (LA vs. UA vs. SH)

Experiment 2, Number of distinct intervals variance: Comparisons between populations

Population	Segment 1	Segment 2	Variance 1	Variance 2	p-value
AB	AB	BPI	9.28	0.00	0.0094
	AB	TR	9.28	13.76	0.9069
	BPI	TR	0.00	13.76	0.0580
BPI	AB	BPI	1.95	10.47	0.0264
	AB	TR	1.95	7.84	0.1477
	BPI	TR	10.47	7.84	0.6042
TR	AB	BPI	5.36	9.81	0.6682
	AB	TR	5.36	2.96	0.6414
	BPI	TR	9.81	2.96	0.4963

Table 24 - Number of distinct intervals variance: Comparisons between populations (LA vs. UA vs. SH)

Experiment 2, Number of distinct intervals: Comparisons between populations

Population	Segment 1	Segment 2	median[IQR] 1	median[IQR] 2	p-value
Dorsal	AB	BPI	10.0 [5.0]	2.0 [0.0]	0.0015
	AB	TR	10.0 [5.0]	10.0 [2.0]	0.8939
	BPI	TR	2.0 [0.0]	10.0 [2.0]	0.0062
Ventral	AB	BPI	11.0 [3.0]	2.0 [0.0]	0.0015
	AB	TR	11.0 [3.0]	12.0 [0.0]	0.5050
	BPI	TR	2.0 [0.0]	12.0 [0.0]	0.0062

Table 25 - Number of distinct intervals: Comparisons between populations (dorsal vs. ventral)

Experiment 2, Number of distinct intervals variance: Comparisons between populations

Population	Segment 1	Segment 2	Variance 1	Variance 2	p-value
Dorsal	AB	BPI	9.28	0.00	0.0094
	AB	TR	9.28	13.76	0.9069
	BPI	TR	0.00	13.76	0.0580
Ventral	AB	BPI	5.51	0.14	0.0310
	AB	TR	5.51	8.56	0.8209
	BPI	TR	0.14	8.56	0.2792

Table 26 - Number of distinct intervals variance: Comparisons between populations (dorsal vs. ventral)

8.1.1.4 Tracking task

Experiment 3, Correlation: Comparisons between participants

Population	Segment 1	Segment 2	median[IQR] 1	median[IQR] 2	p-value
AB	Visual	Lower arm	92.0 [1.9]	70.2 [12.3]	0.0039
	Visual	Upper arm	92.0 [1.9]	70.2 [10.1]	0.0039

	Visual	Shoulder	92.0 [1.9]	64.4 [14.7]	0.0039
	Lower arm	Upper arm	70.2 [12.3]	70.2 [10.1]	0.3594
	Lower arm	Shoulder	70.2 [12.3]	64.4 [14.7]	0.6523
	Upper arm	Shoulder	70.2 [10.1]	64.4 [14.7]	0.0391
BPI	Visual	Lower arm	92.2 [3.1]	0.0 [0.0]	0.0625
	Visual	Upper arm	92.2 [3.1]	44.9 [17.2]	0.0625
	Visual	Shoulder	92.2 [3.1]	68.1 [25.6]	0.0625
	Lower arm	Upper arm	0.0 [0.0]	44.9 [17.2]	0.0625
	Lower arm	Shoulder	0.0 [0.0]	68.1 [25.6]	0.0625
	Upper arm	Shoulder	44.9 [17.2]	68.1 [25.6]	0.1250
TR	Visual	Lower arm	93.7 [7.0]	74.8 [29.0]	0.0625
	Visual	Upper arm	93.7 [7.0]	81.2 [27.1]	0.0625
	Visual	Shoulder	93.7 [7.0]	75.5 [38.4]	0.1250
	Lower arm	Upper arm	74.8 [29.0]	81.2 [27.1]	0.4375
	Lower arm	Shoulder	74.8 [29.0]	75.5 [38.4]	0.6250
	Upper arm	Shoulder	81.2 [27.1]	75.5 [38.4]	0.1250

Table 27 - Correlation: Comparisons between participants

Experiment 3, Correlation variance: Comparisons between participants

Population	Segment 1	Segment 2	Variance 1	Variance 2	p-value
AB	Visual	Lower arm	3.72	123.41	0.0082
	Visual	Upper arm	3.72	53.88	0.0353
	Visual	Shoulder	3.72	102.33	0.0015
	Lower arm	Upper arm	123.41	53.88	0.3099
	Lower arm	Shoulder	123.41	102.33	0.9551
	Upper arm	Shoulder	53.88	102.33	0.2620
BPI	Visual	Lower arm	7.30	0.00	0.0316
	Visual	Upper arm	7.30	122.72	0.0693
	Visual	Shoulder	7.30	227.28	0.0834
	Lower arm	Upper arm	0.00	122.72	0.0233
	Lower arm	Shoulder	0.00	227.28	0.0429
	Upper arm	Shoulder	122.72	227.28	0.6051
TR	Visual	Lower arm	12.65	271.28	0.0380
	Visual	Upper arm	12.65	204.51	0.0885
	Visual	Shoulder	12.65	348.83	0.0377
	Lower arm	Upper arm	271.28	204.51	0.7722
	Lower arm	Shoulder	271.28	348.83	0.7611
	Upper arm	Shoulder	204.51	348.83	0.5787

Table 28 - Correlation variance: Comparisons between participants

Experiment 3, Correlation: Comparisons between populations

Population	Segment 1	Segment 2	median[IQR] 1	median[IQR] 2	p-value
Visual	AB	BPI	92.0 [1.9]	92.2 [3.1]	0.9468
	AB	TR	92.0 [1.9]	93.7 [7.0]	0.7389
	BPI	TR	92.2 [3.1]	93.7 [7.0]	1.0000
Lower arm	AB	BPI	70.2 [12.3]	0.0 [0.0]	0.0027
	AB	TR	70.2 [12.3]	74.8 [29.0]	0.5485
	BPI	TR	0.0 [0.0]	74.8 [29.0]	0.0625
Upper arm	AB	BPI	70.2 [10.1]	44.9 [17.2]	0.0041

	AB	TR	70.2 [10.1]	81.2 [27.1]	0.5485
	BPI	TR	44.9 [17.2]	81.2 [27.1]	0.0625
Shoulder	AB	BPI	64.4 [14.7]	68.1 [25.6]	0.6407
	AB	TR	64.4 [14.7]	75.5 [38.4]	0.6407
	BPI	TR	68.1 [25.6]	75.5 [38.4]	0.0000

Table 29 - Correlation: Comparisons between populations

Experiment 3, Correlation variance: Comparisons between populations

Population	Segment 1	Segment 2	Variance 1	Variance 2	p-value
Visual	AB	BPI	3.72	7.30	0.4872
	AB	TR	3.72	12.65	0.1485
	BPI	TR	7.30	12.65	0.5175
Lower arm	AB	BPI	123.41	0.00	0.0189
	AB	TR	123.41	271.28	0.2577
	BPI	TR	0.00	271.28	0.0113
Upper arm	AB	BPI	53.88	122.72	0.3117
	AB	TR	53.88	204.51	0.1358
	BPI	TR	122.72	204.51	0.6151
Shoulder	AB	BPI	102.33	227.28	0.3933
	AB	TR	102.33	348.83	0.1136
	BPI	TR	227.28	348.83	0.6351

Table 30 - Correlation variance: Comparisons between populations

Experiment 3, Error: Comparisons between participants

Population	Segment 1	Segment 2	median[IQR] 1	median[IQR] 2	p-value
AB	Visual	Lower arm	0.2 [0.0]	0.3 [0.1]	0.0039
	Visual	Upper arm	0.2 [0.0]	0.3 [0.1]	0.0039
	Visual	Shoulder	0.2 [0.0]	0.3 [0.0]	0.0039
	Lower arm	Upper arm	0.3 [0.1]	0.3 [0.1]	0.3594
	Lower arm	Shoulder	0.3 [0.1]	0.3 [0.0]	0.0547
	Upper arm	Shoulder	0.3 [0.1]	0.3 [0.0]	0.0039
BPI	Visual	Lower arm	0.2 [0.0]	0.0 [0.0]	0.0625
	Visual	Upper arm	0.2 [0.0]	0.4 [0.0]	0.0625
	Visual	Shoulder	0.2 [0.0]	0.4 [0.1]	0.0625
	Lower arm	Upper arm	0.0 [0.0]	0.4 [0.0]	0.0625
	Lower arm	Shoulder	0.0 [0.0]	0.4 [0.1]	0.0625
	Upper arm	Shoulder	0.4 [0.0]	0.4 [0.1]	0.3125
TR	Visual	Lower arm	0.2 [0.1]	0.3 [0.2]	0.0625
	Visual	Upper arm	0.2 [0.1]	0.3 [0.1]	0.0625
	Visual	Shoulder	0.2 [0.1]	0.3 [0.2]	0.1250
	Lower arm	Upper arm	0.3 [0.2]	0.3 [0.1]	0.1875
	Lower arm	Shoulder	0.3 [0.2]	0.3 [0.2]	0.4375
	Upper arm	Shoulder	0.3 [0.1]	0.3 [0.2]	0.3125

Table 31 - Error: Comparisons between participants

Experiment 3, Error variance: Comparisons between participants

Population	Segment 1	Segment 2	Variance 1	Variance 2	p-value

AB	Visual	Lower arm	0.0004	0.0033	0.0294
	Visual	Upper arm	0.0004	0.0024	0.0146
	Visual	Shoulder	0.0004	0.0020	0.0612
	Lower arm	Upper arm	0.0033	0.0024	0.8044
	Lower arm	Shoulder	0.0033	0.0020	0.5216
	Upper arm	Shoulder	0.0024	0.0020	0.6361
BPI	Visual	Lower arm	0.0007	0.0000	0.1321
	Visual	Upper arm	0.0007	0.0008	0.7132
	Visual	Shoulder	0.0007	0.0040	0.1264
	Lower arm	Upper arm	0.0000	0.0008	0.0838
	Lower arm	Shoulder	0.0000	0.0040	0.0211
	Upper arm	Shoulder	0.0008	0.0040	0.2047
TR	Visual	Lower arm	0.0010	0.0078	0.0896
	Visual	Upper arm	0.0010	0.0049	0.2359
	Visual	Shoulder	0.0010	0.0140	0.0259
	Lower arm	Upper arm	0.0078	0.0049	0.6302
	Lower arm	Shoulder	0.0078	0.0140	0.4746
	Upper arm	Shoulder	0.0049	0.0140	0.2540

Table 32 - Error variance: Comparisons between participants

Experiment 3, Error: Comparisons between populations

Population	Segment 1	Segment 2	median[IQR] 1	median[IQR] 2	p-value
Visual	AB	BPI	0.2 [0.0]	0.2 [0.0]	0.3861
	AB	TR	0.2 [0.0]	0.2 [0.1]	0.6407
	BPI	TR	0.2 [0.0]	0.2 [0.1]	0.6250
Lower arm	AB	BPI	0.3 [0.1]	0.0 [0.0]	0.0027
	AB	TR	0.3 [0.1]	0.3 [0.2]	0.9468
	BPI	TR	0.0 [0.0]	0.3 [0.2]	0.0625
Upper arm	AB	BPI	0.3 [0.1]	0.4 [0.0]	0.0027
	AB	TR	0.3 [0.1]	0.3 [0.1]	0.7389
	BPI	TR	0.4 [0.0]	0.3 [0.1]	0.0625
Shoulder	AB	BPI	0.3 [0.0]	0.4 [0.1]	0.3861
	AB	TR	0.3 [0.0]	0.3 [0.2]	0.9468
	BPI	TR	0.4 [0.1]	0.3 [0.2]	0.3125

Table 33 - Error: Comparisons between populations

Experiment 3, Error variance: Comparisons between populations

Population	Segment 1	Segment 2	Variance 1	Variance 2	p-value
Visual	AB	BPI	0.0004	0.0007	0.8826
	AB	TR	0.0004	0.0010	0.1738
	BPI	TR	0.0007	0.0010	0.4649
Lower arm	AB	BPI	0.0033	0.0000	0.0164
	AB	TR	0.0033	0.0078	0.2249
	BPI	TR	0.0000	0.0078	0.0135
Upper arm	AB	BPI	0.0024	0.0008	0.2170
	AB	TR	0.0024	0.0049	0.4245
	BPI	TR	0.0008	0.0049	0.2057

Shoulder	AB	BPI	0.0020	0.0040	0.3688
	AB	TR	0.0020	0.0140	0.0126
	BPI	TR	0.0040	0.0140	0.1596

Table 34 - Error variance: Comparisons between populations

Experiment 3, Delay: Comparisons between participants

Population	Segment 1	Segment 2	median[IQR] 1	median[IQR] 2	p-value
AB	Visual	Lower arm	44.4 [7.4]	47.6 [9.1]	0.3594
	Visual	Upper arm	44.4 [7.4]	46.7 [6.0]	0.3008
	Visual	Shoulder	44.4 [7.4]	48.4 [13.2]	0.2031
	Lower arm	Upper arm	47.6 [9.1]	46.7 [6.0]	0.7344
	Lower arm	Shoulder	47.6 [9.1]	48.4 [13.2]	0.1641
	Upper arm	Shoulder	46.7 [6.0]	48.4 [13.2]	0.2500
BPI	Visual	Lower arm	42.5 [4.6]	0.0 [0.0]	0.0625
	Visual	Upper arm	42.5 [4.6]	71.6 [61.2]	0.0625
	Visual	Shoulder	42.5 [4.6]	58.1 [25.4]	0.1250
	Lower arm	Upper arm	0.0 [0.0]	71.6 [61.2]	0.0625
	Lower arm	Shoulder	0.0 [0.0]	58.1 [25.4]	0.0625
	Upper arm	Shoulder	71.6 [61.2]	58.1 [25.4]	0.8125
TR	Visual	Lower arm	49.0 [6.6]	58.6 [25.5]	0.4375
	Visual	Upper arm	49.0 [6.6]	49.4 [17.2]	1.0000
	Visual	Shoulder	49.0 [6.6]	56.7 [19.5]	0.4375
	Lower arm	Upper arm	58.6 [25.5]	49.4 [17.2]	0.0625
	Lower arm	Shoulder	58.6 [25.5]	56.7 [19.5]	0.6250
	Upper arm	Shoulder	49.4 [17.2]	56.7 [19.5]	0.1875

Table 35 - Delay: Comparisons between participants

Experiment 3, Delay variance: Comparisons between participants

Population	Segment 1	Segment 2	Variance 1	Variance 2	p-value
AB	Visual	Lower arm	21.52	27.63	0.6536
	Visual	Upper arm	21.52	24.46	0.9808
	Visual	Shoulder	21.52	79.69	0.1177
	Lower arm	Upper arm	27.63	24.46	0.6778
	Lower arm	Shoulder	27.63	79.69	0.1943
	Upper arm	Shoulder	24.46	79.69	0.1344
BPI	Visual	Lower arm	8.89	0.00	0.0100
	Visual	Upper arm	8.89	2125.47	0.0740
	Visual	Shoulder	8.89	8057.58	0.2594
	Lower arm	Upper arm	0.00	2125.47	0.0580
	Lower arm	Shoulder	0.00	8057.58	0.2377
	Upper arm	Shoulder	2125.47	8057.58	0.7270
TR	Visual	Lower arm	12.78	6157.07	0.2563
	Visual	Upper arm	12.78	82.16	0.1037
	Visual	Shoulder	12.78	5493.20	0.2645
	Lower arm	Upper arm	6157.07	82.16	0.3102
	Lower arm	Shoulder	6157.07	5493.20	0.9453
	Upper arm	Shoulder	82.16	5493.20	0.3238

Table 36 - Delay variance: Comparisons between participants

Experiment 3, Delay: Comparisons between populations

Population	Segment 1	Segment 2	median[IQR] 1	median[IQR] 2	p-value
Visual	AB	BPI	44.4 [7.4]	42.5 [4.6]	0.2571
	AB	TR	44.4 [7.4]	49.0 [6.6]	0.5485
	BPI	TR	42.5 [4.6]	49.0 [6.6]	0.3125
Lower arm	AB	BPI	47.6 [9.1]	0.0 [0.0]	0.0027
	AB	TR	47.6 [9.1]	58.6 [25.5]	0.3861
	BPI	TR	0.0 [0.0]	58.6 [25.5]	0.0625
Upper arm	AB	BPI	46.7 [6.0]	71.6 [61.2]	0.0388
	AB	TR	46.7 [6.0]	49.4 [17.2]	0.9468
	BPI	TR	71.6 [61.2]	49.4 [17.2]	0.1250
Shoulder	AB	BPI	48.4 [13.2]	58.1 [25.4]	0.3861
	AB	TR	48.4 [13.2]	56.7 [19.5]	0.9468
	BPI	TR	58.1 [25.4]	56.7 [19.5]	0.8125

Table 37 - Delay: Comparisons between populations

Experiment 3, Delay variance: Comparisons between populations

Population	Segment 1	Segment 2	Variance 1	Variance 2	p-value
Visual	AB	BPI	21.52	8.89	0.3597
	AB	TR	21.52	12.78	0.5998
	BPI	TR	8.89	12.78	0.7262
Lower arm	AB	BPI	27.63	0.00	0.0066
	AB	TR	27.63	6157.07	0.1275
	BPI	TR	0.00	6157.07	0.2266
Upper arm	AB	BPI	24.46	2125.47	0.0187
	AB	TR	24.46	82.16	0.1195
	BPI	TR	2125.47	82.16	0.1249
Shoulder	AB	BPI	79.69	8057.58	0.1574
	AB	TR	79.69	5493.20	0.1683
	BPI	TR	8057.58	5493.20	0.8592

Table 38 - Delay variance: Comparisons between populations

8.1.2 Neuropathology of neuromas

8.1.2.1 Inflammation-related cells

Comparison	*Variable 1*	*Variable 2*	*Results 1*	*Results 2*	*p-value*
CD3 Density (mm⁻²)	controls	patients	0.3 [0.5]	0.2 [0.2]	0.488
CD3 Weighted density idx	controls	patients	-0.3 [0.5]	0.1 [0.2]	0.034
CD3 Density (mm⁻²)	no pain	pain	0.2 [0.3]	0.2 [0.2]	0.875
CD3 Weighted density idx	no pain	pain	-0.0 [0.3]	0.2 [0.2]	0.043
KiM1P Density (mm⁻²)	controls	patients	0.0 [0.2]	0.2 [0.3]	0.630
KiM1P Weighted density idx	controls	patients	-0.0 [0.2]	0.1 [0.2]	0.093
KiM1P Density (mm⁻²)	no pain	pain	0.2 [0.2]	0.2 [0.3]	0.678
KiM1P Weighted density idx	no pain	pain	-0.0 [0.2]	0.2 [0.2]	0.266

S100 Area	controls	patients	0.5 [0.3]	0.4 [0.5]	0.318
S100 Weighted area idx	controls	patients	-0.5 [0.3]	0.2 [0.4]	0.006
S100 Area	no pain	pain	0.7 [0.3]	0.3 [0.3]	0.608
S100 Weighted area idx	no pain	pain	-0.1 [0.4]	0.3 [0.3]	0.145

Table 39 Inflammation-related cells in controls and neuromas

8.1.2.2 Morphologies

Comparison	*Variable 1*	*Variable 2*	*Results 1*	*Results 2*	*p-value*
Neuroma (%)	controls	patients	0.0 [0.0]	35.5 [32.8]	0.007
Fascicles (%)	controls	patients	33.5 [16.0]	6.2 [18.8]	0.106
Connective tissue (%)	controls	patients	30.8 [12.9]	31.5 [15.5]	0.515
Fat tissue (%)	controls	patients	25.7 [19.0]	6.9 [8.0]	0.030
Neuroma (mm²)	controls	patients	0.0 [0.0]	20.2 [74.9]	0.007
Fascicles (mm²)	controls	patients	4.6 [7.4]	9.0 [10.5]	0.799
Connective tissue (mm²)	controls	patients	3.9 [3.6]	28.1 [38.8]	0.066
Fat tissue (mm²)	controls	patients	2.5 [11.4]	5.3 [5.4]	0.562
Nerve size (mm²)	controls	patients	11.1 [24.7]	86.7 [99.7]	0.135
Neuroma (%)	no pain	pain	16.5 [11.3]	36.9 [24.9]	0.113
Fascicles (%)	no pain	pain	37.4 [17.3]	3.7 [4.1]	0.006
Connective tissue (%)	no pain	pain	26.1 [7.0]	39.1 [21.6]	0.618
Fat tissue (%)	no pain	pain	1.6 [10.4]	8.6 [3.8]	0.623
Intruding conn. tissue (%)	no pain	pain	1.9 [6.5]	15.5 [6.6]	0.172
Neuroma incl. conn. tissue (%)	no pain	pain	25.9 [14.4]	58.9 [34.2]	0.150
Neuroma (mm²)	no pain	pain	9.3 [12.8]	68.2 [88.0]	0.232
Fascicles (mm²)	no pain	pain	14.3 [11.1]	5.5 [11.5]	0.162
Connective tissue (mm²)	no pain	pain	14.0 [14.7]	68.1 [55.3]	0.219
Fat tissue (mm²)	no pain	pain	0.9 [1.8]	7.8 [2.2]	0.147
Intruding conn. tissue (mm²)	no pain	pain	0.6 [6.0]	10.3 [20.5]	0.283
Neuroma incl. conn. tissue (mm²)	no pain	pain	14.6 [20.9]	104.3 [96.9]	0.263
Nerve size (mm²)	no pain	pain	56.3 [35.1]	131.9 [103.8]	0.232
Normalized deviation	no pain	pain	-0.7 [0.6]	0.9 [0.1]	0.006

Table 40 - Morphological analysis of controls and neuromas

8.2 FIGURE DESIGN AND FURTHER SOFTWARE

All figures in this thesis, including graphical representations were created with BioRender.com or Microsoft PowerPoint. All plots showing experimental results were created using Seaborn [266] and statistical annotation were included using Statannotations [267]; both libraries are available for Python. For grammar and style, Grammarly.com suggestions were taken into account.